Metal Alkoxide Inks for High Resolution Electrohydrodynamic Inkjet Printing with Applications in Meta-Optics, Photonics, and Plasmonics

Holly J. C. Brunner

A dissertation

submitted in partial fulfillment of the

requirements for the degree of

Doctor of Philosophy

University of Washington

2023

Reading Committee:

J. Devin MacKenzie, Chair

Guozhong Cao

Arka Majumdar

Peter J. Pauzauskie

Program Authorized to Offer Degree:

Materials Science and Engineering

University of Washington

Abstract

Metal Alkoxide Inks for High Resolution Electrohydrodynamic Inkjet Printing with Applications in Meta-Optics, Photonics, and Plasmonics

Holly J. C. Brunner

Chair of the Supervisory Committee:
Washington Research Foundation Professor of Clean Energy
Associate Professor of Materials Science and Engineering and Mechanical Engineering
J. Devin MacKenzie
Department of Materials Science and Engineering

Additive manufacturing at the micron and sub-micron scale is a rapidly expanding field with electrohydrodynamic inkjet (EHD) printing proving to be a critical fabrication technique that will enable continued advancement. Increasing the range of materials compatible with EHD printing to create micron and sub-micron scale features is critical to increasing the variety of devices that can be fabricated with this method. Ceramic, semiconducting, and hybrid organic-inorganic materials are essential for meta-optics and micro-electromechanical systems devices and yet these materials are vastly underexplored for applications in EHD printing. A range of novel printing formulations with varying material properties, all containing a titanium alkoxide precursor that is compatible with EHD, are investigated in search of a material capable of achieving high resolution

EHD printing objectives. Methods for more efficiently developing novel printing formulations are presented along with optimized TiO_2 printing solutions that can consistently produce final printed features on the order of 500 nm; the highest resolution features ever reported for this family of materials and this method. These solutions are used to fabricate functional and representative meta-optical device components. The first additively manufactured, EHD printed and functional mid-infrared meta-optical lens, capable of focusing 5 μm light is presented along with optical device components for hybrid plasmonic bullseye antennae, designed to focus 1530 nm light.

TABLE OF CONTENTS

LIST OF FIGURES

LIST OF TABLES

ACKNOWLEDGEMENTS

First, I would like to acknowledge and thank my research advisor, Professor Devin MacKenzie, for the incredible range of research projects I have had the fortune to work on during my time as a graduate student. I met Devin in my first week at the University of Washington and I was immediately intrigued by the scope of his research. I knew that with him as my advisor, I would always be on the cutting edge of an exciting field of research. I am also immensely grateful to Devin for the open mind he brings to every research meeting and for the freedom and creativity I have been allowed to maintain as a graduate student. Under Devin's supervision, I truly learned how to be an independent scientist and was introduced to a field of research about which I am deeply passionate and plan to explore long into the future.

I also wish to thank the members of my supervisory committee: Professors Peter Pauzauskie, Guozhong Cao, and Arka Majumdar. I appreciate the time you have taken to read and review my research, listen to my presentations, and question my assumptions, all in service of strengthening my skills as a scientist. I have had the pleasure of working with each of you in a context outside of your roles on my supervisory committee, either as a student in one of your classes, as a research collaborator, or both. I deeply admire the care you all bring to your work as professors and advisors and am grateful for the knowledge and skills you imparted on me during my time at the University of Washington.

I owe a debt of gratitude to the many staff members of the research facilities where I work and the administrative staff of the Materials Science and Engineering department. To the staff members

of the Washington Clean Energy Testbeds and the Molecular Analysis Facility, thank you so much for the many hours you spent training me on delicate instruments, answering my questions, and brainstorming solutions. Without your assistance, the research in this dissertation would not have been possible. Also thank you to the funding agencies that sustained my graduate research, specifically the National Science Foundation and the Washington Research Foundation. I will be eternally grateful for the opportunities made possible by the research funding I received.

As for my fellow University of Washington students, I am so grateful for the many friends I have made over my years here. You provided much needed levity in moments of frustration and you provided insight in moments of confusion. You commiserated with me during the hours of work that appeared, in the moment, to lead nowhere and you celebrated me when I accomplished something substantial. I cannot thank you enough for being a collectively unflappable support system.

I am equally grateful for my community outside of the university. It is not an exaggeration to say that I would not be the person I am today without the friends and mentors I made in the Seattle rowing community. In times of true hardship, the sport of rowing and the people who bring the sport alive, have helped me make it through. There were many moments where I felt lost and uncertain of my ability to complete my doctoral degree and in all of these moments rowing has been there to provide me with harmony, rhythm, and balance.

Finally, words cannot express how fortunate I am to have a family as loving and supportive as mine. I have always been encouraged to pursue the things I care about, even when those pursuits take me far away from home. You bring me joy, wherever I am, and I carry you all in my heart, wherever I go. None of this would have been possible without you.

DEDICATION

to my loving family who have supported me throughout this journey

and to women and girls everywhere, pursuing their dreams in the face of adversity

Chapter 1. INTRODUCTION

Throughout the millennia of human civilization, there has existed a motivation to understand the surrounding world. This curiosity spanned wondering about the origin of the furthest stars to philosophizing about the smallest unit of matter. From the discovery of the atom and the development of the Bohr model to more modern advances such as single nanometer transistors for high-speed computing, the determination to understand and then push beyond the existing lowest limit of any field has led to some of the most significant advances in science, and thus humanity. The field and methods in which these advancements are made may differ, but the overall motivation is the same: identify the existing limit and move the field beyond the existing limits to a smaller scale.

In tandem to this pursuit of understanding the world at the smallest possible scale, there exists an equally strong practice in human history of respecting and preserving the natural world. Examples of this cross the spectrum from religious practices, both ancient and modern, to the contemporary global environmental movement working to reduce climate warming emissions through the adoption of renewable energy and development of clean technology. The practices have varied by region and point in time but there exists a common theme to care for the Earth's natural environment.

The field of materials science and engineering has long existed in an interdisciplinary space, with many key contributors to the field working to understand the natural environment in an effort to improve the built environment. In the broadest sense, guiding the research are to make advancements in the fields of printed electronics and nanoscale additive manufacturing in search of smaller scale printed features using methods that minimizes the human impact of research,

development, and manufacturing on the surrounding world. The expansion of nanoscale additive manufacturing and printed electronics requires the development of novel material formulations and processes and a deeper understanding of the existing tools and techniques. Continued scientific research is required to meet existing needs and expand the field.

1.1 MOTIVATION

The last two decades have seen significant research and development efforts towards additive manufacturing of functional materials using inkjet printing and direct write 3D printing techniques for applications in displays, energy harvesting, and flexible electronics. [1], [2], [3], [4], [5] The advanced processing enabled by the developments in additive manufacturing has received wide-spread attention due to the wide range of compatible materials and variety of devices that can be made with these methods. [6], [7] These fabrication advances include creating micrometer and nanometer scale features out of a wider selection of materials and substrates than is possible with traditional micro and nanofabrication methods. [8], [9] Furthermore, traditional fabrication methods frequently require harsh post-processing steps such as wet or dry etching and solvent or developer baths. These processes are not only incompatible with many types of substrates but can also degrade the deposited active materials, completely destroying the fabricated device. Direct printing processes allow for the modification of sensitive or delicate devices by only adding the desired features to the active surface which generally avoids harsh post-processing steps. [5], [6]

Another significant consideration for modern device fabrication is the scalability of the fabrication process. Small scale devices for use in imbedded and wearable sensors or energy harvesting and storage, can only achieve wide-ranging impact if they can be fabricated in a cost-effective manner. [5] Speed of fabrication, quantity, and cost of consumable materials, as well as energy expended during the production process are all key elements to be considered and

minimized when developing a scalable process. [10] Solution based additive manufacturing addresses the issue of scalability in several ways. First, the rapid prototyping enabled by many printing processes allows for new device designs to be made and tested quickly. This leads to efficiency in research and development and reduce waste by only fabricating the devices necessary to test a concept. [11], [12] Second, additive manufacturing uses a bottom-up fabrication method. The building up of the required materials from the substrate to the top of the device means that, in most cases, only the essential material is used to create each device. Traditional, top-down fabrication methods rely on material removal through masking and etching processes that result in a significant amount of material waste. This is particularly concerning when considering the prevalence of rare earth materials in many energy harvesting devices, energy storage devices, and a wide range of sensors. A large volume of hazardous effluents are also typically a byproduct of top-down device fabrication. [7] Third, many traditional fabrication techniques require energy intensive fabrication environments such as high vacuum or high heat for each step of the process. In contrast, most direct printing occurs in ambient conditions, reducing the overall energy required for device manufacturing and increasing the range of usable materials to include those that are incompatible with traditional fabrication methods. [12]

When prototyping transitions to large-scale device fabrication, many direct printing methods transition well to roll-to-roll or on-web printing. This printing method encompasses a continuously moving substrate with layer-by-layer material build. The deposition methods range from large-area, uniform thin film coating to high-resolution patterning, depending on the type of print-head selected. Furthermore, roll-to-roll printers can move at web speeds up to 200 m/min, resulting in an efficient, high-throughput manufacturing method. [13] The overall reduction in materials and energy usage, increased speed of moving from prototyping to large-scale production, and rapid

fabrication enabled by certain printing methods are all justifications for utilizing direct printing and expanding upon the known capabilities of additive manufacturing.

The instruments that enable scalable, additive manufacturing are certainly a critical component of in this complex field but the printable materials required to make a full range of functional devices are equally important. The ever-expanding variety of possible devices to print requires an equally diverse library of printable materials. Additionally, the push to fabricate perpetually smaller computer chip components, such as transistors, or completely change the method in which these chips function, such as the turn towards optical and quantum computing, has subsequently driven the field of additive manufacturing pursue higher resolutions for printed materials and to expand the range of materials that can meet the high-resolution standards. [7]

The motivation for the research presented here stems from the need to have high-resolution printed materials for next generation printed devices. The most promising high-resolution printing method is electrohydrodynamic inkjet (EHD) printing as it combines many of the benefits of other drop-on-demand, additive manufacturing methods such as traditional 3D printing and piezoelectric inkjet printing, but at higher printing resolutions than are typically achievable with those methods. New printing solutions are needed to be compatible with EHD printers in order to make optical device components and the insulating and semiconducting features of micro-electromechanical systems (MEMS). [14], [15] EHD printing also shows promise as a method for scalable nanomanufacturing. By using multiple printing nozzles simultaneously, large area high-resolution printing can be achieved. The success of this research space is vital to the field of printed electronics and continued advancements in printable materials research is essential to a future where scalable, additive nanomanufacturing is a thriving industry sector.

The goals of this research can be broken down into five distinct areas. One, expand the knowledge of the EHD printing tools as it pertains to the material properties of the printing formulations. Two, investigate the impacts of material properties and the printing formulation-to-printer interactions on the final printed feature. Three, develop novel printing formulations to meet the requirements of the materials needed for meta-optical devices; specifically high refractive index low absorption materials such as TiO_2. Four, print higher resolution features than previously reported in scientific literature for TiO_2 or any ceramic material. Five, combine the advances made in the printing formulations, substrate surface energy modifications, and instrument knowledge with the optimized meta-optical and photonic device designs to create fully printed and functional, planar light sensors and sensor components on the micro and nano scale using scalable nanomanufacturing techniques.

1.2 ORGANIZATION

This dissertation is divided into three primary chapters that discuss the need for and benefits of high resolution electrohydrodynamic inkjet (EHD) printing, methods for developing novel formulations compatible with EHD printing, and examples of applications of these materials and methods in the burgeoning field of EHD printed optical and photonic devices. Chapter 2 goes in depth on the function of EHD printers, the benefits of this fabrication method over traditional methods, and the state of the field with respect to functional oxide and particle-free printing formulations. Chapter 3 presents the research into the material properties of the printing formulations and the impact of those material properties on the observable printed structure. The objective of this chapter is to shed light on the myriad of material properties that impact the final printed structure while providing direction for future printing formulation development. Chapter 4 discusses the applications of the materials presented in Chapter 3 with a specific focus on meta-

optical and photonic devices. The results of the first fully printed meta-optical lens are presented along with the current state of the research into the next generation of fully EHD printed photonic devices.

1.3 BIBLIOGRAPHIC NOTE

This dissertation is based upon the following publications:

1. Holly J. C. Brunner, James Whitehead, Ricky Gibson, Joshua L. Hendrickson, Arka Majumdar, and J. Devin MacKenzie. *Fully Additive Electrohydrodynamic Inkjet Printed TiO_2 Mid-Infrared Meta-Optics*. Adv. Mater. Interfaces **2022**, 9(9), 2200149. DOI: 10.1002/admi.202200149
2. Holly J. C. Brunner and J. Devin MacKenzie. *Inorganic-Organic Hybrid Inks for Attoliter Scale Electrohydrodynamic Inkjet Printing with Applications in Meta-Optics and Printed Photonics.* ACS Appl. Mater. Interfaces **2022** (submitted).

Chapter 2. BACKGROUND ON ELECROHYDRODYNAMIC INKJET PRINTING

High resolution additive manufacturing is a broad term, and the range of applications is equally expansive. Direct-write printing is a subset of additive manufacturing that makes use of 2D or 3D patterns in order to have point-by-point control over material deposition in either two or three dimensions. [7] The relative ease in changing the print pattern, thus changing the subsequently printed device, makes direct-write printing methods incredibly versatile and optimal for rapid prototyping. There is also the possibility of parallel direct-write printing systems that would print an identical pattern, simultaneously, using multiple printer nozzles controlled by one printing script. [16] This in combination with a roll-to-roll system is the next step in scaling up direct-write printed devices. [17]

One form of direct-write printing that has the potential to significantly disrupt the field of micro and nanofabrication, is electrohydrodynamic inkjet (EHD) printing. EHD printing has similarities to other direct-write printing techniques, such as traditional inkjet printing and 3D printing, but with the addition of an electric field applied between the nozzle tip and the printer stage. This enables EHD printing to achieve printed material resolutions well below that which was achieved by traditional inkjet printing or 3D printing. In the case of traditional inkjet printing, fluid surface energy constraints make it difficult for this technique to reach below the picoliter droplet size and 10 μm printed feature size regime without the use of additional patterning. [9] There is also a significant limitation on the viscosity of the printing formulation used in piezoelectric inkjet printing. This severely constrains the types of materials compatible with this method and subsequently limits the devices and forms that can be printed. Extrusion or filament-based 3D printing requires contact between the nozzle, extruded material, and substrate to facilitate

printing. Without additional processing, this limits the printing resolution to the nozzle diameter or larger, depending on the material. [18], [19]

2.1 Electrohydrodynamic Inkjet Printer Functions

EHD printing is a rapidly advancing fabrication technique used to additively print functional materials with micron and submicron precision. The applied electric field between the printing nozzle and the substrate stage serves as a driving force necessary to create a fluid flow, or jet, to enable printing. [20] EHD printing can produce directed femtoliter, or smaller, size droplets from solution-borne functional materials with a broader range of viscosities than conventional, pressure-actuated inkjet printing. This is accomplished by using an applied electric field on polarizable fluids to overcome energetic barriers to smaller droplet formation. In contrast to extrusion 3D printing, EHD is a noncontact printing technique. The space between the printing nozzle and the substrate facilitates solvent evaporation of the ejected drop, reducing the volume prior to contact with the substrate. [18] Coupled with optimally engineered materials, EHD printing can provide many benefits over traditional micron-scale fabrication techniques, including large area photolithography, two-photon resist direct write lithography, and electron beam lithography. [20], [21] While lithographic techniques can achieve very high resolution and good reproducibility, they are typically indirect or subtractive and pattern transfer is done with an intermediate, sacrificial material, not the final product. In most cases, the processing produces significant waste fractions and is challenging and expensive to scale to large area and high-volume manufacturing. As such, these methods are typically limited to high value per area devices, such as microchips for advanced electronics. Furthermore, EHD printing is a significantly faster fabrication method

compared to e-beam lithography and two-photon resist direct write lithography, increasing the potential for scalable micro and nanomanufacturing. [7]

There are several variations of EHD printers along with multiple printing modes under which each printer can operate. EHD printers can function with or without the presence of a syringe or nozzle pump that applies pressure to the printing solution in combination with the applied electric field that is characteristic of EHD printers. With the presence of a syringe pump, the EHD printer can function in modes that are similar to extrusion-based 3D printing and can result in ink discharging from the nozzle with little to no contribution from an applied electric field. [9], [22], [23] This may be beneficial for large-area or large-volume EHD printing applications, but high-resolution printing can be achieved without a syringe pump. Therefor it does not appear to be a necessary instrument component. **Figure 2.1** shows a wide view schematic (a) of an EHD printer setup and a close-up schematic (b) of the EHD printer nozzle and the substrate. The close-up view

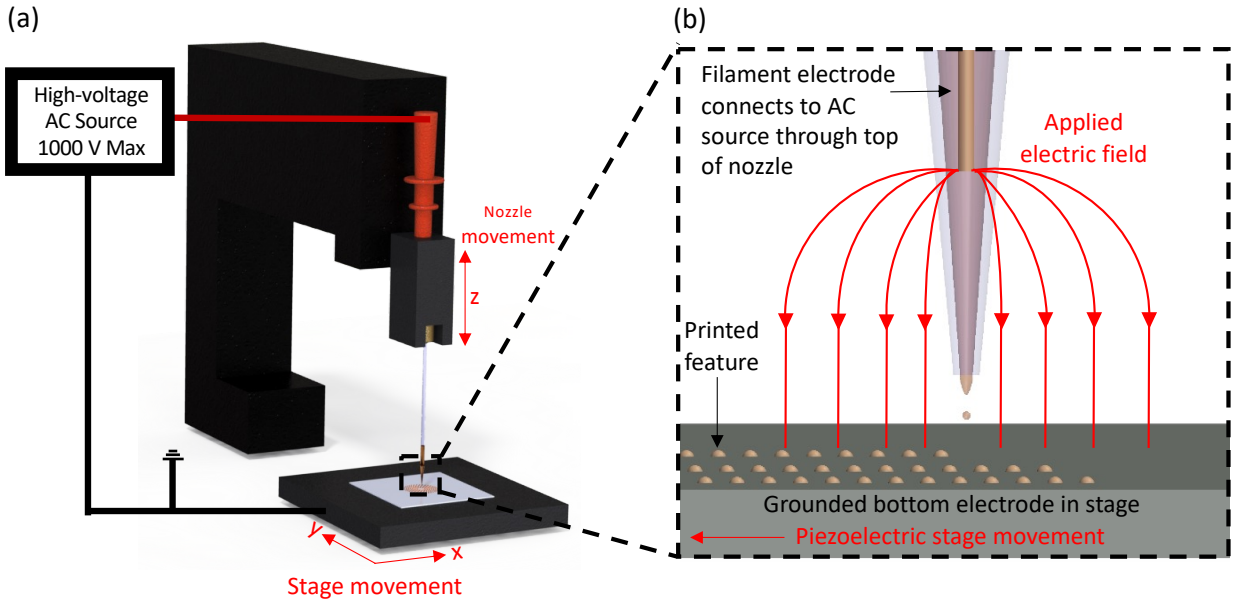

Figure 2.1. (a) Wide-view schematic of EHD printing set-up showing the degree of freedom of the nozzle and the stage. (b) Close-up schematic of EHD printing nozzle and substrate with approximated electric field lines.

indicates the approximated electric field lines for this variety of internal electrode nozzle. Previous studies have modeled the electric field lines around an internal electrode nozzle indicating that they primarily emanate from the central electrode and are normal to the ground electrode, thus compatible with this depiction. [16]

The printing nozzles used in EHD printers usually function made in one of two ways. Method one involves using either a metal nozzle [22], [23] or uniformly coating the outside of nozzle with a thin layer of conductive material, usually gold. [5], [12] This creates a conductive pathway from the nozzle head to the nozzle tip, enabling the formation of an electric field between the nozzle tip and the stage. The other primary method includes a conductive filament that runs along the inside of a glass capillary nozzle. The filament creates a conductive pathway from the top of the nozzle to a point near the nozzle tip. The filament intentionally ends a few millimeters before the nozzle opening to change the electric field foci to be further away from the printer stage. Depending on the electrical conductivity of the printing formulation, the ink also acts to a greater or lesser degree as a continuation of the internal electrode, shifting the foci of the electric field to the nozzle tip. This results in a stronger electric field at the nozzle tip for highly electrically conductive inks compared to weakly conductively inks. [16]

The inner diameter of the nozzle opening impacts the size of the cone-jet that forms upon the application of the electric field. This has the effect of changing the volume of the drops that break off the formed jets. The smaller inner diameter nozzles result in smaller ejected drops. [12], [20] However, as nozzle openings become narrower, the nozzle clogging becomes more likely. This is of particular concern for printing solutions that include nanoparticle suspensions. Using a particle free printing solution can help mitigate nozzle clogging but not all desired results can be achieved with particle free systems

The nozzle tip-to-stage distance (nozzle height) is an important parameter to consider in EHD printing and there are two competing factors at play when using the nozzle height to adjust the printed feature size. The region between the nozzle tip and the substrate serves as a space for the ejected drop to reduce in volume due to solvent evaporation, prior to reaching the substrate, resulting in a smaller printed feature. However, increasing the distance between the nozzle tip and the substrate, increases the required electrostatic force to draw the solution out of the nozzle. The larger electrostatic force results in a larger liquid cone pulled from the nozzle, larger drops breaking away from the electrified jet, and an increased likelihood of the formation of satellite drops. [24], [25] The optimal nozzle height is likely material dependent. Printing solutions made with a lower boiling point, more volatile, base solvent may benefit more from the increased evaporation time available with greater nozzle height. While printing solutions made with a higher boiling point, less volatile, solvent may benefit more from the smaller liquid cone with smaller break away drops that occur with a lower nozzle height. It is also possible that other printing formulation material properties such as viscosity, thixotropy, relative permittivity, and others impact the optimal nozzle printing height by changing the shape of the liquid as it exits the nozzle. Section 2.3 will discuss the state of research from the perspective of the electrified liquid and how that impacts the liquid cone formation and cone break up. However, a thorough investigation into the possible material dependent nature of the nozzle tip-to-stage distance has not yet appeared in the literature and the competing factors that influence the volume of the drop reaching the substrate is yet another example of the research that needs to be conducted into the complex material-EHD printing parameter relationship. The research presented in Chapter 3, and submitted for publication earlier this year, [26] begins to address several of the complex material-EHD printing parameter relationships that are not yet fully understood. This work does not specifically investigate how

different material properties impact the optimal printing nozzle height, but it does investigate the impact of a range of material properties on the final printed feature, not just the shape of the liquid as it leaves the nozzle. This distinction is important as some of the findings, specifically the impact of the printing formulation viscosity and surface tension, contradict previous work [24], [25], [23] solely focused on the ejected drop rather than the final printed feature. As it stands, it is clear that the nozzle height is an important parameter to consider but it cannot be said that all printing formulations should be printed at the same distance from the substrate.

The EHD printer operates under two primary electrical current conditions. When functioning exclusively with a direct current (DC), a constant voltage is applied between the EHD printer nozzle electrode and the stage. The polarizable printing solution responds to the presence of the electric field and is drawn out of the nozzle. The applied voltage required to overcome the energetic barrier keeping the fluid inside the printing nozzle, varies based on a wide range of material properties. The dominant forces acting on the fluid as it leaves the nozzle, depicted in **Figure 2.2** (a), are the hydrodynamic force (F_h), the capillary force (F_γ), and the electrostatic force (F_E), which is a combination of the normal ($F_{E,n}$) and tangential($F_{E,t}$) force vectors. This figure shows that in the presence of an electric field, a polarizable liquid responds with a buildup of charge on the fluid surface. This charge movement towards the surface results in electric normal stress ($\tau_{E,n}$) and the movement of the charge on the surface to maintain the surface charge results in the electric tangential stress ($\tau_{E,t}$). [23] If there is sufficient charge buildup, a constant and elongated cone (Taylor Cone) can form and the resulting printed drops are due to the fluid instabilities that occur at the cone tip as a result of the combined effect of the hydrodynamic, viscous and electrostatic forces. [25]

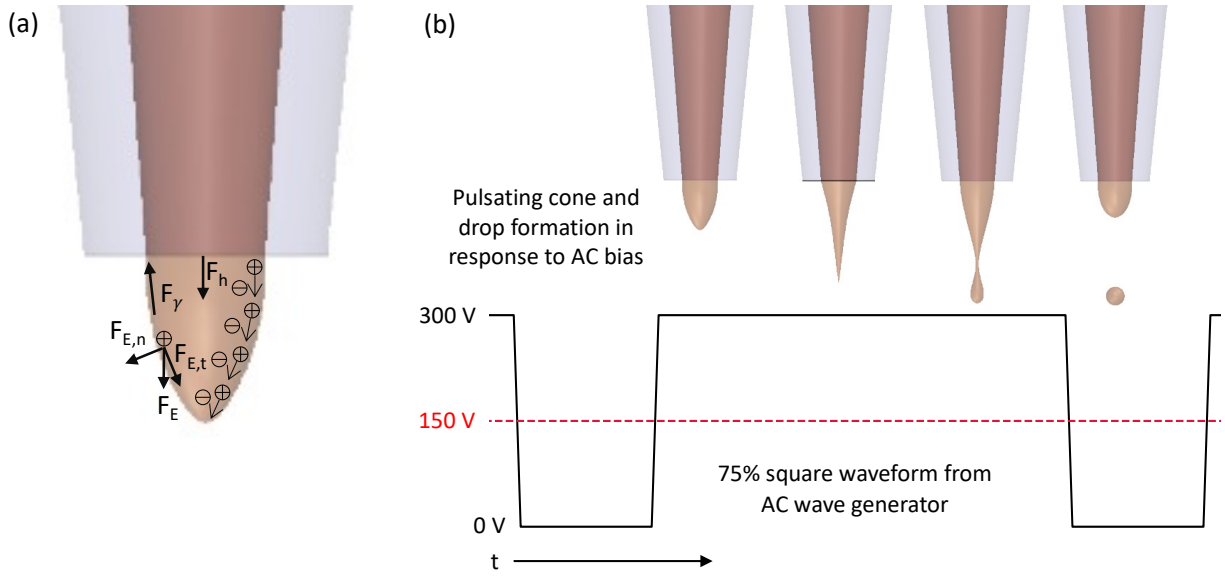

Figure 2.2. (a) Schematic of the nozzle tip with the approximated liquid cone shape corresponding to the applied 75% square-wave used to stimulate droplet ejection during printing. (b) The forces acting on the liquid at the nozzle tip and the movement of charge in response to the applied electric field.

Figure 2.3 shows the range of shapes the liquid printing ink can take upon exiting the nozzle. From the dripping mode (Figure 2.3 (a)) to the Taylor Cone/cone jet mode (Figure 2.3 (c)), increasing the electric potential results in an increasingly narrow liquid cone. The shape of the liquid as it is drawn out of the printing nozzle is also dependent on the strength of the applied electric field, along with other material properties. [23], [27] Past the Taylor Cone threshold voltage, it is common for off-angle, satellite drops, and spray-style printing to occur (Figure 2.3 (d)). It is important to note that the studies from which these images are based on use large nozzles with inner diameters between 0.2 mm and 1 mm. This is substantially larger than the nozzles used for high resolution EHD printing, which typically range from 0.5 µm to 10 µm. The nozzles are also observed at offset distances that are substantially larger than what is typically used for high resolution EHD. Larger nozzles and larger offset differences make it substantially easier to image

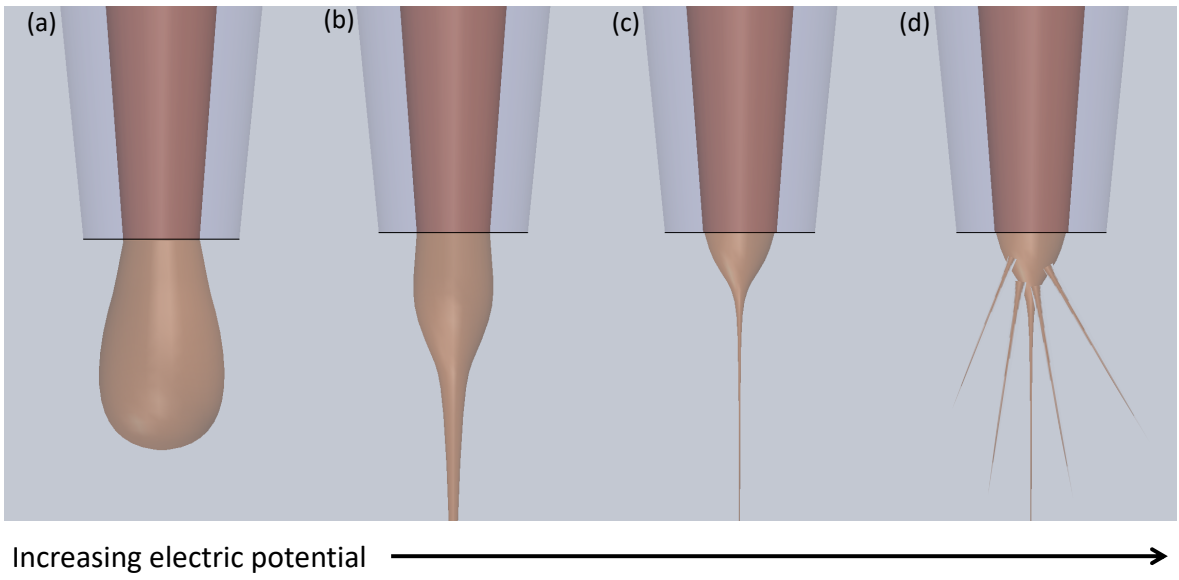

Figure 2.3. Four primary EHD ejection modes as a function of increasing electric potential (a) dripping mode, (b) pulsating more, (c) Taylor Cone jet mode, (d) multi-jet/spray mode.

the fluid that is drawn from the nozzle. Images of these nozzles can be taken with traditional high resolution and high-speed cameras or make use of light strobing imaging techniques commonly used in piezoelectric inkjet printing. [16], [28], [29], These imaging techniques are not readily available for high resolution EHD printing nozzles. This is a result of the rapidly evolving dimensions relevant to EHD printing liquid jet analysis are at a scale approaching the diffraction limit of light in often low optical density materials. The narrower printing offset distance (nozzle height) adds an additional layer of complexity to imaging high resolution EHD. Until these issues are addressed, there will continue to be questions about the true ejected drop volume, mode, and shape of high resolution EHD printed materials under any printing conditions and the hypothesized fluid shape or mode will be based on models and larger scale examples.

The EHD printer can also function exclusively with alternating current (AC). When functioning in this mode, an electrical current waveform generator coupled to the printer nozzle applies an AC voltage. This creates an electrostatic perturbation in the printing solution which

leads to drops jetting from the nozzle. The applied AC voltage can be tuned to each printing application by changing the waveform, amplitude, and frequency. Each AC wave component impacts the ejected drop in a variety of ways including average drop volume, consistency of drop volume, ejection frequency, and breakup of the electrified drop. Figure 2.2 (b) shows a schematic of a representative nozzle and printing fluid responding to an AC 75% square wave. the EHD printers can also operate with a DC and AC component. Under this hybrid mode, there is a constant DC voltage between the nozzle and the stage, and the variable AC voltage oscillates around the DC component. There is not yet a consensus in the literature as to which mode (DC, AC, or hybrid) results in the highest resolution printed features or greatest control over localized drop placement but there are some advantages in printing with an AC component. The constant and uniform direction of a DC voltage can result in a significant buildup of charge on the substrate and printed droplets resulting in altered droplet dynamics. This is of particular concern when working with insulating or weakly conducting substrates and inks. The buildup of charge can result in substrate conditions that vary with printing time and in some instances result in drops deflected from the target printing location. [29] In contrast, when using an AC voltage, the polarity switches at regular intervals resulting in a net zero total voltage over time. This mitigates unintended charge buildup and increases the range of printing materials and substrates compatible with EHD printing. [12] In the hybrid mode, where an AC voltage is overlayed a DC voltage, the jetting behavior tends to follow that of the dominant voltage source. For example, in the study by Tran et al. they tested the jetting behavior of hybrid printing conditions where the AC voltage is larger than the applied DC voltage and the reverse, where the DC voltage is larger than the AC voltage. Their results showed that the jetting and flight pattern of the drops followed the pure AC mode, when the AC voltage was larger, and the pure DC mode when the DC voltage was large. [30] Notably, the best results

from the research conducted for this dissertation, presented in Chapter 3, were achieved using the hybrid mode with a larger AC voltage than DC voltage.

In addition to the different electrical current conditions, the EHD printer can function under two different drop ejection modes: the continuous jetting mode and the dropwise mode. For additive printing of complex patters, such as those required for meta-optical lenses, it is essential to use a process with precise control of over the location and volume of the deposited material. In EHD printing, the method of continuously printing a solution can result in high resolution printed features, but the method does not provide the level of drop size and location precision necessary to fabricate quasi-periodic or aperiodic patterns. The dropwise EHD printing method uses point-by-point control of printing parameters. In this mode, the location and pitch of each drop is controlled by pausing droplet ejection during discrete stage movements before resuming ink flow at a defined location. The volume of the ejected drop is controlled by the parameters set at each point, including the duration of ink ejection.

Understanding the impact of the electrostatic forces on the printing solution in an EHD printer is a non-trivial area of research. Optimizing the printing parameters that dominate the electrostatic force component in order to achieve the printing objective is a critical step of any EHD process. More broadly, determining the dominant variables and material properties that lead to the size and shape of the jetting streams of charged liquids, the volume of the ejected drop, and the final printed feature is an enduring area of research for this field. In part, this is due to the multi-variable problem that is EHD printing and the extensive combinations of interacting materials as well as the challenges associated with directly imaging the liquid jets.

2.2 Electrified Liquid Jet Breakup Theory

Collins et al. conducted an expansive computational study on the factors impacting the breakup of electrified jets. The simulations are based on perfectly conducting, incompressible Newtonian liquids and models were developed to compare stream breakup time, droplet Coulombic stability, and the properties of the satellite drops that frequently occur alongside the primary drop to other variables such as electrical Bond numbers, disturbance wave numbers, and the ratio of viscous to cohesive force. Satellite drops are smaller drops that occur in tandem with the primary drop. The investigation into the conditions that result in the formation of satellite drops as well as the size ratio of the primary drop to the satellite drop while impacted by the presence of an electric field is particularly valuable for high-resolution EHD printing. Models in this paper show that jet breakup time is impacted by the wavenumber of the electrostatic stresses. The electrified jet breakup time increases both as the wavenumber increases and decreases, with a minimum occurring at the transition point between longer and shorter waves. This trend holds true for a range of liquid viscosities and charge states but the transition point changes based on viscosity and the ratio of electrostatic to hydrodynamic force. [25] These simulations, and others, provide valuable insight into which material properties and printer variables to consider when conducting experimental research to develop the novel printing solutions required to achieve the goal of high-resolution direct write printing. However, a significant limiting factor in directly applying the modeled results to experimental results is the difference between the perfectly conducting, incompressible Newtonian fluid in the model and the imperfectly conducting and in some cases non-Newtonian fluids used as printing inks. As such, continued research into the presence of modeled trends in experimental results and the optimal methods in which to the apply insight gained through simulations is necessary to expand the capabilities of EHD printing.

2.3 Electrohydrodynamic Inkjet Printing Materials and Applications

The EHD printing techniques and compatible materials present a unique combination of benefits, including rapid prototyping and fabrication, maskless lithography, ambient condition fabrication, and a wider range of material types including metal salt [31] and metal nanoparticle based inks, [18] carbon nanotube and graphene inks, conductive polymers, [32] photopolymers, [24] suspended quantum dots [33], and many other varieties of materials in a range of viscosity from less than 10 centipoise (cP) [34] to at least 5000 cP. [24], [35] Additionally, most EHD printed devices can be fabricated without the assistance of chemical etchants, thus reducing overall resource use and toxic effluents from the process. [34] EHD printing techniques have already been used to successfully print a wide range of materials; however, much of the focus in the field, including the reported highest resolution printed features, involved metal nanoparticle inks or UV-curable polymers. [21], [24] There has been significantly less emphasis on materials and process development for EHD printed ceramics, semiconductors and inorganic-organic hybrid materials.

Ceramic and semiconducting materials, such as TiO_2, are of particular interest for applications in meta-optics [36], [37] and MEMS devices due to the optimal combination of material properties such as a high refractive index, [38], [39] low absorption over a broad wavelength range, including the visible, near-infrared, and mid-infrared spectrum, [40] low signal losses, increased efficiencies, [37] and mechanical and thermal robustness. As such, there is significant motivation to develop high-resolution printable ceramics to bring the benefits of printed electronics to optical devices and MEMS. Previous work by Duoss et al. used an extrusion-based 3D printer to print a very high viscosity TiO_2 alkoxide precursor and polymer filament to fabricate structures with possible optical device applications. This process, however, requires a sacrificial layer to enable post printing sintering and condensation to achieve their final reported minimum feature size of

268 nm ± 9 nm. [41] This significantly limits the types of structures and devices that can be printed and is not appropriate for meta-optical lenses, optical resonators, nanostructure anti-reflective coatings, or MEMS. Meta-optical lenses, specifically, rely on 2D arrays of sub-wavelength structures. These scatterer structures must remain well adhered to the substrate and maintain the optimal pitch to focus light. [42] As such, an alternative direct-write process and compatible printing solutions are needed to create a viable fabrication method to achieve fully printed, high-resolution optical device components.

The process of developing a novel printing solution for EHD is a multifaceted endeavor that requires consideration of the printer constraints and function, substrate properties, post-printing processing, and final device function. As mentioned previously, EHD printing makes use of an applied electric field in order to draw the printing solution out of the nozzle. This method requires that the printing solution has some degree of polarizability. The printing solution must allow a charge to build up at the extrusion point and is therefore drawn towards the substrate. [22] It is important to note that the base solvent of a printing solution does not need to be polarizable if it contains suspended particles that can be polarized such that the overall system produces a response to the presence of an electric field. [33] The presence of the electrostatic forces that enable printing of femtoliter drops also creates a dynamic printing environment where changes in the printing parameters result in measurable changes in the material properties which has a different response to the new printing parameters than would be observed if the material properties remained constant.

An example of this printer parameter induced material property variation is the impact of the AC voltage frequency and the relative permittivity of the printing solution. The relative permittivity, or dielectric constant, of a liquid is a relative measurement of the liquid's chemical

polarity and can be interpreted as the degree to which a liquid responds to the force of an electric field. [22] The static permittivity (ε_s) of a material can be determined by measuring its capacitance (C) at a known distance (D) with the known area (A) of a parallel plate capacitor (**Equation 2.1)**.

$$C = \varepsilon_s(\frac{A}{D}) \tag{2.1}$$

The static permittivity is a complex, frequency dependent material property and determining this value allows one to calculate the relative permittivity (ε_r), which is given relative to the permittivity of free space ($\varepsilon_0 = 8.85418782 \times 10^{-12}\,\frac{F}{m}$) (**Equation 2.2)**.

$$\varepsilon_r(\omega) = \frac{\varepsilon_s(\omega)}{\varepsilon_0} \tag{2.2}$$

Going back to the example of the printing solution in the EHD printer, assuming all printing parameters remain constant, changing only the frequency of the AC voltage also changes the relative permittivity of the printing solution. This results in the solution having a different response to the constant DC voltage and a different response to the amplitude of the AC waveform. The interrelated nature of the different printing parameters that impact the overall electrostatic force on the printing solution makes isolating the impact of each variable challenging. It also serves as motivation to conduct research into the individual impact of each EHD printer parameter on the printing solution and the collective impact of these parameters on the ejected drop.

Outside of the material properties that respond directly to electrostatic forces, there are a wide range of material properties that significantly impact the geometry of the final printed feature and the overall usability of a given printing solution. Some of these critical material properties include the surface tension, contact angle between the printed liquid and the substrate, viscosity at room temperature, viscosity at elevated temperatures, density, the hydrogen bond count, boiling point of the primary solvent, and usable printing time. The impact of some of these material properties have been investigated and are presented in literature but there does not exist a thorough

investigation on the combined impact of these material properties on final printed drop geometry. A previous experimental study that focused on properties such as the relative permittivity, surface tension, and viscosity, only considered the properties of pure solvents and assessed the solvents based on the shape of the electrified jets with minimal examples of the final printed solution. [22] Another study investigated the impact of printing liquid viscosity on the ejected fluid shape by varying the ratio of high viscosity terpineol with low viscosity ethanol. Again, this study only focused on the ejection shape and mode and did not discuss the printing outcomes as it pertains to the final printed feature dimensions. [23] While understanding the impact of these parameters on the jetting modes is important, understanding the impact of these properties on the dimensions of the final printed material is crucial to developing reliable EHD printing methods that can be used to make fully printed and functional devices. Chapter 3 of this dissertation is dedicated to determining the impact of key material properties on the final geometry of the printed features of alkoxide precursor based EHD printing solutions.

Chapter 3. PARTICLE FREE TITANIUM ALKOXIDE INKS FOR HIGH RESOLUTION ELECTROHYDRODYNAMIC INKJET PRINTING

The process of developing a novel printing formulation for EHD printing is a multifaceted endeavor that requires consideration of the printer constraints and function, substrate properties, post-printing processing, and final device function. There are a wide range of material properties that significantly impact the geometry of the final printed feature and the overall usability of a given printing solution. [9], [12], [22] Some of these critical material properties include the surface tension, contact angle between the printed liquid and the substrate, viscosity at room temperature, viscosity at elevated temperatures, density, the hydrogen bond count, boiling point of the primary solvent, relative permittivity, and usable printing time. [23], [25], [43] The impact of some of these material properties have been investigated and are presented in literature but there does not exist a thorough investigation on the combined impact of these material properties on final printed drop geometry. The research presented in this chapter aims to close that knowledge gap and shed light on the ways in which printing formulations should be tailored to meet the printing objectives.

3.1 RESEARCH OBJECTIVES

In addition to the broader objectives to expand general knowledge in the space of EHD printing with a focus on EHD printed oxides, there are several specific objectives guiding this research. First, in order to meet the demand for high-throughput micro and nanoscale devices, the initial objective of this research is to achieve the highest-resolution ever reported EHD printed TiO_2 feature. The metric used to define highest-resolution is the x-y area covered by the EHD printer deposited material. Prior to the start of this research, the smallest ever reported EHD printed

TiO_2 feature was a line of material with a linewidth on the order of 100 μm. [14], [44] If this objective is expanded to include EHD printing of all metal oxides, examples of the smallest reported features are a SnO_2 precursor capable of printing a 5 μm wide line and an In-Ga-ZnO solution capable of printing features in the 2-7 μm range. [15], [45] Developing the materials and methods to print TiO_2 features below 2 μm would surpass the existing standard for EHD printed metal oxides.

The second objective of this research is to go beyond the smallest ever reported feature and develop a method for printing sub micrometer wide TiO_2 features. Achieving this objective would provide the resolution necessary to print optical device components tailored for near and mid-infrared wavelengths with the prospect of meeting the requirements to print optical device components tailored for wavelengths in the visible spectrum.

The third and fourth primary objectives are to print 1 μm tall features such that 1 μm wide features have a 1:1 aspect ratio and to develop a consistent and precise process that results in accurately printed patterns of features with a narrow size distribution. The fifth and final primary objective is to create a fully printed, functional optical device based on the materials and processes developed for the previous objectives.

Several of these objectives have been achieved and the associated research is presented in subsequent sections and chapters of this dissertation. Significant progress has been made on the remaining objectives and those research findings are also presented. Advancements were made beyond the initial objectives, expanding the range of applications for the materials and methods developed as part of this research and indicates that high-resolution EHD printed device research is a promising field with the potential to disrupt the optical device fabrication industry.

3.2 TITANIUM ALKOXIDE PRINTING FORMULATION DEVELOPMENT

The published research on EHD printed ceramic and inorganic-organic hybrid inks is limited, across applications, and it was determined that a novel printing solution would be required to meet the research objectives. As described in Chapter 2, the EHD printing solution development process is requires consideration of a wide range of variables alongside the impact of the printing process on the printing formulations. Titania alkoxide precursor-based inks are an appealing material system to explore for the continued development of EHD compatible printing formulations that result in TiO_2 features. The following material properties were investigated and the measured values compared to the final printed feature diameter: viscosity, surface tension, Ohnesorge number, contact angle, and relative permittivity. The effective printing window is also investigated to determine wider usability and scalability of the printing formulations. The collected data is used to determine what properties to prioritize when developing new printing formulations for high resolution printed features. This remainder of chapter is dedicated to determining the impact of key material properties on the final geometry of the printed features of alkoxide precursor based EHD printing formulations.

3.2.1 *Titanium Alkoxide Chemistry*

Low-reactivity titania alkoxides are a compelling material family to consider for novel EHD compatible printing formulations that result in solid TiO_2 printed features. Printed in pure form or in combination with other solvents and polymers, titania alkoxides provide a path to creating particle free ceramic printing formulations. However, metal alkoxides are much more reactive towards water compared to silicon alkoxides due to coordination expansion, i.e., the coordination number of the metal is higher than its valency. While this means that many metal alkoxides do not required a catalyst to enhance the alkoxide reactivity and convert into a solid metal oxide, the

reaction rate of a system could also be too high to result in a viable printing formulation. [46] When developing formulations for applications in additive manufacturing, it is critically important to design a system with a reaction rate that is compatible with the printing method. In EHD printing, it is usually of greater concern that the metal alkoxide will react too quickly, result in uncontrolled metal oxide precipitation and cause nozzle clogging or non-uniform printed features.

Highly reactive alkoxides, such as titanium ethoxide (Ti $(OCH_2CH_3)_4$), hydrolyze readily in the presence of water. There is sufficient water present in ambient laboratory conditions to result in ill-defined titanium-oxo/hydroxo precipitates due to unintended reactions between the alkoxide and the ambient water vapor. To create more stable precursors, a titania precursor with the form $Ti(OR)_4$ is reacted with a bidentate or multidentate complexing ligands, such as acetic acid or acetylacetone, to create a less reactive metal alkoxide. These complexing ligands are more strongly bonded and the exchange of one or more OR groups for a multidentate complexing ligand, results in a higher equilibrium constant (K) and thus a lower reactivity. In addition to lower reactivity, the chelated alkoxides show a decrease in crosslinking of the gel network. [46] The increased stability of multidentate titanium alkoxides suggests there are in a wide range of formulations likely to be compatible with EHD printing.

One such stable titania alkoxide is titanium diisopropoxide bisacetylacetonate (TDBA). This is a chelated titanium alkoxide which has octahedral coordination of two isopropoxide and two acetylacetonate groups about a central titanium atom. [41] This highly stable precursor is well suited for EHD printing due to its low reactivity under ambient conditions, compatibility with a range of organic polar solvents and polymers. A catalyst can be added to induce hydrolysis and condensation, resulting in a higher viscosity sol-gel solution, but a catalyst is not required to convert the alkoxide to titania. This process can happen through calcination at elevated

temperatures, with or without the presence of a catalyst in the original printing solution. For this reason, TDBA is regularly used in aerosol printing methods and spray pyrolysis. [47], [48] **Figure 3.1** (a) shows a molecular diagram of TDBA converting to crystalline TiO_2. A simple spin coat and sinter test was conducted to determine if this precursor converted as simply as described in literature. The TBDA used for this test is a 75 wt. % solution in isopropyl alcohol (IPA) (Sigma-

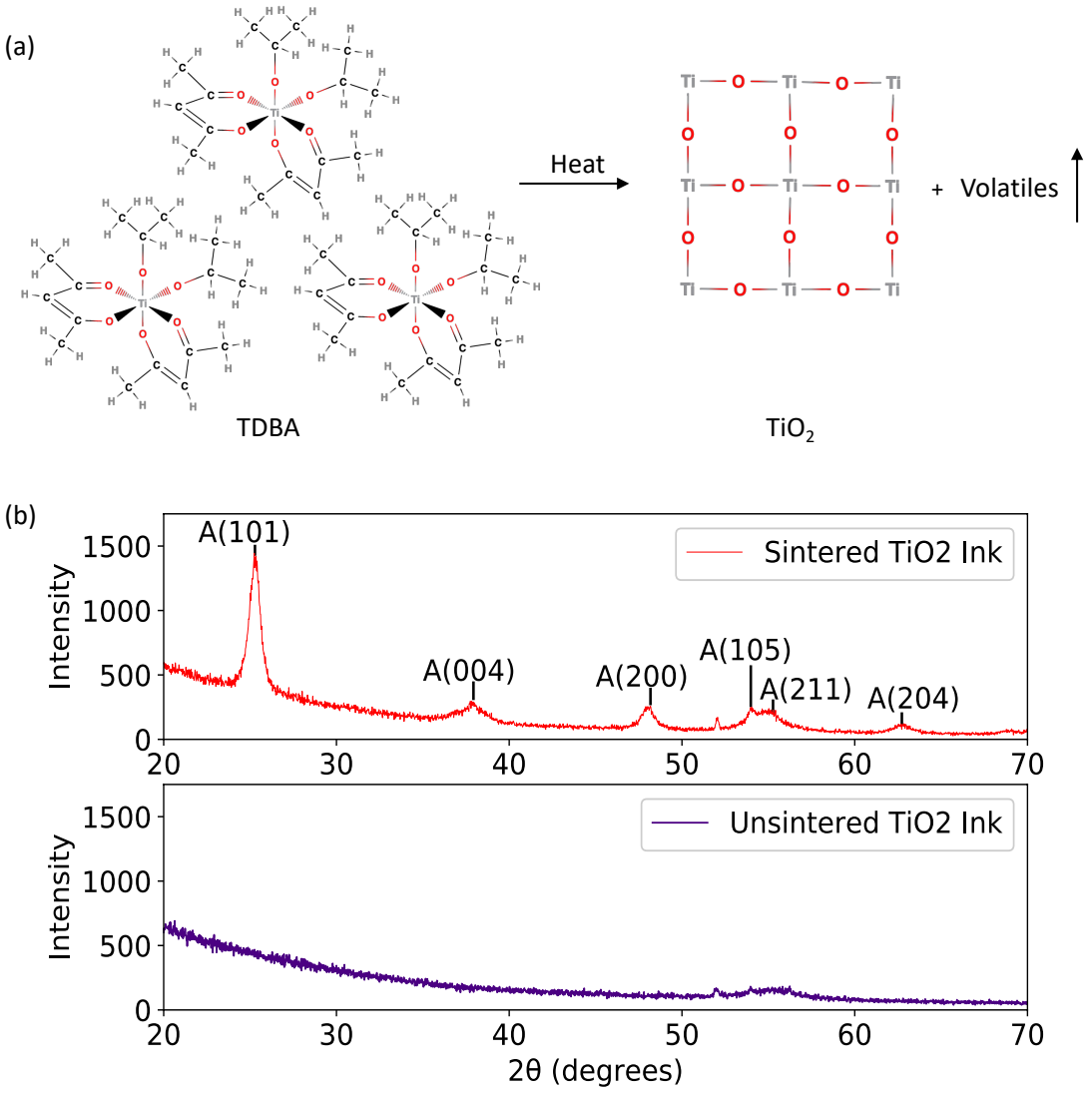

Figure 3.1. (a) Conversion of titanium diisopropoxide bisacetylacetonate (TDBA) to TiO_2 with the application of heat. (b) XRD of TDBA thinfilm before (blue) and after (red) high temperature sintering. The characteristic peaks of the anatase phase of TiO_2 are labeled.

Aldrich) and was spin coated onto a clean, polished silicon wafer. After spin coating, there is a low temperature drying step to evaporate residual solvent (75 °C for 10 minutes). The blue curve in Figure 3.1 (b) shows the collected XRD (Bruker D8 Advanced XRD) data of a TDBA thinfilm after the low temperature step. To test the conversion to crystalline TiO_2, the substrate is heated to 450 °C in a box furnace for 1 hour. The same XRD measurement is taken and the results are shown in the red curve of Figure 3.1. The sintered version of TDBA shows the characteristic peaks of the anatase phase of TiO_2, which is expected for the temperature used in the calcination step. The large number of stable combinations of precursor, polar solvent, and polymers along with the simple conversion process to TiO_2, makes TDBA an ideal material to use in the development of a novel alkoxide based printing formulation.

3.2.2 *Substrate Surface Energy Modification*

The substrate used for all EHD printing experiments is a polished n-type silicon wafer. Observations from the initial printing trials of TDBA with IPA showed total wetting of the solutions on silicon. In an effort to reduce printed drop spreading, thus decreasing the x-y area of the printed feature, substrate surface energy modification were investigated. Three methods were investigated for increasing the contact angle between the TDBA mixture and the Si substrate. A proprietary thinfilm hydrophobic coating by Aculon and two hydrophobic, self-assembling monolayers (SAM), trichloro(1H, 1H, 2H, 2H-perfluorooctyl)silane (FOTS) and octadecyltrichlorosilane (ODTS). [49], [50] The Aculon coating was suboptimal as it resulted in an observable thinfilm on the Si substrate and most importantly because the IPA and precursor locally dissolved the coating resulting in cavities in the thinfilm, rather than extruded features. The FOTS favorably changed the surface energy of the Si substrate without visually impact the substrate, resulting in an increase in the contact angle of TDBA on Si from 0° (total wetting) to ~ 64°. **Figure**

3.2 (a) shows the contact angle between the TiO_2 precursor printing solution and (b) the Si substrate with and without the FOTS surface treatment. The TDBA+IPA mixture printed on clean, uncoated Si (Figure 3.2 (c)) resulted in ~ 35 μm wide lines. Upon the addition of FOTS, the linewidth narrowed to ~10 μm, shown in Figure 3.2 (d). Most importantly, material printed on the FOTS coated Si remained extruded from the substrate. For the sake of comparison, a second hydrophobic monolayer was investigated, n-octadecyltricholorosilane (ODTS). The contact angle between TDBA in IPA and silicon coated ODTS is 35°. This is an improvement over clean, uncoated Si, but significantly lower than FOTS coated Si. Given the significantly higher contact angle on of TDBA on FOTS compared to ODTS and the greater than 3x reduction in the width of the printed feature, between the uncoated and hydrophobic SAM coated silicon, FOTS coating proved to be a valuable addition to reduce the printed feature size without compromising other research objectives. As such, an FOTS coating was used on all substrates for all subsequent printing.

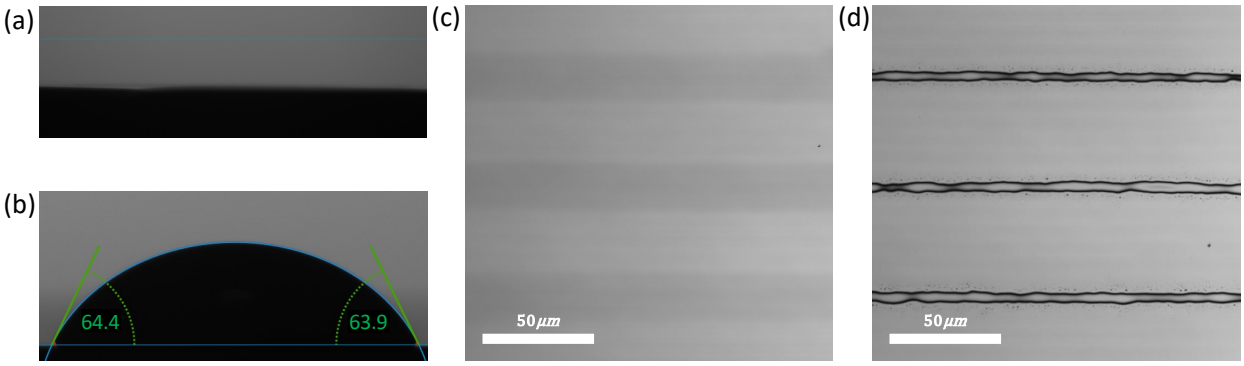

Figure 3.2. (a) Contact angle, showing total wetting, of TiO_2 precursor on clean Si substrate without any hydrophobic coating (b) Contact angle of TiO_2 precursor printing solution on clean Si substrate with the hydrophobic self-assembled monolayer coating (c) EHD printed TiO_2 precursor on Si wafer without the hydrophobic self-assembled monolayer coating (d) EHD printed TiO_2 precursor on Si wafer with the hydrophobic self-assembled monolayer coating.

3.2.3 *Benefits of Added Polymer*

The simple precursor and solvent system described above resulted in printed lines with a ~35 μm linewidth, meeting the preliminary objective to achieve printed lines narrower than 100 μm. However, the resulting lines had very little material buildup in the z-direction, only about 20 nm tall. Overall, the printed feature fell well below the 1:1 (height:width) aspect ratio outlined in the objectives. Additionally, several of the TDBA and IPA printing tests fractured during the solvent evaporation and calcination steps. In an effort to increase the printed feature aspect ratio and mitigate stresses that occur in post-printing solvent evaporation and calcination steps, a solution containing polyvinyl pyrrolidone was tested. Initially designed for extrusion based 3D-printing, this sol-gel formulation included TDBA as the TiO_2 precursor, PVP to mitigate stress from drying, ethanol and water as the primary solvents, and NH_4OH as a reaction catalyst. [41] The EHD printed features using this formulation showed significantly more material buildup in the z-direction (~500 nm) and no cracking. Plus the addition of PVP created a mechanism with which to change the viscosity of the original solvent + TDBA mixture without changing the other components of the formulation. However, the solution dried in the nozzle quickly, clogging the nozzle after less than one hour of printing. This rapid clogging is assumed to be caused by either the high vapor pressure of the primary solvents, ethanol and IPA, in combination with the presence of PVP, which resolidified upon the evaporation of the solvent or the combination of H_2O and NH_4OH which could be causing the titania alkoxide precursor to react too quickly to be compatible with EHD printing. To address this set of issues, a range of novel formulations were developed, and a set of standardized printing tests were run to determine the optimal formulation and optimal set of material properties to achieve the outlined objectives and to consider for future ink development research.

3.3 Printing Experiments

The basic requirements to be compatible with EHD printing are that the printing solution needs to be polarizable and the ink should easily flow out of the nozzle, allowing for approximately three hours of printing time or greater. A particle free approach to the TiO_2 printing solution was determined to be the best way to mitigate the issue of nozzle clogging, which is a significant concern for particle-based systems. Nozzle clogging, either through the collection of solution borne particles or solution drying at the nozzle tip, reduces the overall printable time of a given solution.

The nozzles used for this research are made of glass with a conductive filament on the interior and most printing tests were conducted with nozzles that have a 2 μm inner diameter at the tip. The narrow nozzle opening increases the likelihood of clogging. The preliminary research and existing literature highlight that a range of printing solution and interface properties impact the usable printing time and the printed feature geometry. However, it is unclear which solution properties lead to which printed results. From here, a robust study into the critical printing solution properties was developed in pursuit of achieving the outlined objectives.

The following solution properties were investigated to determine which properties have the greatest impact on reducing the individual printed feature size: solvent boiling point, contact angle between the printing solution and the substrate, viscosity, and relative permittivity. Six solvents were chosen for this study: ethanol, 1-butanol, ethylene glycol, 5-methylfurfural, propylene glycol, and 1,4-butylene glycol. The quality of the ink was measured based on the size of the printed feature under uniform printing conditions and the usable printing time.

3.3.1 *Ink Formulation Methods*

To make the printing solution, first, 0.625 g of PVP (~55,000 mw, Sigma-Aldrich) is added to a glass scintillation vial. Then 1.76 mL of one of the follow solvents is added to the vial: ethanol, 1-butanol, ethylene glycol, propylene glycol, 5-methylfurfural, or 1,4-butylene glycol (all Reagent Plus > 99%, Sigma-Aldrich) and 0.638 mL of IPA (ACS Reagent > 99.5%, Sigma-Aldrich). The PVP and solvents are stirred at room temperature, using a clean magnetic stir bar, at 600 rpm, until the PVP has fully dissolved, about 2-3 hours. Once the PVP is dissolved, 1.1125 g of titanium diisopropoxide bisacetylacetonate (TDBA) (75 wt. % solution in IPA, Sigma-Aldrich) and 0.125 g of poly(melamine-co-formaldehyde) methylated solution (~84 wt. % in 1-butanol, Sigma-Aldrich) , a thermally activated crosslinking agent, is added to the solution. The solution is stirred at room temperature for 24 hours. Upon removing the sample from the stir plate after the 24 hours of mixing is complete, the bulk solution is stored in air at room temperature. The final printing solution is made by taking 0.51g of the bulk solution and adding 0.51 g of the selected solvent and 0.48 g of titanium TDBA. This solution is mixed for 30 seconds using a vortex mixer at 2000 rpm. The subsequent materials measurements or printing tests are conducted shortly after mixing. Prior to printing, each ink is filtered through a 0.45 μm water-wetting polytetrafluoroethylene (PTFE) membrane syringe filter (VWR).

3.3.2 *Standardized Printing Methods*

The six inks are printed individually, under uniform conditions. All samples are printed on a commercially available, double side polished, n-type silicon wafer (University Wafer, Inc). The wafer is first cleaned via sonication baths in deionized (DI) water with 10% detergent, pure DI water, acetone, and IPA. Following sonication in IPA, the Si wafer undergoes a UV-ozone surface activation treatment for 10 minutes. Then the substrate is coated with FOTS (97%, Sigma-

Aldrich). The hydrophobic coating was applied in an enclosed environment on a hotplate set to 125 °C for two hours. After the application of the hydrophobic monolayer, two standard patterns were printed on the substrate using an EHD printer made by SIJ Technology, Inc., Japan; one using the continuous jetting mode the other using the dropwise mode. All patterns are printed with a 2 μm inner diameter nozzle purchased from SIJ Technology and are commercially available. The samples were printed under ambient conditions with the printing nozzle kept at a uniform height (approximately 10 μm). This distance is measured by using the tool's z-axis digital nozzle control. First, the nozzle is brought close to the stage until it is touching the substrate. Then, the nozzle is retracted by 10 μm. This distance is set at the origin of the printed region and the nozzle does not move in the z-axis while the pattern is printed. After printing is complete, the substrate was placed on a 200 °C (250 °C for 1, 4-butylene glycol) hotplate for 20 minutes. This is to enable the thermal crosslinking of the PVP and poly(melamine-co-formaldehyde) methylated, to evaporate the printing solvents, and convert the titania precursor to amorphous TiO_2. After the thermal crosslinking steps, the printed structures adhere well to the polished Si substrate, as tested through scratch testing and sonication in a solvent bath.

The continuous mode patterns were printed with a 75% square waveform, an AC voltage amplitude of 150 V, a DC bias of 150 V, AC voltage wave frequency of 400 Hz, and a stage speed of 3 mm/s. **Figure 3.3** shows the bulk solution of each different printing formulation along with a wide view and a close view of five of the six different inks printed in continuous mode. Ethanol ink is not depicted in this figure because the solution dried and clogged the nozzle so quickly that the basic printing patterns could not be completed. This occurred during multiple attempts and so it was determined that the rate of solvent evaporation was too high for ethanol based solutions to be a viable option for EHD inks.

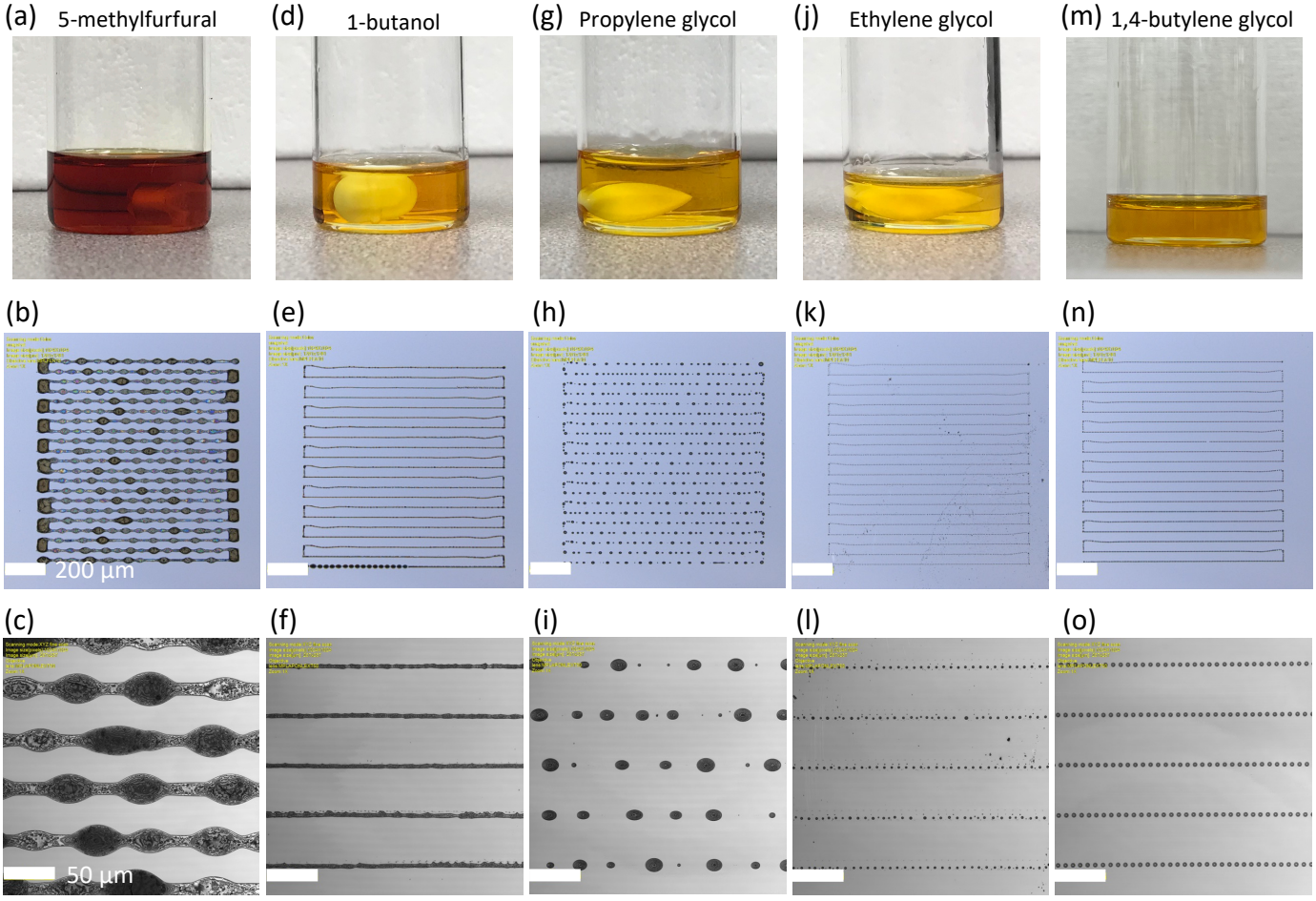

Figure 3.3. TiO_2 + PVP + solvent inks printed in continuous mode. Top row scale bar is 200 µm, bottom row scale bar is 40 µm. (a-c) 5-meyhylfurfural ink, (d-f) 1-butanol ink, (g-i) propylene glycol ink, (j-l) ethylene glycol ink, (m-o) 1,4-butylene glycol ink.

The dropwise mode patterns were printed with a 75% square waveform, an AC voltage amplitude of 150 V, AC voltage wave frequency of 400 Hz, a stage speed of 1 mm/s, and drop hold time of 0.001 s, the shortest amount of time allowed by the tool. **Figure 3.4** shows a wide view and a close view of the same set of inks printed in dropwise mode. After printing and drying, the samples were imaged using an optical profilometer (Olympus OLS4100) and the images were analyzed using Fiji, an open-source image processing software package for ImageJ2. Using Fiji, the average area of the individually printed feature in each array was determined. This value is

presented as the average feature width in and is used as the feature diameter value in the plots comparing the value of one material property to the resulting printed feature. The wide view images are taken with a 10x objective in the optical microscope imaging mode and the close view images are taken using a 50x objective, in laser scanning mode. The feature heights of the dropwise printed samples were measured on the optical profilometer, using the 50x laser scanning mode images, from there the average was calculated. Using Fiji, the average area of the individually printed features in each array was determined.

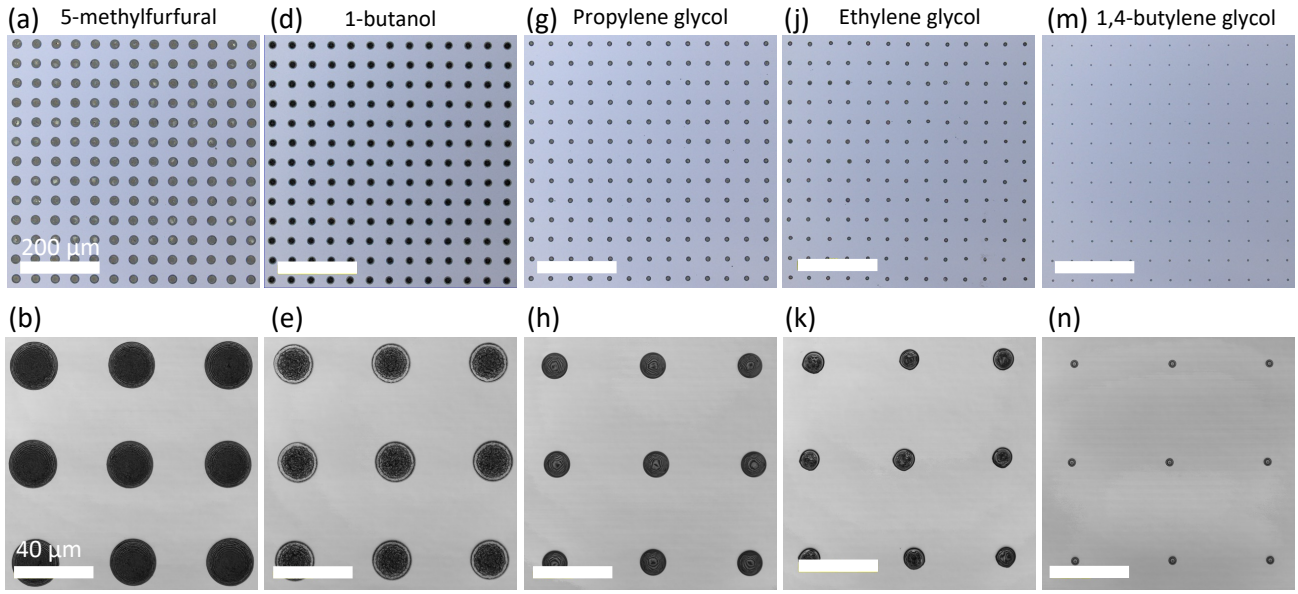

Figure 3.4. TiO_2 + PVP + solvent inks printed in dropwise mode. Top row scale bar is 200 µm, bottom row scale bar is 40 µm. (a), (b) 5-methylfurfural ink, (c), (d) 1-butanol ink, (e), (f) propylene glycol ink, (g), (h) ethylene glycol ink, (i), (j) 1,4-butylene glycol ink.

3.4 TITANIA PRINTING FORMULATION MATERIAL CHARACTERIZATION METHODS

3.4.1 *Viscosity*

Viscosity measurements were taken at 25 °C and 95 °C using an Anton Paar MCR302 rheometer with a 50mm cone-plate spindle. The measurements were taken of the pure solvents and the final printing solution made from each primary solvent at 25 °C, to approximate room temperature, and 95 °C. An elevated temperature was chosen that is below the boiling point of all the main solvents under consideration, with the exception of ethanol, but significantly above room temperature. Note that ethanol as a base solvent for an optimized printing formulation was ruled out early in this research due to the rapid nozzle clogging that perpetually occurred during printing. As such, the temperature used for the elevated temperature viscosity measure was selected without considering the constraints of the ethanol based printing formulation.

3.4.2 *Surface Tension and Contact Angle*

The contact angle and the surface tension measurements were taken using a Kruss drop shape analyzer. Contact angle and surface tension measurements were taken of the pure solvents and the final printing solution made from each primary solvent. The FOTS coated silicon substrates used in the contact angle measurements were prepared with the same procedure as the substrates used for the printing tests. The reported contact angle is the measurement taken just after the drop is incident on the substate. This measurement point was chosen due to the rapid solvent evaporation that occurs once the solution leaves the nozzle because of the high surface area of the printed feature. For surface tension measurements, a uniform drop volume of 10 μL was used for all tests.

3.4.3 *Relative Permittivity*

The relative permittivity (ε) of a liquid is a relative measurement of the liquid's chemical polarity and can be interpreted as the degree to which a liquid responds to the force of an electric field. [22] The static permittivity (ε_s) of a material can be determined by measuring its capacitance (C) at a known distance (D) with the known area (A) of a parallel plate capacitor (**Equation 3.1)**.

$$C = \varepsilon_s(\frac{A}{D}) \tag{3.1}$$

The static permittivity is a complex, frequency dependent material property and determining this value allows one to calculate the relative permittivity (ε_r), which is given relative to the permittivity of free space ($\varepsilon_0 = 8.85418782 \times 10^{-12}\,\frac{F}{m}$) (**Equation 3.2)**.

$$\varepsilon_r(\omega) = \frac{\varepsilon_s(\omega)}{\varepsilon_0} \tag{3.2}$$

The relative permittivity values presented in the results section are calculated based off capacitance measurements taken with an Ametek Parstat 4000 potentiostat. A specialized liquid measurement cell is used to take the capacitance measurements at frequencies ranging from 1 Hz to 100 kHz. Prior to the start of taking any ink or solvent measurements, an airgap measurement was taken in the liquid cell. This measurement is used to normalize the subsequent solvent and printing solution measurements by providing the permittivity value of air to determine the relative permittivity values presented in the results. The form of EHD printer used in this study applies an AC voltage between 1-1000 Hz across the printing formulation. Most relative permittivity values reported in literature make use of a high frequency model, which assumes a frequency much higher than 1000 Hz. [51] In order to report values most meaningful to both this research and other studies, several types of capacitance measurements were taken of each solvent and complete printing solution to determine the range of expected ε_r values for each material. Continuous sweep

measurements from 1 Hz to 100 kHz are taken to show the incremental change in the capacitance, and thus the relative permittivity, across a wide range of frequencies. Measurements were also taken at a constant frequency (400 Hz, 900 Hz, 1 kHz, 10 kHz, and 100 kHz) with 50 consecutive measurements taken. To minimize data collection errors, the capacitor plate gap was uniform across all measurements (2.300 mm).

3.5 Titania Printing Formulation Material Characterization Results and Discussion

Image analysis of the printed samples shows that the 1,4-butylene glycol-based printing solution has the smallest printed feature, as measured by the area in contact with the substrate, while under uniform printing parameters. The average feature diameter of the 1,4-butylene glycol ink under the stated printed conditions is 4.27 μm. The ethylene glycol printing solution resulted in the second smallest features with an average diameter of 9.61 μm, and propylene glycol, 1-buntanol, and 5-methylfurfural resulting in features with average diameters of 17.15 μm, 18.81 μm, and 24.48 μm, respectively. The average feature diameter along with other printing formulation material property data is presented in

Table 3.1 and detailed findings comparing the final printed feature size of each ink to an individual material property are presented in the follow plots. Since these are high circularity features, the feature size is equated to the feature diameter.

Table 3.1. Material properties of primary solvent in TiO_2 precursor ink and the complete inks. All values but the boiling point were measured as part of the research.

Primary Solvent	Boiling Point of Main Solvent (°C)	Relative Permittivity of Main Solvent	Surface Tension of Ink at Room T (~20°C) (mN/m)	Contact Angle on FOTS Si (º)	Viscosity of Ink at 25°C (mPa*s)	Viscosity of Ink at 95°C (mPa*s)	Average Feature Width (µm) Drop Mode Bias=150V
Ethanol	78.4	25.3	No Data	53.44	4.0	No Data	No Data
1-Butanol	117.4	1259	22.22	55.6	6.9	3.0	18.81
Ethylene Glycol	197.0	181.3	28.55	69.17	33.5	4.2	9.61
Propylene Glycol	187.6	13.81	29.22	65.1	97.1	4.5	17.15
5-Methylfurfural	187.0	3144	27.94	70.09	9.1	0.9	24.48
1,4-Butylene glycol	228	6.97	35.3	70.89	101.5	7.9	4.27

As the data show, the 1,4-butylene glycol ink resulted in the highest resolution printed features under the standard printing conditions. The collected data also show that there are a range of material properties that impact the size of the final printed feature. The material property versus feature size data is fit with a linear curve for all properties measured except for the Ohnesorge number. A range of curves were investigated for all data sets and the best curve was chosen based on the resulting R^2 values. The viscosity at 95 °C and the Ohnesorge number have the strongest correlation based on the R^2 squared values from the curve fitting. The relative permittivity and surface tension of the printed ink also showed a reasonable correlation and the contact angle of the printing solution on the FOTS coated Si showed some correlation to the final printed feature, but it was the weakest correlation based on the data collected.

3.5.1 *Viscosity*

Figure 3.5 (a) shows a plot that compares the printed feature diameter against the viscosity of the final printing formulations measured at 25 °C. The viscosity measurements of the printing solutions taken at this temperature show a modest correlation between increasing viscosity and decreasing feature size. This trend is strengthened by the data of the viscosity measured at 95 °C, shown in Figure 3.5 (b), which shows a strong trend that as the printing solution viscosity increases the final printed feature size decreases.

The strengthened correlation in viscosity to feature size as the measurement temperature increases was an unexpected finding. At 25 °C, there is a trend that indicates that as viscosity increases the printed feature size decreases. At 95 °C, this trend is much more obvious and the resulting R^2 value is 0.8542. This result could indicate that there is a localized increase in temperature, at or near the nozzle tip. As such, the viscosity of the printed material is elevated at the time of printing. This increase in temperature could be the result of the applied electric field that is necessary for standard EHD printing. This hypothesis is supported by research into the impact of an applied electric field on liquid dielectrics which shows that at high fields, the energy absorption of the liquid dielectric results in an increase in temperature. [52] Under the current EHD printer setup, measuring the temperate of the printing liquid at the nozzle tip is a non-trivial task. The volume near the point of eject is quite small and the space around the printer is limited. There are thermal imagers that could provide insight into general changes in temperature near the nozzle tip and it could be worthwhile endeavor to adjust the instrument setup to accommodate an external thermal imager. It would also be feasible to design an out-of-printer liquid cell to measure the impact of the electrical current on the printing liquid, with respect to temperature. A study of this

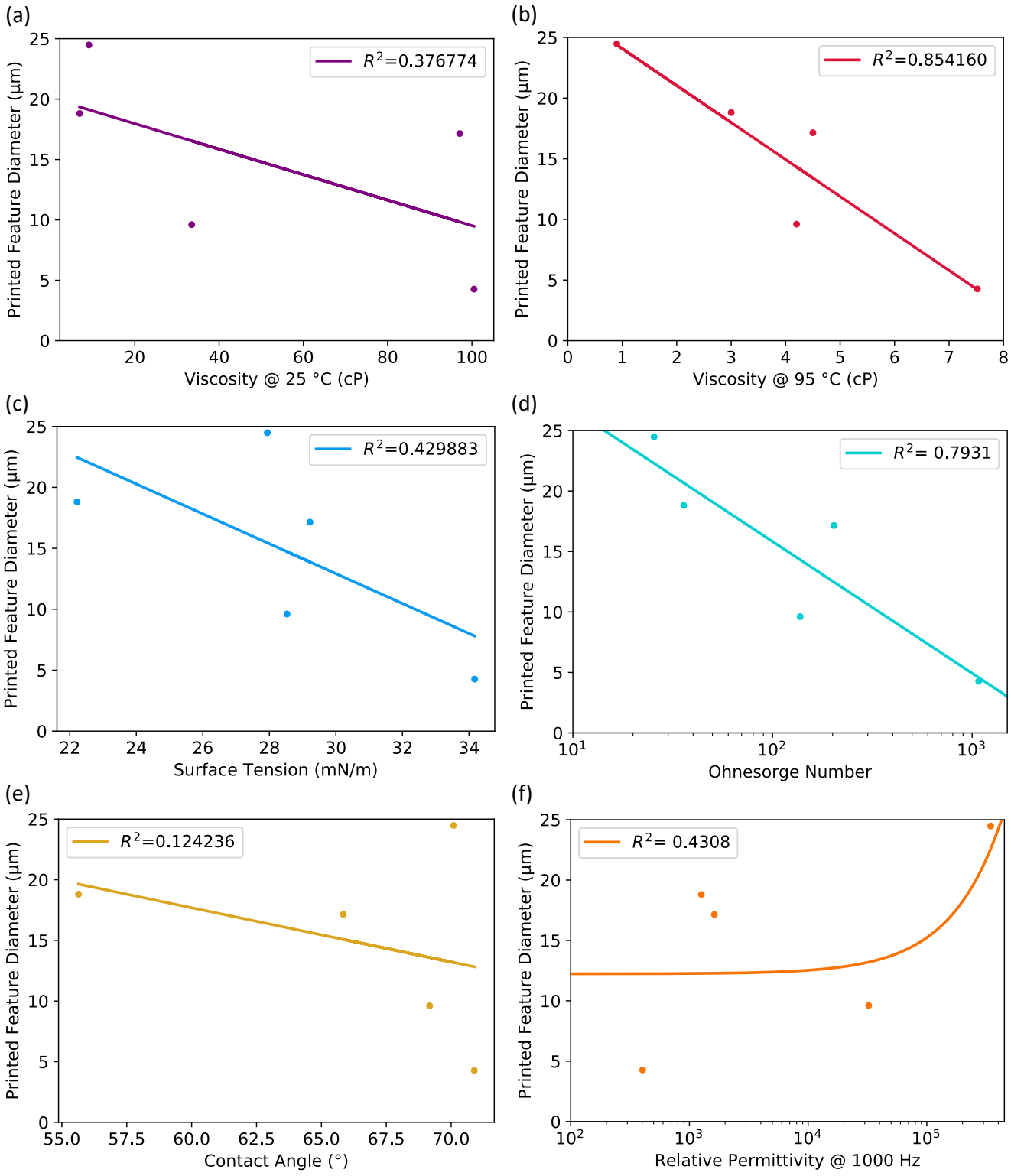

Figure 3.5. The data and trendlines of the printed feature diameter of each printing solution compared against (a) viscosity at 25 °C (b) viscosity at 95 °C (c) surface tension (d) Ohnesorge number (e) ink-substrate contact angle and (f) relative permittivity.

nature could be very valuable to the field of EHD printing by providing greater insight into the variations of the printing environment which would lead to more thoroughly optimized printing formulations.

It is also possible that the post-printing solvent evaporation step and PVP cross-linking step, which involves heating the sample to 200-250 °C, first reduces the viscosity of the printed features causing some material spreading. These two processes could be working in combination, first with the electric field induced increase in temperature impacting how the solution is drawn out of the nozzle then the final printed feature changing shape as the material is heated but not yet at the temperature that results in solvent evaporation and PVP crosslinking. Regardless of the cause, considering the viscosity of a printing solution at a temperature above room temperature appears important for determining ink performance during printing. Taking elevated temperature viscosity measurements of possible printing solutions prior to in-depth printing trials could result in more efficient ink development.

3.5.2 *Surface Tension*

Figure 3.5 (c) compares the measured surface tension of each ink to the final printed feature size. The data shows a noticeable trend that an increase in surface tension of the main solvent leads to a decrease in the final printed feature.

Surface tension, equivalent to surface energy, acts on the plane tangent to the free surface of a material and is perpendicular to a free edge in that surface, acts to keep the printing solution inside or adhered to the nozzle.[22], [23], [25], [43] Previous studies into the impact of the printing solution surface tension in EHD printing have looked at the surface tension in terms of how it impacts the solution jetting from the nozzle. [22], [23] These studies show that if the surface tension is too low, the formation of satellite drops is more likely to occur. If surface tension is too high,

there will not be enough electrostatic force to achieve solution jetting. [43] However, these studies stop short at investigating how the surface tension of the printing solution impacts the geometry of the printed drop. As shown in the data from Figure 3.5 (c), as the surface tension of the printing solution increases, the x-y area of the printed feature decreases. Similar to the impact of the relative permittivity, increasing the material parameters that resist the forces of the electric field appear to reduce the volume of the ejected drop and the x-y area of the printed feature on the substrate. It is also possible that increasing the surface tension reduces the drop spreading that occurs upon impact with the substrate and increases the degree to which the drop reduces in surface area after the force of impact has subsided. Additional studies can accurately determine the degree to which each of these factors (drop volume, resisting impact forces, overcoming impact forces) contributes to the final printed geometry, but the correlation between surface tension and printing resolution is evident in the current study and this material property should be strongly considered in the development of future printing solutions.

3.5.3 *Ohnesorge Number*

The Ohnesorge number (Oh, **Equation 3.3**) is a commonly investigated value for assessing the viability of a liquid in traditional piezoelectric inkjet and EHD printing.

$$Oh = \frac{\mu}{\sqrt{\rho\sigma L}} = \frac{viscous\ forces}{inertial \cdot surface\ energy\ forces} \tag{3.3}$$

$$\mu = viscosity$$

$$\rho = density$$

$$\sigma = surface\ energy\ or\ surface\ tension$$

$$L = characteristic\ spatial\ dimension$$

It relates the viscous forces to surface tension or surface energy and inertial forces. Previous studies have investigated this dimensionless parameter to understand electrified jet break-up [25] and the liquid cone shape as it leaves the nozzle [27], however, little information exists on the impact of this value on the final EHD printed feature.

The room temperature viscosity measurements and surface tension measurements were used to calculate the Ohnesorge number, which in turn lead to the creation of Figure 3.5 (d). This figure shows the Ohnesorge number versus the final printed feature size of each ink. Calculating the Ohnesorge number also requires knowledge of the liquid's characteristic drop length. For the purposes of this research, the characteristic drop is assumed to be spherical and the length is assumed to be the ejected drop diameter. The ejected drop diameter is calculated by using measurements of the printed feature height and diameter to calculate the final feature volume. The volume calculation is used in tandem with known material densities and thermogravimetric

analysis (TGA) measurements of each printing solution to understand the mass percentage remaining after the solvent evaporation step of the post-printing process.

The data show there is a good correlation between the calculated Ohnesorge number and printed feature size such that an increasing Ohnesorge number results in a smaller printed feature. This trend could be strengthened if the 95 °C viscosity values were used but the surface tension of the printing solutions can only be taken at room temperature (~25 °C). As such, the 25 °C values are used to maintain continuity of the measurement temperature.

Figure 3.5 (d) indicates there is a reasonable correlation that as the Ohnesorge number increases the characteristic printed drop size printed feature size decreases in a logarithmic relationship. Based on the information in Equation 3, it is clear that if the characteristic drop length is kept constant, a large Oh indicates that the viscous forces dominate and a small Oh indicates that surface energy forces dominate. Comparing this information to the data in Figure 3.5 (d) supports the previous claim that the viscous properties of a printing formulation have a more significant impact on the final printed feature than the surface energy. However, in this study, the characteristic spatial dimensions of the ejected drop varies so the change in Oh cannot be exclusively attributed to either the viscous forces or the surface energy forces but it is clear that increasing the Ohnesorge number by tuning the relevant material properties is an avenue to reducing the final printed feature.

It is important to note that this assessment runs contrary to work conducted by previous researchers indicating that high viscosity printing solutions are suboptimal for EHD printing based on the observed liquid cones. [27] The studies indicating that high viscosity and high Ohnesorge number materials are suboptimal look only at the liquid jet formation and not on the final printed feature. Low Ohnesorge number liquids have a reduced resistance to flow upon impact with a substrate and the liquid deformation upon impact with the substrate may be a more significant factor to consider when assessing materials for the final print quality. Furthermore, while the best methods available were used for determining the volume of the liquid feature remaining on the substrate prior to solvent evaporation and calcination. However, there are a significant number of assumptions made as a part of this calculation and several remaining unknowns.

One critical unknown is the shape of the ejected fluid. A significant gap in the current research is the ability to image the highest resolution nozzles and ejected drops, as well as the moment of incidence on the substrate, while printing is occurring. This is experimentally challenging due to the rapidly evolving relevant dimensions involved that are approaching the diffraction limit of light in often low optical density materials. Until this is addressed, there will continue to be questions about the true ejected drop volume, mode, and shape of high resolution EHD printed materials.

For the Ohnesorge number calculations presented in this study, a spherical ejected drop is assumed. However, due to the complexities and limitations associated with imaging mentioned above, the actual drop shape is unknown. Stretching of the ejected liquid could be present, the degree to which is impacted by the charge of the liquid and the rheological properties of the printing formulation. [53] This in turn impacts the characteristic length used in the Ohnesorge

number calculation. Another critical unknown is whether or not the printing liquid is forming discrete drops in air prior to reaching the substrate. Research by other groups has shown continuous liquid spindles connected the nozzle to the substrate. Under the conditions in the outside studies, discrete drops do not form in air and the liquid-substrate contact is broken upon removal, reduction, or reversal of the applied electric field. [28], [54] The same type of liquid deformation could be occurring to the printing formulations presented in this research, but as there is no measured data indicating the shape of the ejected fluid, the simplified, spherical drop model is used for this study. Further research into the liquid shape, either experimental or theoretical, of the family of inks presented in this dissertation would substantially benefit field of EHD printing.

3.5.4 *Contact Angle*

Figure 3.5 (e) shows a plot comparing the contact angle between the titania alkoxide formulations and the Si substrate coated with FOTS, against the printed feature diameter. There is a slight trend indicating that as the contact angle increases the printed feature size decreases, but it is notably weaker than trends observed in the viscosity, surface tension, Ohnesorge number and the relative permittivity.

The contact angle between the printed solution and the substrate is generally important for reducing the lateral dimensions of a printed feature on a substrate, as shown by the impact of adding the FOTS self-assembling monolayer to a clean silicon substrate. [55] But it appears that beyond a critical change of going from total wetting to a high contact angle, there is only a moderate correlation between the printed feature and the liquid-substrate contact angle (Figure 3.5(e)). It is likely that the electrostatic, viscous, and surface tension forces dominate the drop formation and the drop shape, pre and post impact, such that the ink specific solution-substrate contact angle does not substantially contribute to the printed drop geometry. If all other material

and printing properties are set, increasing the contact angle could be a method used to achieve small reductions in the overall x-y printing area but should not be main the parameter to adjust when working to further improve the printing resolution.

3.5.5 *Relative Permittivity*

Figure 3.5 (f) presents the calculated relative permittivity (see section 3.4.3) of the printing formulations, measured at 1 kHz, against the average printed feature size. The log scale on the x-axis is used to improve the data visualization as the range of calculated relative permittivity varies by orders of magnitude. The depicted trendline is a linear fit, the closest fit based on R^2 values. This comparison indicates that as the relative permittivity increases, the printed feature size increases, under standard printing conditions. The existence of a correlation between the relative permittivity and the final printed feature size was expected but the manner of that correlation was unexpected.

Prior to conducting this research, the hypothesis was that as the relative permittivity increases the ejected drop volume, and thus the printed feature size, decreases. Electrical permittivity is an indication of how significantly a material responds to the presence of an electric field. Given this, it was assumed that a material that responded more readily to an applied electric field would require lower DC and AC voltages to form an extruded liquid cone, resulting in a smaller liquid cone and thus smaller ejected drops and features.[22] However, the materials in this research showed an inverse response compared to the study by Lee et al., such that a larger relative permittivity resulted in a larger printed feature. It appears from the data presented in this section that materials that are more responsive to the presence of an electric field, result in a larger liquid cone being drawn out of the nozzle. This larger cone then results in larger drops occurring during the electrified jet breakup process leading to larger printed features.[22] The trend between the

relative permittivity and the final printed feature size isn't the strongest trend out of the properties investigated, but a correlation does appear, and it would be worth investigate this property and the correlation further.

It is important to note that the capacitance measurements used to determine the relative permittivity presented in Figure 3.5 (f), were taken at 1 kHz. The capacitance measurements resulting in the average relative permittivity values used in Figure 3.5 (f) are based of many repeated measurements. While there are oscillations in the collected data, the inconsistencies with respect to the literature values are not due to singular outlier points resulting in skewed data. This is a relatively low frequency to use for relative permittivity calculations, but this frequency was determined to be an appropriate choice due to the frequency constraints of the EHD printer. The AC electrical component of the EHD printer has a maximum frequency of 1 kHz. Given that the printing formulation response is influenced by the frequency of the AC component, comparing the relative permittivity of each formulation at a frequency within the bounds of the printing constraints would provide insight to the behavior of each formulation during printing.

To highlight how the relative permittivity changes as a function of the measurement frequency, a sweep of capacitance measurements from 1 Hz to 100,000 Hz was taken for each printing formulation. These measurements were used to calculate the relative permittivity of this range of frequencies and this data is presented in **Figure 3.6** (a). As seen in the figure, at lower frequencies the relative permittivity the printing formulations is several orders of magnitude higher than the relative permittivity at higher frequencies. In the example of the 1,4-butylene glycol ink the relative permittivity is on the order of 10^6 when measured at 1 Hz and goes down to about 75 when measured at 100 kHz.

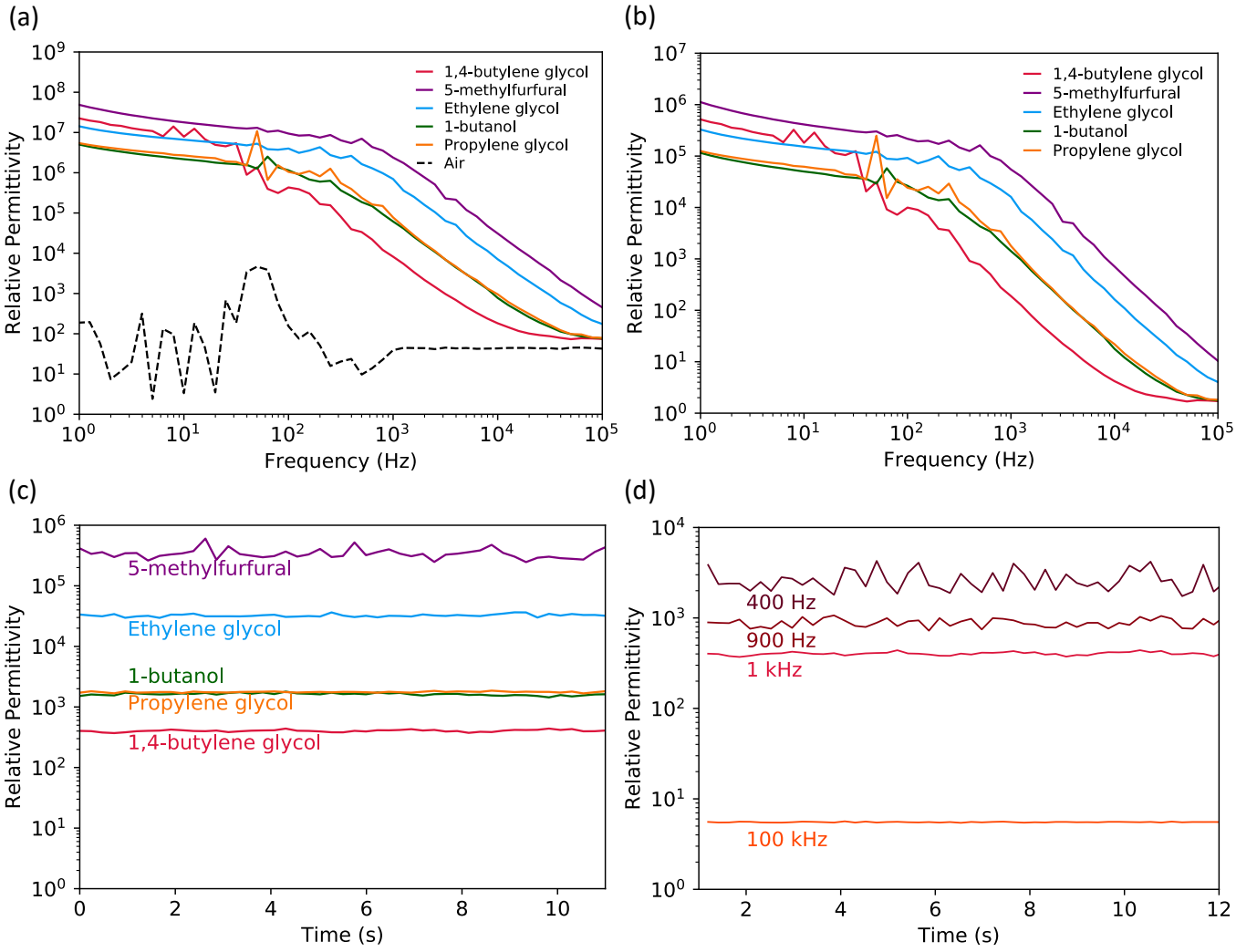

Figure 3.6. (a) Relative permittivity of printing formulations and liquid cell airgap from 1 Hz to 100,000 Hz. (b) Relative permittivity of printing formulations from 1 Hz to 100,000 Hz normalized with respect to the liquid cell air gap at 100,000 Hz. (c) Relative permittivity of all printing formulations at 1000 Hz. (d) Relative Permittivity of 1,4-butylene glycol at discrete frequencies.

The response of air to the changing frequency of the capacitance measurement is presented in Figure 3.6 (a) as well. The pattern for the changing permittivity of air is notably different than the printing formulations. It is also notable that steady state value reached by air is about 1.5 orders of magnitude higher than the standard relative permittivity of air, 43.5 and 1.0006 respectively. In

order to account for this difference, the calculated relative permittivity of the printing formulations is normalized to the calculated relative permittivity of air. The normalized version of the data in Figure 3.6 (a) is presented in Figure 3.6 (b). Normalizing the data in this manner, results in the high frequency (100 kHz) relative permittivity values adhering much more closely to expected values based on known values of the relative permittivity of the primary solvents.

Another notable observation from this phase of research is the oscillating nature of the relative permittivity, even during measurements at constant frequency. The oscillating relative permittivity phenomenon is present in Figure 3.6 (c) and (d). Figure 3.6 (c) shows the calculated relative permittivity of each printing formulation, using capacitance measurements at 1 kHz. Fifty consecutive measurements were taken of each material. This figure also shows the wide range of the relative permittivity across the different printing formulations. The 1,4-butylene glycol ink has the lowest relative permittivity at 1 kHz and this also the printing formulation that results in the smallest printed features. To better understand the variations in the 1,4-butylene glycol ink, especially withing the frequency regime of the EHD printing methods, continuous capacitance measurements were taken at several discrete frequencies: 400 Hz, 900 Hz, 1 kHz, and 100 kHz. Figure 3.6 (d) shows the 50 consecutive capacitance measurements taken at each frequency to investigate the variability of the relative permittivity. These frequencies were chosen due to their relevance to EHD printing (400 Hz, 900 Hz, 1 kHz) and to get a sense of the relative permittivity at high frequencies (100 kHz). Similar to the sweep measurement, this figure shows that at lower frequency the calculated relative permittivity is higher than at higher frequencies. It is particularly interesting for the applications of EHD printing to note that there is more than order of magnitude difference in the relative permittivity of the 1,4-butylene glycol formulation within the bounds of the AC frequency of the EHD printer. This variation highlights that the AC frequency must be

considered as important to the printed material output both in terms of the physical response and electrical response of the printed liquid. Going forward, when determining the optimal printing parameters for a specific material or application, it is clear that material's response to the AC frequency should be studied.

The relative permittivity of an EHD printing formulation is an interesting, insightful, and complex material property to measure. In addition the relative permittivity to printed feature shape trend showing a relationship opposite to the original hypothesis, the significant variation in the relative permittivity of one material was another unexpected outcome. Furthermore, there is a significant gap in EHD printing research in the space of measuring the relative permittivity of printing formulations and studying the impact of this value on the final printed feature. For the purposes of this study, to achieve the smallest possible printed feature, a low relative permittivity material most likely to achieve those results. Within the bounds of that material, using a higher frequency should result in the material exhibiting a lower relative permittivity. There is still a significant amount to research to be conducted in this space, even within the narrow focus of titanium alkoxide based inks, and the preliminary data presented in this section is hopefully just a first step towards this sub-section of EHD printing materials analysis receiving a greater amount of research focus in the future.

3.5.6 *Effective Printing Window and FTIR*

Effective printing time window is the final material quality considered in this study. This parameter is defined as the amount of time the material flows through the nozzle without resulting in clogging. The reason for clogging can change from ink to ink. In this study the two reasons that stand out are clogging due to solvent evaporation at the nozzle tip and ink gelation resulting in a material that can no longer be drawn from the nozzle. Nozzle clogging is common in EHD printing,

especially when using nozzles with inner diameters of a few microns or smaller. For this research, an ink will ideally have an effective printing window of at least three hours. This is sufficient time to set the printing parameters, run the initial test prints, run the controlled prints, and do a range of new printing experiments. The ethanol-based inks first developed for this project have a use time of approximately 30 minutes or less. This is not sufficient time to complete the controlled prints and as such the feature size versus material parameter tests were unable to be completed. 1-butanol based inks have a printing window of about 1 hour. This is sufficient time to run the control printing tests, but it is not sufficient to allow for significant printing experimentation beyond that. Propylene glycol and 5-methylfurfural have a similar effective printing window of 1.5-2 hours. This is sufficient time to run the control prints and a few experimental printing runs but not ideal for expansive printing tests or for scaling up the printing process to a manufacturable level. The clogging observed in these four inks appears to be the result of solvent evaporating at the nozzle tip, causing the dissolved PVP to resolidify thus preventing solution from exiting the nozzle. This clogging is visible on the printer's nozzle camera. During this same period, the bulk solution in a sealed scintillation vial appears unchanged.

The ethylene glycol ink has a printing use time of 2.5-3 hours. This is sufficient time to run the control prints and complete many experimental printing runs. Nozzle clogging does eventually occur making the ethylene glycol ink suboptimal for scaled processes. An interesting distinction to note with the ethylene glycol ink is that the nozzle clogging for this printing solution does not appear to be the result of solvent evaporation and PVP resolidification at the nozzle tip. The boiling point for ethylene glycol is 197 °C, about 10 degrees higher than propylene glycol and 5-methylfurfural, 80 degrees higher than 1-butanol, and over 100 degrees higher than ethanol. The nozzle clogging for ethylene glycol appears to be due to the slow conversion of the solution from

a liquid to a gel. This process is observed in the bulk solution as well. At the time of the nozzle clogging the bulk printing solution has gone from fully transparent to slightly turbid. Over an additional 24-48 hours after printing the ethylene glycol printing solution has transformed into a pseudosolid gel. The visual transformation of the ethylene glycol ink is shown in **Figure 3.7** (a) alongside two other printing formulations (ethanol and 1-butanol) that remain unchanged over this same period. Although not all formulations are depicted here, no other printing solution developed for this research transformed in the same manner as the ethylene glycol formulation. It can be seen from the molecular structures shown in Figure 3.7 (b) that ethylene glycol has the highest hydroxyl group to molecular weight ratio out of the solvents considered. It is likely that the greater number of hydroxyl groups in the ethylene glycol solution compared to all other printing solutions causes the formation of hydrogen bonds between these hydroxyl groups and the TDBA, resulting in a polymeric gel network.[46], [56]

Fourier-transform infrared spectroscopy (FTIR) was conducted to assess changes observed in the ethylene glycol printing formulation that were not observed in any other printing formulation. The measurements were taken on a Thermo Nicolet iS10 FT-IR of the 1,4-butylene glycol and ethylene glycol inks at three different time intervals: t = 0 hr, t = 24 hr, and t = 3 weeks. This time scale was chosen to provide a baseline at t = 0 hr, a first measurement after the ethylene glycol appears to be fully gelated (t = 24 hr), and substantially longer (t = 3 weeks) in an effort to create the create the conditions for a stronger measurable difference. Over this period of time, the 1,4-butylene glycol and all other printing formulations appear unchanged.

FTIR measurements taken to investigate hydrogen bonding hypothesis (Figure 3.7 (b) and (c)) show characteristic peak broadening between 3300 and 3400 cm^{-1} of the ethylene glycol printing solution indicating that extended hydrogen bonding is present.[56], [57] Initial FTIR

measurements are taken immediately after printing solution preparation is complete and the peak broadening is observed when a sample is measured 3 weeks after its formulation. In contrast, the 1,4-butylene glycol ink prepared and measured simultaneously to the ethylene glycol ink does not show any change in the FTIR measurements over this same period.

The 1,4-butylene glycol has an effective printing window of at least five hours and likely much longer. No solvent evaporation driven clogging or solution gelation has been observed during any printing trials. 1,4-butylene glycol has the highest boiling point of all the solvents tested for this research (228 °C). It has the same number of hydroxyl groups per molecule (2) as ethylene glycol but twice the number of carbons. Therefore, the overall number of hydroxyl groups per volume of solution used is significantly lower. This change could be what is driving the increased stability of the printing solution. Thus far, the conclusion of printing has been due to the completion of all necessary control prints and desired experimental prints and not the result of nozzle clogging. As such, the true maximum printing time of this ink has yet to be determined.

The benefits of highly a stable printing formulation include an extensive printing time which allows for meaningful experimentation and the possibility for a scaling up any process using the 1,4- butylene glycol formulation. In addition, this formulation opens up the possibility of working with even narrower inner diameter nozzles. The finest printing nozzles available for this tool have an inner diameter of 500 nm. A substantially narrower nozzle has a lower tolerance for clogging due to particle-like growing polymeric chains, as in the ethylene glycol ink, and the substantially lower volume of the nozzle tip results in solvent evaporation driven clogging occurring more rapidly. The 1,4-butylene glycol and titanium alkoxide printing formulation is a suitable material for the 500 nm printing nozzles due to minimal solvent evaporation and no observed polymerization or gelation based nozzle clogging.

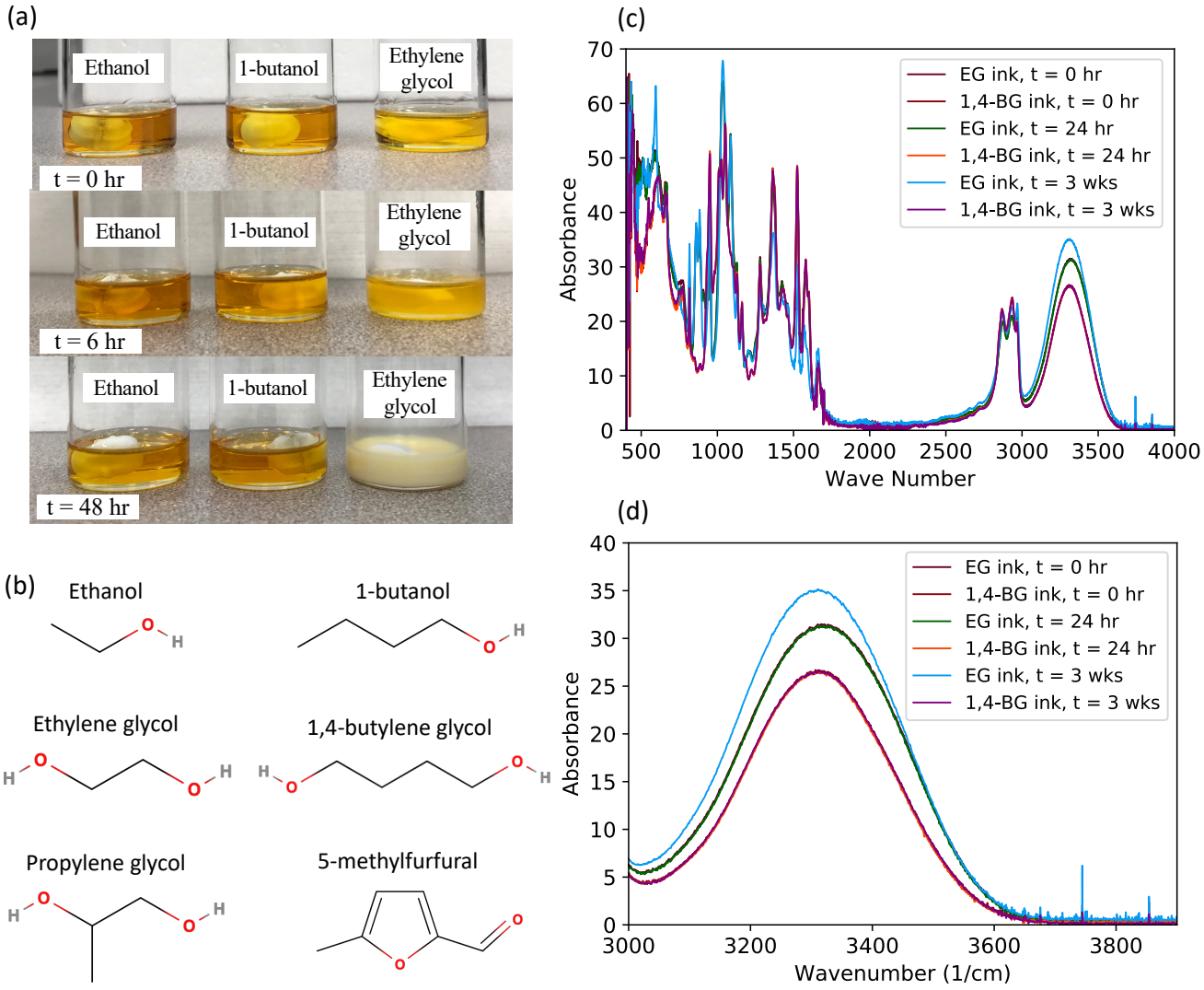

Figure 3.7.(a) Images of changes in ethylene glycol ink over time. (b) Molecular diagrams of solvents. FTIR of ethylene glycol and 1,4-butelene glycol printing formulations showing the full spectrum (c) and the region indicating hydrogen bonding (d).

3.6 Summary of Results and Conclusion

The 1,4-Butylene glycol printing solution has the highest viscosity, highest surface tension, highest boiling point, and lowest relative permittivity at critical frequencies. This combination of optimal material properties resulted in the highest resolution printed features, with an average diameter of 4.27 μm, under standard printing conditions using a 2 μm inner diameter nozzle. This is not highest resolution feature ever recorded for this ink, or other inks tested for this research, but the constraint of using constant printing parameters for all the solutions considered resulted in larger features for the best performing inks. Under variable conditions, using a 2 μm inner diameter nozzle, the 1,4-butylene glycol ink and the ethylene glycol inks can produce features below 1 μm. However, under these printing parameters, the other inks do not jet, making it impossible to conduct a meaningful comparison of the inks.

The high resolutions features achieved by the ethylene glycol and 1,4-butylene glycol inks indicate that EHD printing is a viable method for making mid and near-IR wavelength meta-optical device components and the extensive printing time shown with the 1,4-butylene glycol ink shows that this material is suitable for a scaled-up process that requires consistent printing during a long effective use time. In the following chapter, the highest resolution features are presented along with examples of the applications of these materials and methods to make functional meta-optical device components.

Chapter 4. APPLICATIONS OF ELECTROHYDRODYNAMIC INKJET PRINTING IN META-OPTICS, PHOTONICS AND PLASMONICS

To demonstrate the efficacy of electrohydrodynamic inkjet printing, a fully additive and direct-write process, for depositing high refractive index, functional optical materials, a functional meta-optical lens for a mid-infrared wavelength is printed. This device is based around the ability to print discrete 1 μm features over a large area. The materials and methods necessary to achieve this resolution over a large area is presented in the previous chapter.

The success of the meta-optical lens for mid-infrared light, and the improvements made to the materials and process thereafter, led to the design of an EHD printable plasmonic bullseye antenna for a near-infrared wavelength (1530 nm). This device is designed to be coupled with a near-infrared nanocrystal quantum dot emitter (QD), that is subsequently EHD printed with a different QD printing formulation. The proposed device structure is based around the ability to discretely print 500 nm features out of a high refractive index material and the ability to print low volumes of QDs with high precision. The research presented in this chapter aims to highlight the known, highest resolution capabilities of the titanium alkoxide based printing formulations and the applications of the materials and methods pertaining to printed meta-optics and plasmonic devices.

4.1 Fully EHD Printed Meta-Optical Lens

The meta-optics pattern for this application was designed around the principles of subwavelength diffractive optics. Under this mechanism, the desired phase shift in light occurs by exploiting variations in lateral size and orientation of the individual scatterers while maintaining a uniform thickness. [58] The scatterers must have a subwavelength quasiperiodic structure with

respect to the wavelength the metalens is designed to focus. The results are optical elements that are substantially thinner than a conventional diffractive lens, typically less than the wavelength of the focused beam. These principles have been used to fabricated metalenses with a large numerical aperture (NA > 0.99), indicating a very small spot size of the focused light and increased resolving capabilities. [59], [60] This has benefits in the ever-expanding internet of things, which relies on a large network of thin and inexpensive sensors, optical displays as well as other emerging technologies that require lightweight optical components. [58], [59] Previous work focused on EHD printed micro and nanolens arrays by Lianqing Liu et. al used UV-curable polymers as the printed materials. These materials have a lower refractive index and a higher absorption at $\lambda = 5\ \mu m$ than is optimal for maximum lensing efficiency. [24], [37], [59], [60], [61] Furthermore, these printing experiments examine the lensing capabilities of the individual printed feature based on conventional diffractive lens designs, not the subwavelength diffractive optics of a meta-optics lens demonstrated in this body of work. [24], [61]

4.1.1 *Device Fabrication*

The materials and process development research presented in Chapter 3 led to the fabrication of the first fully EHD printed mid-infrared meta-optics lens made from a functional TiO_2 alkoxide and polyvinyl pyrrolidone (PVP) hybrid ink. The printing solutions developed for the initial high-resolution EHD printing experiments were used to make a meta-optical lens designed to focus 5 μm light. The initial success of the ethylene glycol based ink, measured by the ability to print 1 μm features, led to experimenting with the capabilities of printing a full meta-optical pattern with this formulation.

The meta-optical lens pattern is printed with the ink made from ethylene glycol, TDBA, PVP (~55,000 mw), IPA, and poly(melamine-co-formaldehyde) methylated in the same ratios and

using the same formulation methods described in Chapter 3. Just before printing, the final solution is filtered using a 0.45 μm, water-wetting polytetrafluoroethylene (PTFE) membrane syringe filter (VWR). The $1\ mm \times 1\ mm$ meta-optical lenses are fabricated on an n-type silicon wafer coated with FOTS, under ambient conditions, using the same EHD printer as described in the Chapter 2.

After printing is complete, the substrate was placed on a 200 °C hotplate for 20 minutes. This is to enable the thermal crosslinking of the PVP and poly(melamine-co-formaldehyde) methylated, to evaporate the printing solvents, and convert the titania precursor to amorphous TiO_2. Selected samples were exposed to an additional sintering step to convert the amorphous TiO_2 into anatase and burn off the residual PVP. During this step, the samples were heated in a box furnace to 450 °C and held at that temperature for one hour. After thermal conversion of the ink, the samples were assessed for printing quality using an optical profilometer (Olympus OLS4100), SEM (FEI Sirion XL30 and FEI Apreo VP) and AFM (Oxford Instruments, Jupiter XR). Determination of the printed feature size was done using both the image analysis software in the AFM and with the image analysis software, Fiji. Material and phase analysis was conducted with XRD (Bruker D8 Advanced XRD). Figure 1 (h) shows the X-ray diffraction (XRD) spectra of the TiO_2 printing solution before and after the high temperature annealing process. The diffraction peaks characteristic of the anatase phase of TiO_2 were detected in the samples after the high temperature process, confirming the formation of crystalline TiO_2. XRD spectra from samples that did not undergo the annealing process were characteristic of an amorphous material.

The meta-optics lens made for this study was printed using the dropwise mode, described in Chapter 2. As we demonstrate here, a digital dropwise EHD method can provide the degree of material deposition control necessary to print meta-optics patterns with any level of periodicity where the deposited droplet location depends primarily on the translational stage movement. The

printed feature size can be volumetrically varied on a drop-to-drop basis for single drop features by changing the printing parameters such as DC voltage, AC voltage, and AC frequency.

Mid-infrared meta-optical lenses were printed in four sequential patterns, coinciding with the four different diameters (1 μm – 4 μm) of the meta-atoms present in the optimal infrared lensing design. **Figure 4.1** (a-d) show the distinct patterns made of each size of printed feature. The printer

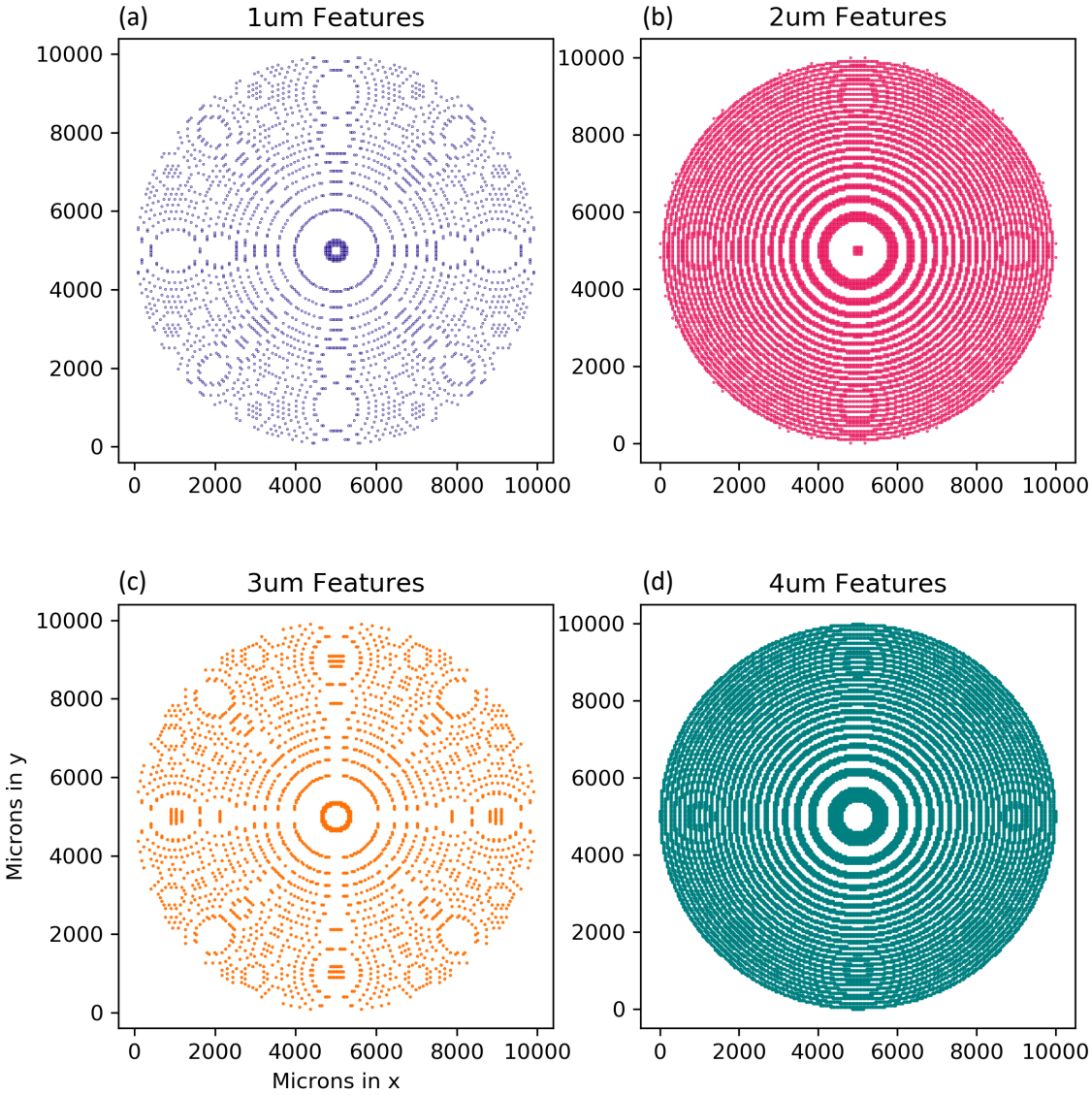

Figure 4.1. The meta-optical lens displayed in the four discrete feature patterns. (a) 1 μm (b) 2 μm (c) 3 μm and (d) 4 μm features.

nozzle was kept at uniform height (approximately 10 μm) throughout the printing process. The alternating current was applied in a 75% square waveform, which was uniform across the entire print. Each printed pattern was made with a different applied bias and wave amplitude, to modulate the printed feature size following the pattern of the designed meta-optics lens. The individual features of each pattern were printed in a single printing pass under one set of parameters; larger features were not achieved by printing in the same location with multiple drops. This is achieved by increasing the applied DC voltage between the nozzle and the stage to increase the volume of the ejected drop. If all other parameters remain constant, a larger applied voltage results in a larger ejected drop and thus larger printed feature.

4.1.2 *Fabrication Results*

The materials and process developed for this research resulted in the highest resolution EHD printed TiO_2 reported in literature. [55] Using a 2 μm inner diameter nozzle with the ethylene glycol based printing formulation, consistently printing features on the order of 1 μm is possible. **Figure 4.2** (a) shows an optical profilometry image and Figure 4.2 (b) shows an SEM image of EHD printed TiO_2 with an average feature diameter of 1.2 μm with the range of the printed features from 0.9 μm to 1.4 μm. The average height of the printed features in this array is 297 nm, as measured by AFM. This sample was printed using the continuous print mode with a printer bed speed of 2.0 mm/s. Figure 4.2 (d) shows an optical profilometry image and Figure 4.2 (e) shows an SEM image of EHD printed TiO_2 printed using the dropwise print mode. This is an example of the range of features necessary to fabricate a meta-optics lens designed to focus 5 μm light. The different feature sizes present in this example are intentional and were printed using different applied bias and wave frequency. The range of features in this example lie between 1.2 μm and 6.0 μm, as measured at the base of the printed feature. The designed range of sizes for the features

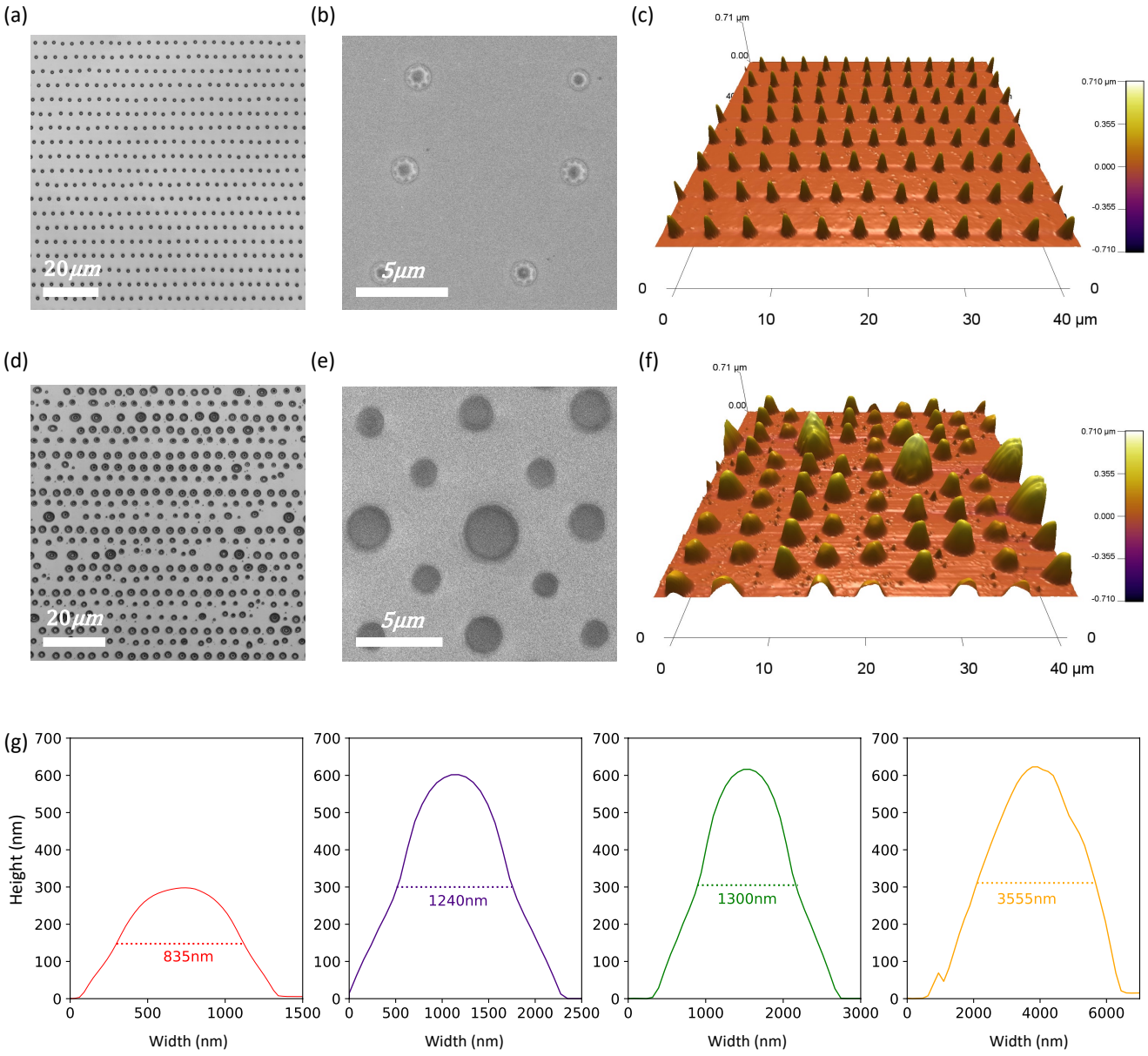

Figure 4.2. (a) Optical profilometry image of TiO_2 precursor ink printed in continuous EHD mode, the scale bar is 20 μm (b) SEM image of TiO_2 precursor ink printed in continuous EHD mode, the scale bar is 5 μm (c) AFM height scan image of samples shown in (a) (d) Optical profilometry image of TiO_2 precursor ink printed in dropwise mode using different printing parameters for different sized features, the scale bar is 20 μm (e) SEM image of TiO_2 precursor ink printed in dropwise mode, the scale bar is 5 μm (f) AFM height scan image of samples shown in (d) (g) Cross sections of printed features with four different sizes fabricated using different EHD printing conditions showing the full width at half maximum height of the features.

was 1.0 μm to 4.0 μm. Figure 4.2 (c) and (f) shows AFM height images of the samples from Figure 4.2 (a) and (d), respectively. Figure 4.2 (g) shows four AFM cross-sections of features with different base diameters (1.2 μm, 2.2 μm, 3.1 μm, and 6.0μm). The maximum height of each printed feature is 297 nm, 597 nm, 616 nm, 622 nm respectively. The full width at half maximum of these printed features is 835 nm, 1.24 μm, 1.30 μm, and 3.6 μm, respectively.

Once the materials, substrate surface energy and EHD printing processes were developed to provide droplet volume control and a lateral resolution of 1 μm for functional TiO_2, these techniques were applied to create a fully printed $1\ mm \times 1\ mm$ mid-infrared meta-optics lens, based on discrete scattering features, designed to focus 5μm light. The designed 2D metasurface is made of regions of features ranging from 1 μm – 4 μm in diameter with a 5 μm pitch between each feature, regardless of the feature diameter (Figure 4.1 (a-d)). The printed version of the meta-optics resulted in features ranging from 1.2 μm - 6.0 μm.

Figure 4.3 (a) shows the as designed, complete metasurface lens, with each feature pattern overlayed on the other and each color in the pattern representing a different scattering feature diameter. Figure 4.3 (b) shows a final, fully EHD printed meta-optics lens, indicating that there is a high fidelity between the designed pattern and the printed pattern. Close-up images are shown of the designed (Figure 4.3 (c) and (e)) and printed (Figure 4.3 (d) and (f)) meta-optical lens. Figure 4.3 (d) and (f) show that there are distinct diameter differences between the features printed at each set of printing parameters, with the larger features resulting from the higher voltage and larger wave amplitude. The 1 μm and 2 μm feature regions have consistently discrete features. The 3 μm and 4 μm feature regions have some discrete features but also show a significant number of merged structures. This defect appears to occur more frequently in regions of the substrate where there is

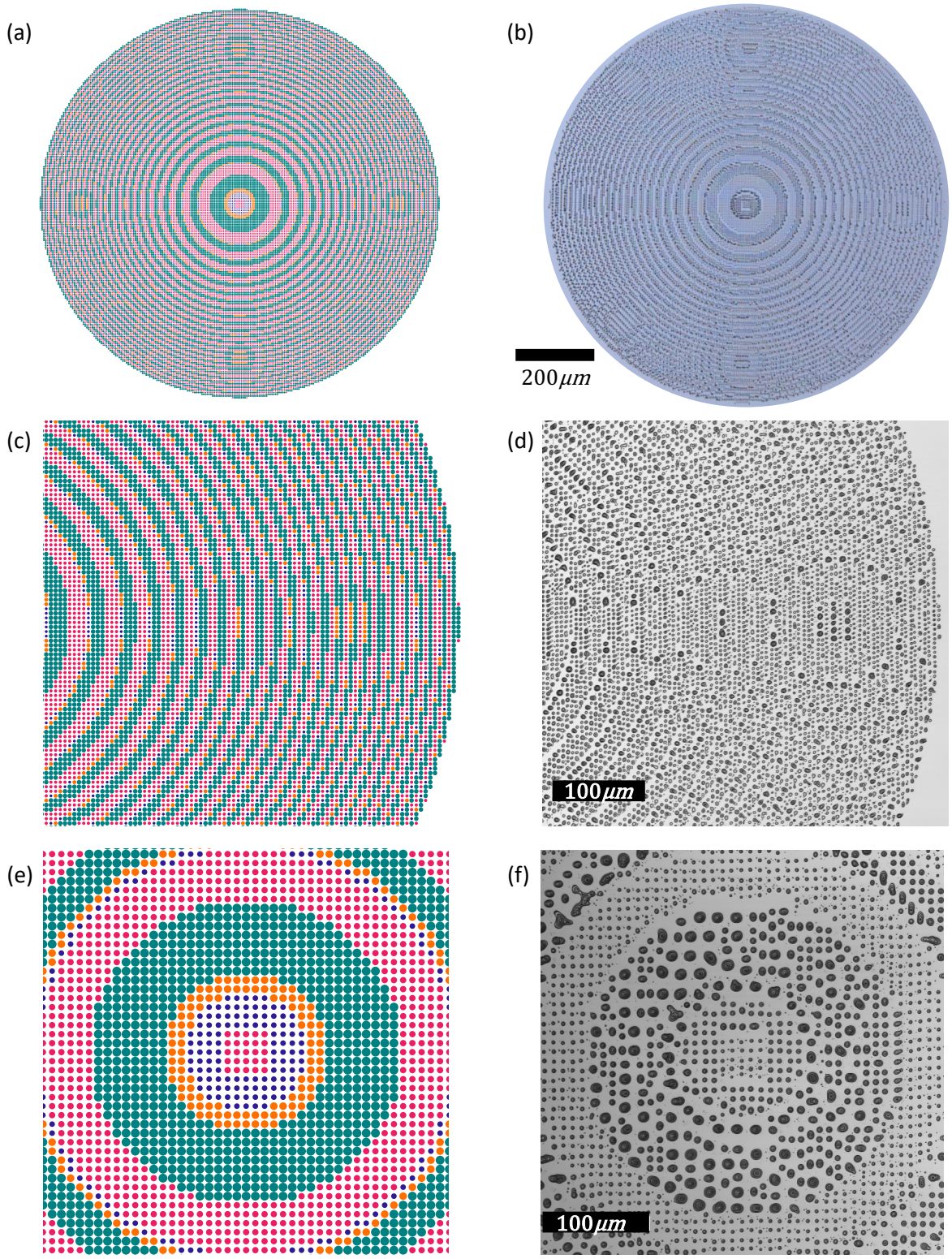

Figure 4.3. (a) Designed mid-infrared meta-optical lens (b) Full view, optical profilometer image of fully printed mid-infrared meta-optics lens (c) central, right section of designed meta-optical lens (d) optical profilometry image of central, right section of printed meta-optics lens (e) close-up view of central region of meta-optical lens (f) close-up view of central region of the printed meta-optical lens.

a higher concentration of 3 μm or 4 μm diameter structures. There is variation amongst the printed features of all diameters but because the feature-to-feature pitch is set at 5 μm in the mid-infrared meta-optics lens, as the features get larger, the room for error without resulting in merged printing drops, decreases.

4.1.3 *Meta-Optical Lens Performance Results*

The phase-distribution $\Phi(x, y)$ of the metalens with a focal-length of f follows the hyperboloid phase profile:

$$\Phi(x, y) = \frac{2\pi}{\lambda}\left(\sqrt{x^2 + y^2 + f^2} - f\right) \quad (3)$$

The original meta-optical lens was designed around the constraints of the titania alkoxide printing materials and the EHD printer. For the printable photonics, the presumed highest achievable thickness of the scatter is $\sim 1\ \mu m$, which limits the phase-coverage. Even under the constraints of the printable features, the estimated phase coverage to is $\sim 0.6\,\pi$, which is sufficient to create a lens. [62] **Figure 4.4** (a) shows the amplitude and phase distribution of the designed meta-optics lens.

The printed meta-optics was characterized using a confocal microscopy set up in mid-IR. In this microscope configuration, a pulsed 5 μm quantum cascade laser (QCL) with 500 ns pulses and repetition rate of 100 kHz is coupled to an InF_3 single mode fiber (NA ~ 0.26 with 9 μm core) and collimated using a black diamond asphere (NA = 0.85) resulting in a collimated beam of about 1mm to match the metasurface clear aperture. The metasurface is translated relative to an imaging lens with a clear aperture of ~25 mm and f = 12.7 mm. The image is captured on and InSb focal plane array (FPA) with a 15 μm pixel pitch and 640 x 512 pixels cooled to 76 K. The camera

acquisition time is 0.9 ms to best fit the 14-bit dynamic range of the FPA and 100 frames are captured and averaged with background correction.

Focusing of the light is clearly observed as we scan along the optical axis (**Figure 4.4** (c) and (d)) and it is possible to fit the intensity at the focal plane to estimate the FWHM of the beam spot to be ~15 μm. The focusing behavior is sub-optimal due to low phase coverage but the focusing behavior is expected to improve as we expand our printing capabilities and print thicker materials.

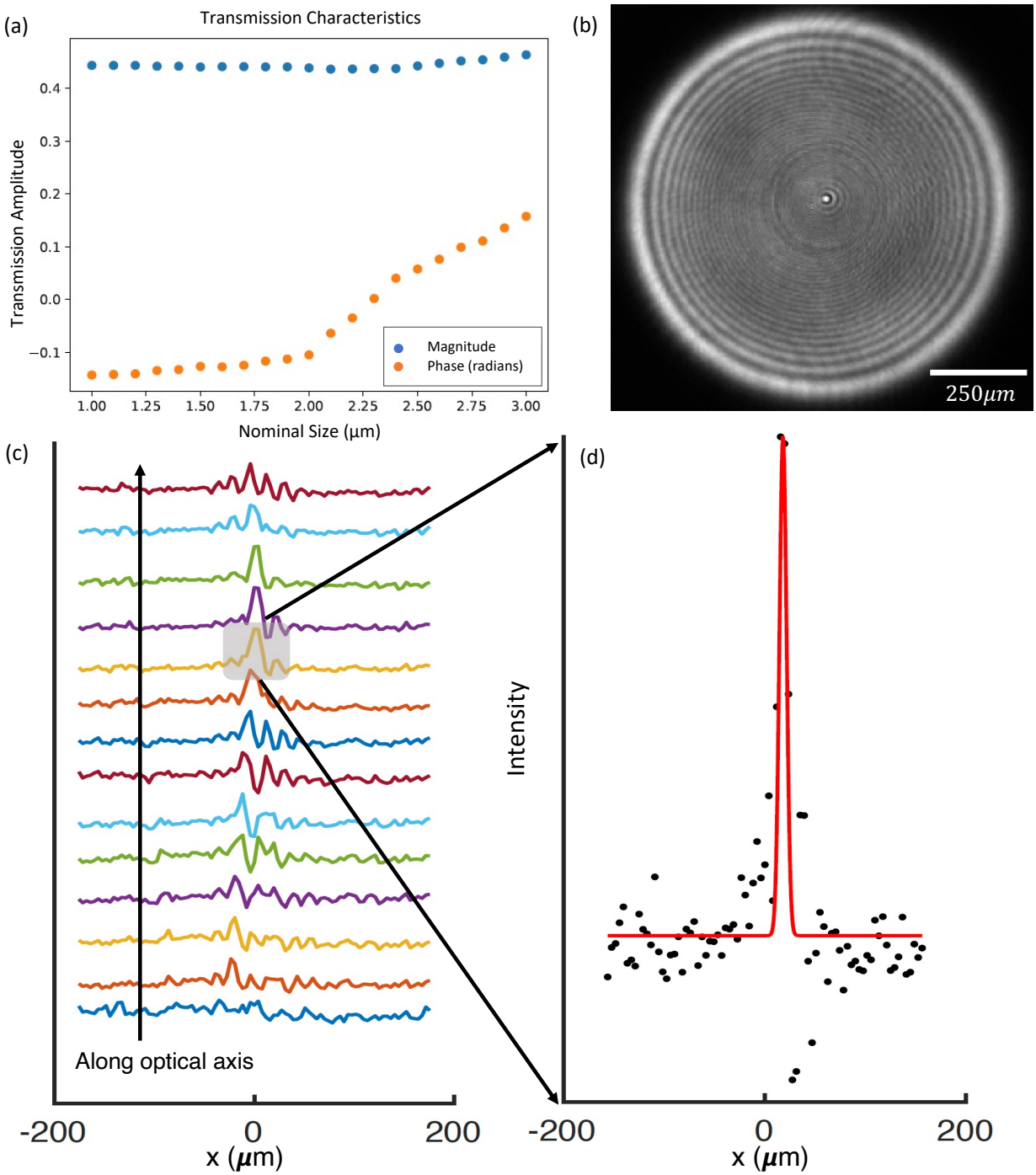

Figure 4.4 (a) The amplitude and phase of the scatterer as a function of the scatterer diameter for light propagating perpendicular to the plane of the metasurface which is typically parallel to the long axis of the scatter feature (b) Signal intensity image showing the most power in the focal spot at the center (c) Focusing measurements taken along the optical axis (d) Peak intensity focusing measurement showing FWHM of the beam spot is ~15 µm.

4.1.4 *Discussion*

There is a strong correlation between the size of the ejected printed drop and the voltage applied between the nozzle and the substrate stage. With all other printing parameters remaining constant, the inks developed for this research show an increase in drop volume as the applied DC voltage increases. This is demonstrated by an increase in the final observed printed feature size. For the metalens shown in Figure 4.3 (a) and (b), the features designed to be 1μm in diameter were printed with an applied DC voltage of 65 V and the 2 μm, 3 μm, and 4 μm diameter features were printed with an applied DC voltage of 77 V, 95 V, and 105 V, respectively. It is important to note that the trend of increasing voltage resulting in larger ejected ink drops is present across the many samples that were printed but it is not the case that one applied voltage will result in a specific drop size every time. For example, other metalenses were printed in a range of 88 V – 210 V for the 1 μm – 4 μm diameter features. This difference in absolute applied voltage is likely due to other variables in the printing set up, such as small variations in nozzle height.

Increasing and decreasing the nozzle height has been shown to impact the voltage required to initiate ink jetting. The further the nozzle is away from the substrate, the higher the applied voltage must be to create a large enough electric field initiate ink jetting. Zhou et al. demonstrated the correlation between nozzle height, applied voltage, and feature size in a 2020 study where micron and submicron features of a UV-curable polymers were printed using the EHD method. [24] The set-up used for the EHD printed metalenses allows for top down control of the nozzle distance away from the substrate with a movement resolution of 1 μm. However, this is not a dynamically controlled printing parameter and the nozzle height remains constant with respect to the top of nozzle arm on the z-axis of the printer (see Figure 2.1 (a)). Although these experiments were conducted in a climate-controlled laboratory with HEPA-filtered airflows, it is also possible that

small variations in temperature, ambient relative humidity, stage roughness, and substrate and ink handling could lead to variations in the electric fields required for a given printing outcome. Therefore, it can be reported that a positive correlation exists between the applied voltage and the resulting printed drop volume but a precise quantitative relationship is presently unknown.

TiO_2 precursor ink printing trials for the 5 μm meta-optical lens revealed that the printing mode can significantly impact the printed feature resolution and feature shape. The highest resolution individually printed drops were consistently generated using continuous print mode. Using the 2 μm inner diameter nozzle with the ethylene glycol formulation, discrete drops below 1 μm in diameter were consistently measured using the continuous print mode. The printed features also had a more consistently uniform radius when compared to the dropwise printing method. The observed improved resolution under the continuous print mode led to the design of the plasmonic bullseyes, discussed in Section 4.2, that are intended to focus light with a wavelength shorter than 5 μm, thus expanding the applications for this printing method and for printed photonics. However, continuous printing mode does not allow for the same drop-on-demand control as is available with dropwise printing. Fabricating the quasiperiodic pattern necessary for the mid-infrared meta-optical lens presented in this research is not currently feasible using the continuous print mode. Therefore, the continuous printing mode is only practical for simpler printing patterns.

The meta-optical lens from this study was printed using the dropwise EHD printing mode. Challenges for effective dropwise printing are the hysteretic effects associated with the need to repeatedly start and stop the flow of ink. To achieve initial ink jetting, a higher nozzle electrode to ground plane potential difference is required to initiate droplet formation. This potential can be reduced once a droplet stream is established to achieve the smallest possible drop volume. There is a correlation between applied voltage and drop size, with the higher voltage resulting in larger

ejected drops, thus increasing the size of the printed feature. [24] In dropwise mode, the EHD printer needs to overcome this activation barrier energy at each feature location, therefor increasing the minimum feature size that can be achieved in this mode with respect to the continuous print mode.

As discussed in Chapter 3, the hydrophobic SAM (trichloro(1H, 1H, 2H, 2H-perfluoroctyl)silane) used to coat the polished Si wafer is an essential process step to enable the high resolution features achieved in this study and previous studies. Total wetting between the ink and the substrate is observed when the TiO_2 precursor solution is deposited on a clean and uncoated Si wafer. The contact angle of the ethylene glycol and TDBA ink increases to 68° with the addition of the hydrophobic SAM. In terms of film thickness, this translates to an increase in the single drop height from 20 nm on the uncoated Si to as tall as 620 nm on the hydrophobic SAM coated substrate. To optimally lens 5 μm light, the 1 μm – 4 μm diameter features should have a height of 1 μm. Lensing is still observable with a smaller feature height, but the results could be improved by printing higher aspect ratio features.

4.1.5 *Conclusions*

In this study, a fully additive, maskless process for printing TiO_2 meta-optical lenses made with femtoliter dropwise control is achieved. The materials development research presented in Chapter 3 resulted in a TiO_2 precursor printing solution that led to the fabrication of the first ever fully printed functional mid-infrared meta-optical lens that demonstrated focusing of 5μm wavelength light. The ethylene glycol based ink was investigated before the research into the 1,4-butylene glycol ink. As a result, the first metasurface lenses were printed and tested out of the ethylene glycol printing solution. Improvements have been made to the TiO_2 alkoxide precursor printing solutions and section 4.2 presents the research outcomes associated with using the improved 1,4-butylene glycol printing formulation to fabricate a new class of optical devices.

4.2 PLASMONIC BULLSEYE ANTENNAE

The motivation to bring the signal transmission efficiency gains of antennae, as seen in the radiowave and microwave regimes of the electromagnetic spectrum, to the optical regime has existed for several decades. [63] Prior to the advancements made in nanofabrication, the successful development of an optical wavelength antenna was restricted by the limitations of the fabrication tools. Antennae have characteristic dimensions on the order of the length of the wave for which they are designed to be used. At the optical scale, this requires device fabrication capabilities down to the hundreds of nanometers, with individual instrument precision well below that. At this point, nanofabrication instruments are more than capable of meeting the dimensional requirements to fabricate optical antennae. As such, significant advancements have been made in this research space. [64], [65], [66]

The first generation of optical and plasmonic antennae were fabricated out of metals, such as silver or gold, which demonstrated excellent focusing of electric fields at the geometric center of a device. However, these noble-metal structures suffer from significant ohmic loss due to intrinsic material properties, which presents a meaningful limitation in the field. As a result, alternative materials for the bullseye structures have been proposed and tested. One promising area of material exploration for plasmonics are ceramics, such as TiO_2. Similar to the advances of using TiO_2 as a primary material in meta-optical lenses, TiO_2 plasmonic devices show substantially less loss than comparable metallic devices, have a high degree of material stability, and maintain excellent signal directionality. [67]

The idea to couple the advances in plasmonic antennae with nanocrystal quantum dot emitters (QD) emerged as a method to spatially narrow omnidirectional emission pattern of QDs, thus concentrating the signal towards a detection point and significantly increasing the efficiency

of photonic emission collection. The concentric circle pattern, or bullseye, grating is optimal for QD emission pattern shaping due to the circular symmetry of the resulting beam, which is the preferred shape for most applications. [68] In a study by Anderson et al., a dielectric (TiO_2) plasmonic bullseye antenna is coupled with a nanodiamond to demonstrate a substantial emission beam narrowing around the critical wavelength (675 nm). [69] However, this method relies on a bullseye grating fabricated by electron beam (e-beam) lithography and the nanodiamond emitter is transferred to the center of the bullseye by an AFM "pick and place" technique. Both of these methods are time consuming non-scalable processes, with e-beam being a particularly energy intensive fabrication process. As such, there is a clear opportunity to use the advances made in high-resolution EHD printed ceramics, as discussed in earlier chapters, and EHD printed QDs accomplished by research collaborators [33], to make a fully EHD printed plasmonic bullseye antenna to improve the directionality and photon collection efficiency of an EHD printed QD.

4.2.1 *Near-Infrared Plasmonic Bullseye Design*

Combining the photonic emission beam narrowing and signal strengthening benefits of a bullseye plasmonic antennae with a near-infrared (NIR) spectrum emitting QD on its own is a valuable area of study. Using fully additive printing methods to create such a device would result in a groundbreaking achievement. Therefore, a hybrid plasmonic bullseye antenna was designed around the demonstrated capabilities of EHD printed TiO_2 to focus 1530 nm light. This couples well with the ~1540 nm emissions peak of Er^{3+}/Yb^{3+} doped $NaYF_4$ nanocrystal. The nesting of this nanocrystal in a compatible bullseye antenna should show a significant reduction in emission beam spreading and an increase in peak signal intensity.

Figure 4.5 shows the designed bullseye structure from several perspectives. The pattern was designed around the known limitations of the EHD printer and printable material, particularly

the thickness of each ring, which is designed to be 250 nm. Figure 4.5 (a) shows an angled wide-view of the grating, which is made up of 25 concentric rings. Figure 4.5 (b) shows a top-down, close-view of the bullseye pattern. Each ring is 500 nm wide and there is a 600 nm space between each ring. The overall pitch (1.1 μm) is based on the peak emission wavelength (1540 nm) of the nanocrystal to be used in tandem with this antenna. Figure 4.5 (c) and (d) depict cross sections of the device. The close-view cross section in Figure 4.5 (d) highlights the distinct layers of the substrate necessary for the function of this device.

The specialize substrate stack (Figure 4.5 (d)) on which the bullseye is printed is designed to maximize the signal while minimizing losses due to absorption or recombination. The base of the substrate is Si with 50 nm of gold evaporated, followed by a thin (5 nm) layer of TiO_2 to act as an adhesion promotion layer, and finally a 1 μm layer of SiO_2. Fabrication of the substrate thinfilm stack without the 5 nm layer of TiO_2 resulted in poor adhesion of the SiO_2 to the underlaying gold layer. Without the TiO_2 between the Au and SiO_2 there is significant or total

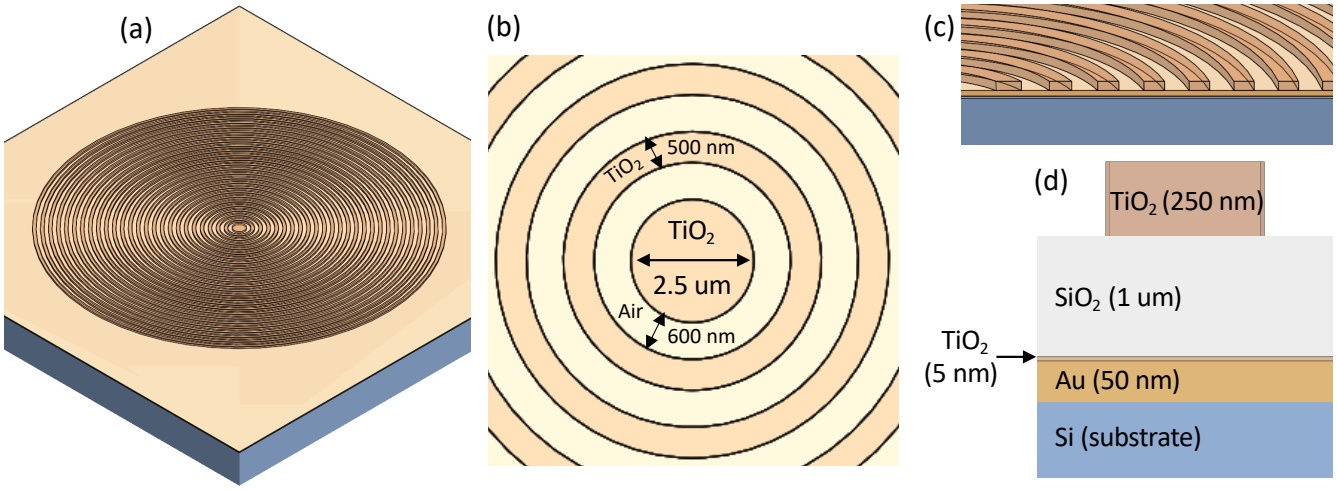

Figure 4.5. Plasmonic bullseye design showing (a) wide view (b) top-down close view (c) cross-section wide view and (d) cross section close view.

delamination of the SiO_2 thinfilm. Since the inclusion of TiO_2, there has been no observed degradation of the SiO_2 layer.

The plasmonic bullseye antenna has a modeled peak performance at ~1530 nm, shown in **Figure 4.6** (a). This near perfect match between the peak near-IR emission of the nanocrystal (~1540 nm) and the wavelength showing peak resonance in the plasmonic bullseye indicates that the combination of the nanocrystal and bullseye antenna should show a significant concentration in the emission pattern. Figure 4.6 (b) shows the response of a 1526 nm signal to the designed bullseye antenna. Significant concentration of the signal is observed in comparison to the signal without the bullseye antenna (Figure 4.6 (c)). The preliminary results of the EHD printed bullseye

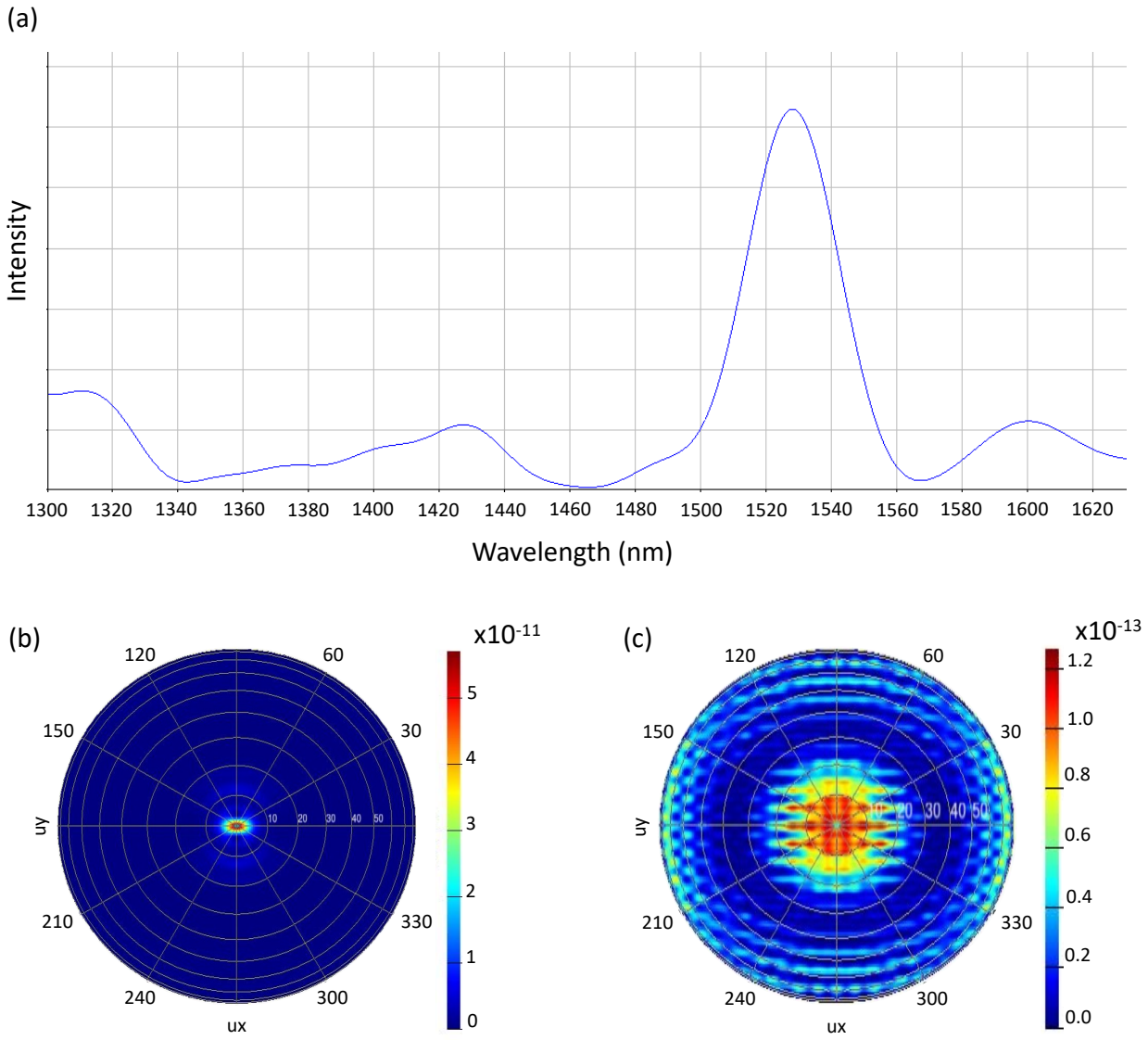

Figure 4.6. (a) Near IR emission spectrum erbium doped QDE showing resonance ~1530nm. (b) In plane dipole source of QD with bullseye antenna and (c) without the bullseye. *Presented with permission of project collaborator, David Sharp.

are presented in subsection 4.2.3 and the quality of the device still needs to be tested. However, if the collected data closely matches the modeled data, a strong plasmonic resonance response and nanocrystal emission beam shaping should be observed.

4.2.2 *Lanthanide Doped Sodium Yttrium Fluoride Nanocrystals*

The quantum dot emitter to be combined with the plasmonic bullseye antenna is a rare earth ion doped nanocrystal made from sodium yttrium fluoride ($NaYF_4$) doped with Er^{3+}/Yb^{3+} ion. [70] Lanthanide doped $NaYF_4$ are phosphors, meaning the crystalline material shows luminescence upon excitation. [71] Lanthanide doped $NaYF_4$ can both upconvert longer wavelength light to result in a shorter wavelength emission and down convert shorter wavelength light to result in longer wavelength emission. The down converting, or red shift, in the radiation can result in a larger number of emitted photons compared to absorbed photons while observing the rules of conservation of energy. Known as quantum cutting, this process takes a higher energy photon and "cuts" it into two lower energy photons. [72] It is important to note that $NaYF_4$ is a non-stoichiometric material in which Na^{1+} and Y^{3+} are randomly distributed over the same lattice site [73], [74] and the ratio of Na^{1+} to Y^{3+} is continuously tunable with different ratios present in different syntheses. Depending on the concentration of the trivalent lanthanide ions (Ln^{3+}) and the phase of $NaYF_4$, the rare earth dopants occupy different lattice sites in the crystal structure. This results in different available electron energy states and thus different energy transfers resulting in emissions of different wavelengths. [75]

The two phases of $NaYF_4$ commonly presented in literature, in both bulk and nanocrystal forms, are the cubic (alpha, α-$NaYF_4$) or hexagonal (beta, β-$NaYF_4$) phase and the synthesis method effects the resulting phase and size of the $NaYF_4$ nanocrystals. [74], [76] The phase impacts the location of Ln^{3+} in the crystal structure, which impacts the crystal symmetry and the distances between the rare-earth ions. [75], [77] Compared to α-$NaYF_4$, β-$NaYF_4$ shows lower crystal symmetry and shorter distances between the rare-earth ions. This results in more efficient energy transfer between the electron states Ln^{3+}, which improves the upconversion efficiency. [77]

There exists a range of Ln^{3+} couple dopants in $NaYF_4$ that result in quantum cutting through energy transfer. The Yb^{3+}, Er^{3+} couple are common co-dopants due to the efficient energy transfer from Yb^{3+} to Er^{3+}. [78] Specifically, the transition from the ground state ($^2F_{7/2}$) to the $^2F_{5/2}$ state in Yb^{3+} is achievable by excitation with a 980 nm source and is an important step for subsequent energy transfer or energy transfer upconversion to Er^{3+}. [79] Many in depth studies have been conducted to show the wide range of possible excitation and relaxation paths between Yb^{3+} and Er^{3+} [70], [72], [78], [79], [80]leading to discrete emissions peaks from the visible to the near-IR. Furthermore, studies have shown that the presence of Yb^{3+} as a co-dopant with Er^{3+} increases the emissions intensity of several wavelengths in the NIR region of interest. [72] Researchers have correlated the wavelength and intensity of the emissions to different factors such as nanocrystal size, Ln^{3+} concentration, crystal phase, and excitation source wavelength. [72], [73], [81]

The emission peak of interest in Er^{3+}/Yb^{3+} doped $NaYF_4$ to combine with the printed plasmonic bullseye antenna is at 1540 nm and there are multiple pathways in a $NaYF_4$: Er^{3+},Yb^{3+} nanocrystal to result in emission at the this wavelength. [79] Using a thermal decomposition synthesis method, Xu et al. show the formation of β-$NaYF_4$ doped with Er^{3+}/Yb^{3+} at two different sizes (~10 nm and ~ 200 nm) and varying dopant concentrations (Yb^{3+}:0%-20%, Er^{3+}: 2%). Their results indicate that there is an emission peak at 1540 nm, as well as other wavelengths, for 10 nm nanocrystals with Yb^{3+} concentrations of 0% and 20% and for 200 nm nanocrystals with Yb^{3+} concentrations of 0%, 2%, 5%, 10% and 20% when measured at room temperature and under 520 nm excitation. In the Xu et al. study, the nanocrystal with the strongest 1540 nm emission while under 520 nm excitation is the β-$NaYF_4$: Er^{3+} (2%), Yb^{3+}(5%). This emission peak is attributed to the following transitions in Er^{3+}: $^4I_{9/2} \rightarrow {}^4I_{13/2}$, and $^4I_{13/2} \rightarrow {}^4I_{15/2}$. The path to these emission peaks can occur in different steps. In one example, upon 520 nm excitation, the $^2H_{11/2}$ state becomes

occupied. From this state, non-radiative relaxation (nRR) occurs from $^2H_{11/2} \rightarrow {}^4S_{3/2}$, $^4S_{3/2} \rightarrow {}^4F_{9/2}$, and $^4F_{9/2} \rightarrow {}^4I_{9/2}$. Then quantum cutting is observed and two ~1540 nm photons are emitted, corresponding to the $^4I_{9/2} \rightarrow {}^4I_{13/2}$, and $^4I_{13/2} \rightarrow {}^4I_{15/2}$ transitions. Other relaxation paths are possible resulting in two different IR wavelength emissions, one corresponding to 1540 nm and another IR photon at a different wavelength. [72] In another study by Lee et al. [79], their investigation into β-$NaYF_4$: Er^{3+},Yb^{3+} indicates another transition ($^4F_{5/2} \rightarrow {}^4F_{9/2}$) that equates to the energy of 1540 nm emission. In this instance, return to the ground state ($^4I_{15/2}$) in Er^{3+} can result in 655 nm emission (red, visible region) due to the $^4F_{9/2} \rightarrow {}^4I_{15/2}$ transition. This set of transitions is only observed when the material is excited by a higher energy photon (441 nm). In summary, the multiple transition paths in $NaYF_4$: Er^{3+},Yb^{3+} resulting in ~1540 nm emission justifies the exploration of this material as an optimal nanocrystal emitter to couple with the designed plasmonic bullseye antenna.

For use in EHD printing, the 200 nm nanoparticles showing the strongest 1540 nm emission from the Xu et al. study are on the cusp of being too large. A general rule for printing with nanoparticles is that the nanoparticles should be at least 10x smaller than the inner diameter of the nozzle at the point of ink ejection. Using a 2 μm nozzle, 200 nm nanoparticles are right on the edge of what is feasible. Given that, a different synthesis method or phase may be necessary to produce Er^{3+}/Yb^{3+} doped $NaYF_4$ nanocrystals smaller than 200 nm.

The research collaborators aiding with the synthesis of the Er^{3+}/Yb^{3+} doped $NaYF_4$ to couple with the plasmonic bullseye antenna are presently using a thermal decomposition reaction that should result in α-$NaYF_4$ nanocrystals with an average particle size of ~27.6 nm. After synthesis, the addition of a capping ligand to the nanocrystals enables the formation of a stable dispersion in a nonpolar solvent such as hexane, toluene, or dichloromethane [70], making them a good candidate for successful EHD printing. As these nanocrystals have yet to be fully analyzed,

the long term colloidal stability, phase, average particle size and full emission spectrum have yet to be determined. Given the difference in phase, particle size, and Yb^{3+} concentration between the present synthesis method and the results from Xu et al. and Lee et al. studies, it is possible that changes will need to be made to the working synthesis method in order to achieve the optimal particle size for EHD printing with the optimal emission at 1540 nm. It is also possible that the synthesis will be intentionally altered to result in β-$NaYF_4$, which demonstrates higher up-conversion efficiency compared to α-$NaYF_4$. [71], [76], [78] Such a change may results in a better performing device. Prior to the start of the investigation into printing the α-$NaYF_4$ nanocrystals capable of emitting at ~1540 nm, a related set of experiments were conducted using α-$NaYF_4$ with a different dopant concentration and a mean emission wavelength of approximately 1 μm. The results from these experiments are presented in subsection 4.2.4.

4.2.3 *EHD Printed Plasmonic Bullseye Antenna Results*

The development of the 1,4-butylene glycol based printing formulation (Chapter 3) with the determination that this ink has a longer effective printing window and results in smaller printed features than the ethylene glycol formulation, under uniform printing conditions, led to further exploration with this printing formulation. With the goal of achieving EHD printed TiO_2 features on the lengthscale of the plasmonic bullseye antenna design presented in section 4.2.1, additional experiments with the 1,4- butylene glycol were performed. These experiments resulted in higher resolution printed features than reported in our previously published study [55] and presented earlier in this dissertation.

Previously, we demonstrated printed features with a base width of 1 μm and a full width at half maximum height of ~835 nm. [55] The newly developed 1,4-butylene glycol based TiO_2 precursor printing formulation, used in combination with a 500 nm inner diameter printing nozzle,

resulted in printed features with a 500 nm base width and a full width at half maximum height value of ~380 nm. **Figure 4.7** (a) shows a wide view image of the 500 nm array of features and Figure 4.7 (b) shows a close-up topography AFM image of the same array. Figure 4.7 (c) shows a 3D rendering of an AFM image of the 500 nm features with Figure 4.7 (d) showing a representative feature cross-section. It is clear from these figures that 500 nm printed features, comparable to the wavelength of visible light, are reproducible over large areas.

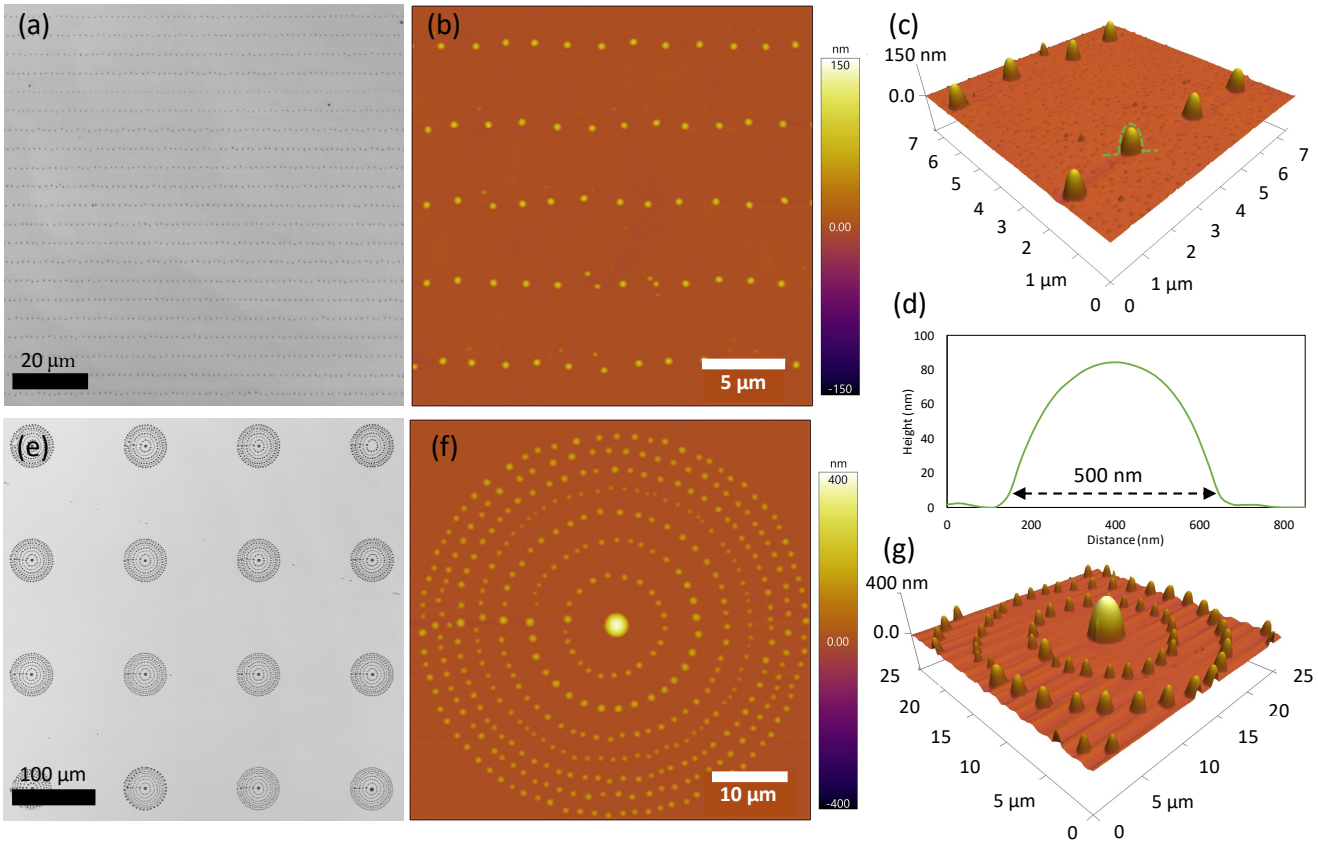

Figure 4.7. 1,4-butylene glycol TiO_2 precursor ink printed on polished Si in a range of patterns. (a) Optical profilometry image of square array of 500 nm features (b) AFM image of square array (c) 3D rendering of AFM image with (d) showing height and width of representative feature. (e) Optical profilometry image of bullseye plasmonic antenna style pattern (f) AFM of single lens (g) 3D rendering of center region of the lens.

The calculated liquid volume from the 500 nm features is 85 attoliters (aL). This is the first report of printing at the attoliter volume scale for the printed alkoxide family of materials. Huang et al. (2020) reported printing drops between 1 to 5 aL using a modified EHD method with a gold nanoparticle ink. [82] The printed examples presented in their study are similar size spatially to the printed features presented in this study and, for the purposes of fabricating effective metasurface and photonic structures, high aspect ratio and therefore taller deposits are more desirable. Also, the drop placement accuracy in Huang et al., appears to be significantly lower than that achieved in this work (Figure 4.7). Given these differences, an 85 aL EHD printed liquid feature is a substantial step forward in further improving the printing resolutions of metal oxide inks.

To demonstrate the advanced capabilities of the EHD printer and the practical benefits of reduced printed feature size, an array of plasmonic bullseye antenna-like structures are printed (Figure 4.7 (e)). The array of 16 bullseyes takes less than 1 minute to print and there is minimal variation between each printed feature. Figure 4.7 (f) shows an AFM image of one lens and Figure 4.7 (g) shows a 3D rendering of the center region of the printed bullseye. All of TiO_2 features and patterns shown in Figure 4.7 are printed on FOTS coated Si substrates, prepared in the manner described in Chapter 3. The quality and speed of fabrication demonstrates the feasibility for scaling this process up to result in high throughput and high precision nanomanufacturing.

The success of printing the 1,4-butylene glycol ink on polished Si, achieving the objective of printing features with a 500 nm base diameter, led to the experiment of printing the same formulation on the specialized Si-Au-TiO_2-SiO_2 substrates. As discussed in Chapter 3, the substrate-printing formulation interactions significantly impact the outcomes of EHD printing experiments. Consequently, changing the device substrate, while leaving all other variables unchanged, can lead to drastically different results. The Si-Au-TiO_2-SiO_2 substrates were treated

with the FOTS SAM in the same method as used for the polished Si wafer. Contact angle measurements of the printing formulation on the new substrate show similar results, with the possibility of 1° to 2° increase in the contact angle on the Si-Au-TiO_2-SiO_2 substrate compared to the Si substrate.

The most significant observable difference between the printing tests conducted on the Si substrates and those conducted on the Si-Au-TiO_2-SiO_2 substrates, are the post-printing and post

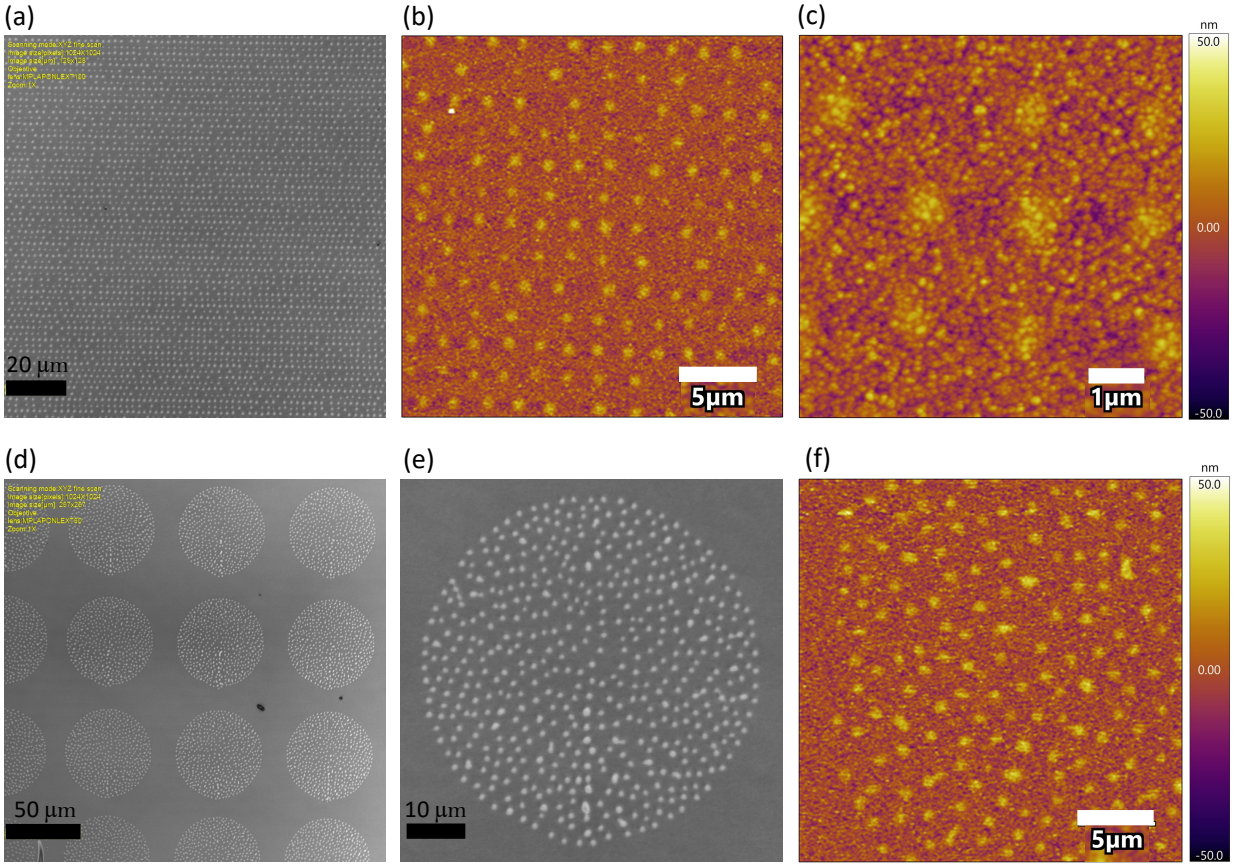

Figure 4.8. 1,4-butylene glycol TiO_2 precursor ink printed in a range of patterns on a Si-Au-TiO_2-SiO_2 substrate. (a) Optical profilometry image of 5 µm pitch square array of features (b) AFM image of square array (c) close-view AFM image highlighting significant substrate surface roughness. (d) Wide view and (e) close view of optical profilometry image of an array of plasmonic bullseye antenna-like patterns (f) AFM of single bullseye.

cross-linking steps. **Figure 4.8** shows a similar set of printing tests done on the Si-Au-TiO_2-SiO2

substrates as those conducted on the Si substrates (Figure 4.7). Figure 4.8 (a) shows a wide view optical profilometry image of a 5 μm pitch square array with Figure 4.8 (b) and (c) show AFM images of the same array at high resolutions. Figure 4.8 (d) shows an optical profilometry image of an array of plasmonic bullseye antenna-like patterns with Figure 4.8 (e) showing a closer view of one of the patterns in the array. These printed patterns are designed to have a 1.1 μm pitch such that there is a 600 nm edge-to-edge spacing between a 500 nm wide printed feature; the desired dimensions of the designed plasmonic bullseye antenna. Figure 4.8 (f) shows an AFM image of a printed bullseye.

AFM of the features printed on Si-Au-TiO_2-SiO2 substrates highlight the significant difference in surface roughness compared to the polished Si substrate. The root mean square (RMS) surface roughness of a polished Si substrate with the hydrophobic SAM coating is ~0.5 nm. This calculation is based on measurements taken on unprinted regions of substrates that contain printed samples. In contrast, the RMS surface roughness of the Si-Au-TiO_2-SiO2 substrate is ~10 nm. This value is based on the few initial AFM measurements of this substrate. As such, there is greater uncertainty in this value compared to the measurement of the Si substrate. However, the primary difference to note is that the RMS surface roughness of the Si-Au-TiO_2-SiO2 substrate is approximately 20x greater than that of polished Si. Surface roughness of this order, given the dimensions of the designed pattern, presents a significant fabrication challenge. It appears from the first round of experiments that the deposited printing formulation first fills in the troughs of the rough surface, resulting in the printed regions of the substrate appearing smoother but not resulting in features that are extruded from the substrate. It is possible that multiple rounds of printing the same material and pattern could results in features that ultimately extrude from the

substrate. However, this method was attempted without success on polished Si in an effort to increase the printed feature aspect ratio, so it's uncertain if this approach will be successful.

The images in Figure 4.8 also show that there are significant improvements to be made regarding the accuracy of the printed patterns. Even without the extrusion issues, the printed patterns are significantly off from the designed pattern (Figure 4.5). Since printing the examples presented here, new EHD printer patterns and fabrication orders have been designed in an effort to address the observed issues.

4.2.4 *EHD Printed $NaYF_4$ Results*

In order to successfully couple a printed QD with a printed plasmonic bullseye antenna, it is first essential to determine the optimal printing formulation and process that results in successful ink jetting and functional emitters, post printing. Research peers determined the optimal formulation and method to result in printed, functional $CsPbBr_3$ nanocrystals with an average edge length of 9.7 ± 2.1 nm and a post-printing emission peak at 517 nm. They also determined an optimal process for printing these perovskite nanocrystals with a high degree of accuracy such that a low volume of nanocrystals can be printed on prefabricated nanobeam cavities with sub-micrometer precision. [33] This research study shows that it is possible to successfully print nanocrystals, susceptible to environmental degradation, that maintain functionality post printing with a degree of printing accuracy that meets what is necessary for the application in fully printed hybrid plasmonic bullseye antennae with coupled QDs. However, there are significant differences between the perovskite nanocrystals successfully EHD printed by our research group peers and the lanthanide doped $NaYF_4$ nanocrystals necessary to produce the 1540 nm emission to be tuned by the plasmonic bullseye resonator. As such, significant research is required to determine the optimal printing formulation and process to result in post-printing functional $NaYF_4$ nanocrystals.

To date, there does not exist a peer reviewed publication on EHD printed Er^{3+}/Yb^{3+} doped $NaYF_4$ nanocrystals. This presents both an exciting opportunity and a significant challenge as there is no obvious path that leads to successful printing of this material. In order to determine the parameters for successful printing of $NaYF_4$ nanocrystals, preliminary investigations into the optimal printing formulation and EHD printing process for $NaYF_4$ nanocrystals have been executed. The intended outcome of the synthesis performed for the purpose of EHD printing trials was to result in spherical α-$NaYF_4$ nanocrystals with diameters in the range of 130 nm. After the nanocrystals synthesis, which was carried out by research collaborators [74], there was an attempted suspension of the α-$NaYF_4$ in ethylene glycol. As discussed in Chapter 3, ethylene glycol is compatible with EHD printing and previous printing trials show that ethylene glycol based formulations result in high resolution printed features. Furthermore, ethylene glycol was selected due to its similarity to polyethylene glycol, which is known by our collaborators [83] to be compatible with α-$NaYF_4$. Prior to printing, the ethylene glycol α-$NaYF_4$ mixture is filtered through a water-wetting PTFE filter to minimize the likelihood of nozzle clogging due to agglomerated nanocrystals. Two main types of printing patterns were attempted: square arrays of features printed using the dropwise mode and concentric circles in Fresnel lens-like or bullseye-like patterns printed using the continuous mode. Images of the ethylene glycol α-$NaYF_4$ printing trials are presented in **Figure 4.9**. The square arrays are shown in Figure 4.9 (a-c), with Figure 4.9 (a) showing an optical profilometry image of dropwise features with ~ 3 μm diameter and Figure 4.9 (b) showing and AFM image of dropwise features with diameters as small as 400 nm (Figure 4.9 (c)). Images of the Fresnel lens-like and bullseye-like patterns are shown in Figure 4.9 (d-i). Two different examples of these patterns are shown in Figure 4.9 (d) and (g). AFM images of a

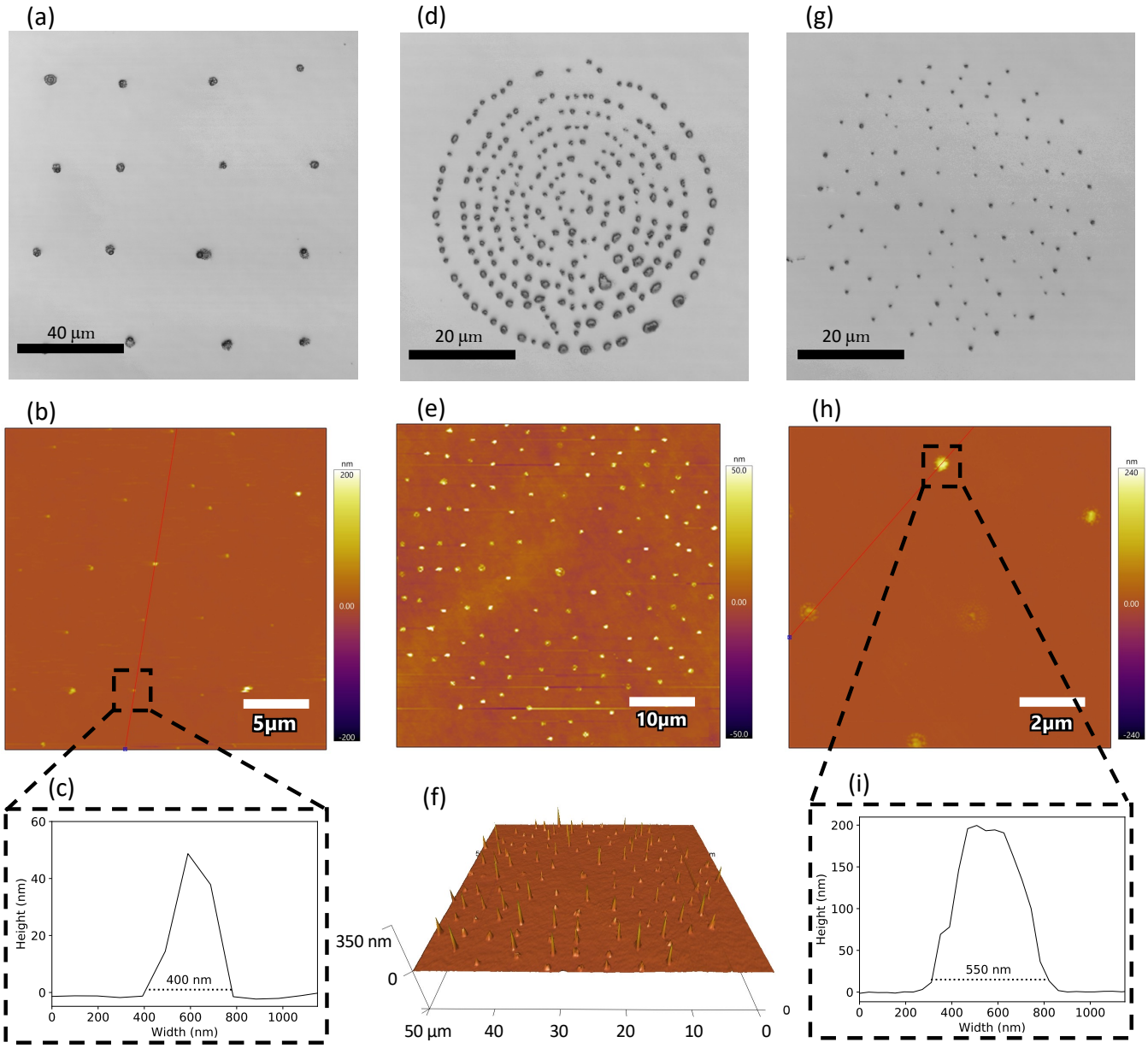

Figure 4.9. Images of EHD printed cubic $NaYF_4$ printing formulation. (a) Optical profilometry of square array with ~3 µm features, (b) AFM of square array with ~400 nm diameter features, shown by (c) the detailed profile of a printed feature. (d) Optical profilometry of Fresnel Lens like structure, (e) AFM image, wide view, of Fresnel Lens like structure (f) 3D representation of pattern. (g) Concentric circle dot pattern, (h) close view of Fresnel Lens like structure from (e), (i) detailed profile of printed feature from (h).

longer pitch, smaller feature diameter pattern is shown in Figure 4.9 (e), (f), and (h). The individual features in this family of patterns have diameters of ~550 nm (Figure 4.9 (i)) or possible smaller.

The high resolution of the ethylene glycol α-$NaYF_4$ formulation printed features, showing printed features on the scale of 400 nm, is a promising result. However, post-printing analysis of the printed material's emission spectrum did not reveal an emission peak characteristic of the Yb^{3+} dopant present in the originally synthesized α-$NaYF_4$ and subsequent testing revealed only trace amounts of Na and Cl ions indicating that Yb^{3+} doped materials were not printed. Furthermore, subsequent characterization of the α-$NaYF_4$ mixed with ethylene glycol showed a bimodal size distribution of nanoparticles, indicating that particle degradation might be occurring in the ethylene glycol formulation prior to EHD printing.

4.2.5 *EHD Printed $NaYF_4$ Discussion*

The lack of an emission peak characteristic of the Yb^{3+} dopant is a disappointing initial result but the issues with the original ethylene glycol printing formulation appeared early on. First, the α-$NaYF_4$ did not disperse well in ethylene glycol and all mixtures shared by project collaborators contained a dense mass of material at the bottom of a conical centrifuge tube. It was challenging to both draw the nanocrystal mixture out of the tube with a syringe due to the settled material and subsequently difficult to filter the material in the syringe prior to printing. In addition to particle degradation that might be occurring as a result of the inclusion of ethylene glycol, the filtration process may also be negatively impacting the nanocrystals prior to printing. Finally, the applied electric field that is essential to the EHD printing method, might be resulting in nanoparticle degradation during printing.

In order to determine at which point the α-$NaYF_4$ nanocrystal degradation is occurring, more detailed analysis of the nanocrystals needs to occur at each step of the synthesis to post-

printing process. Nanocrystal phase analysis and determination of the presence of Yb^{3+} through the detection of the characteristic emission peak should be conducted at each step. This will make clear which procedure is negatively impacting the nanocrystals and alternative methods can be tested to determine the optimal process to successfully print functional $NaYF_4$ nanocrystals. Additional discussion on how to improve the α-$NaYF_4$ printing dispersion, based on the dispersion developed for the research in subsections 4.2.1 to 4.2.3, is presented in section 4.3.

4.2.6 *Conclusions*

The ability to print the smallest ever reported printed feature and ejected drop volume for the particle free, metal oxide class of materials is primarily due to the optimized material properties of the 1,4-butylene glycol printing solution. Substantial improvements in the stability of the titanium alkoxide ink enabled the use of higher resolution printing nozzles, which clog much more easily than the wider nozzles. The high boiling point of 1,4-butylene glycol and lack of ink gelation, means that 500 nm inner diameter (ID) nozzles can now be used while maintaining a multi-hour effective printing window. The ID of the nozzle tip impacts the size of the liquid cone that forms upon the application of the electric field. This has the effect of changing the volume of the drops that break off the formed jets as the smaller inner diameter nozzles result in smaller ejected drops. [12], [20]

This substantial reduction in feature size, aided by the narrower inner diameter nozzle, resulted in the consistent printing of 500 nm features made with a particle free, metal oxide ink and the first experiments into EHD printing a plasmonic bullseye antenna to focus 1530 nm light. The features printed in bullseye-like patterns on polished silicon show that the dimensions of the functional bullseye pattern is attainable and the first tests of the functional pattern on Si-Au-TiO_2-SiO2 substrates have helped to define the next phase of research.

Finally, a preliminary set of experiments using the dropwise and continuous printing mode of the EHD printer was conducted with undoped and doped $NaYF_4$ nanocrystal formulation. These tests resulted in some material jetting and nanoscale printed features, but the post printing analysis indicated that the nanocrystals had degraded since the original synthesis and the characteristic emission indicating the presence of Yb^{3+} was not observed. These nanocrystals differ slightly from the $NaYF_4$ nanocrystals to be coupled with the TiO_2 plasmonic bullseye antenna but retain enough similarity such that the development of a successful process to EHD print this variety of $NaYF_4$ nanocrystals could only serve to assist in the development of a process to print the Er^{3+}/Yb^{3+} doped $NaYF_4$ optimized to emit at 1540 nm.

4.3 EHD Printed Meta-Optics, Photonics, and Plasmonics Future work

The primary shortcoming in the TiO_2 inks presented and the resulting printed features is minimal control over the printed feature aspect ratio. The performance of the meta-optical lenses and the plasmonic bullseye antennas is limited by the vertical height of the printed features, which limits the achievable phase coverage for the meta-optics and reduces resonance of the bullseyes. Further increasing the aspect ratio of the printed features through ongoing materials, surface and process engineering will improve the device performance and efficiency.

Using the knowledge gained from the initial TiO_2 ink development research, further adjustments to the printing formulation can be made in pursuit of higher aspect ratio features. The same rigorous materials analysis and printed feature characterization study should be conducted to determine the correlation between printing solution properties, air-solution-substrate interface, and the resulting printed feature aspect ratio. A few methods for increasing the EHD printed feature aspect ratio are actively being investigated and continued literature search could highlight additional methods. Developing the capabilities for material deposition control between 10 nm in

x-y area and greater than 1 μm in the z-direction will expand the versatility and capabilities of EHD printed metal oxides.

One pathway to increase feature height and aspect ratio is through the addition of TiO_2 nanoparticles, resulting in a composite titania nanoparticle and titanium alkoxide ink. Metal nanoparticle and organic functional inks have been used to create very high aspect ratio features [18], and a similar approach could be taken to increase the aspect ratio of EHD printed TiO_2. The nanoparticles could enable higher aspect ratio features compared to particle free inks, as well as an increase in viscosity of the printing solution, that can lead to reduced lateral droplet spreading before solvent loss and increasing viscosity effectively freezes the droplets maximum lateral dimensions. The high melting temperature of oxides makes a solely nanoparticle-based printing formulation undesirable, as the printed features are more likely to be discontinuous, porous, and adhere poorly to the substrate. However, combining the alkoxide precursor printing formulation, which convert to crystalline TiO_2 at 450 °C and amorphous TiO_2 well below that, with TiO_2 nanoparticles could result in a printing formulation that enables higher aspect ratio features from a given droplet volume while still being able to bind the nanoparticles together with TiO_2 and the substrate.

An area of concern when considering nanoparticle based printing formulations is the increased possibility of nozzle clogging due to aggregation and settling of the particles at the nozzle tip. A few recently developed alkoxide precursor-TiO_2 nanoparticle hybrid inks have been through a limited set of initial tests, helping to highlight potential benefits and pitfalls with working with this type of inks. Using a very high concentration of poorly dispersed TiO_2 nanoparticles led to rapid nozzle clogging, even when mixed with into a high viscosity solution that should reduce the rate of particle settling. In an effort to avoid this issue, an ink with a very low concentration of

well-dispersed TiO_2 nanoparticles was tested. This solution did not result in nozzle clogging for the duration of the printing tests (~3 hours) but the printing tests to date have only shown minimal gains in improving the average feature aspect ratio. Thus far, only limited materials analysis and EHD printing tests have been conducted with this new family of inks and much more research needs to be completed in this space.

The addition of TiO_2 nanoparticles could also lead to an increase in the refractive index of the printed features. There is a positive correlation between an increasing refractive index and a reduction in the focal length of the measured metasurface lens, which is a device benefit for ultraflat optics. [38] At a wavelength of 5 μm, the effective refractive index of the printed TiO_2 structures is 1.9. This is lower than the refractive index of bulk TiO_2 at this wavelength, which is 2.24. One reason for the lower refractive index is due to the blend of PVP and TiO_2 in the printed structures. During the high temperature sintering process that is performed after printing, the PVP burns out and the remaining structures are converted to anatase. This results in some porosity in the TiO_2 with an effective refractive index proportional to the fractions of TiO_2 and void spaces that are below the refractive index of bulk TiO_2. The addition of TiO_2 nanoparticles could result in printed features with a higher ratio of TiO_2 to PVP as well as an overall higher solid loading of the precursor ink, leading to a higher effective refractive index with or without a high temperature alkoxide conversion process. These factors are pathways towards improved EHD printed meta-optical lenses, plasmonic bullseye antennas and other optical devices.

Improvements in the printed TiO_2 formulations as a key step to realizing a fully printed and functional plasmonic bullseye antenna with a coupled near-IR QD emitter. In addition to this step, there also needs to be improvements in substrate fabrication to achieve lower surface roughness films. One possible route to reducing the surface roughness of the Si-Au-TiO_2-SiO_2

substrates is through a process called template stripping. This method makes use of a sacrificial layer of ultraflat material, upon which the desired substrate stack is built. After the deposition steps have taken place, the sacrificial layer is removed revealing an extremely smooth substrate with root-mean squared surface roughness as low as 1nm. [84] If achieved, this 10x reduction in surface roughness would come close to matching the surface roughness of the polished Si wafer, resulting in printed features that extrude from the surface, as intended, leading to significantly improved performance of the EHD printed plasmonic bullseye antenna without any changes in the printed material formulation.

Finally, the realization of a coupled plasmonic device with NIR nanocrystal emitter hinges on the full development of EHD printed Er^{3+}/Yb^{3+} doped $NaYF_4$ nanocrystals. Currently, there persists the issue of creating a stable $NaYF_4$ nanocrystal printing formulation made up of uniformly dispersed nanocrystals that maintain functionality through the necessary printing and post-printing processes. This could be addressed by adding or adjusting the presence of a capping ligand on the nanocrystals to create a stable colloidal dispersion. The Er^{3+}/Yb^{3+} doped $NaYF_4$ nanocrystals presented in section 4.2.2 are stably dispersed in nonpolar solvents as part of the original synthesis process. Conversely, the nanocrystals presented in sections 4.2.4 and 4.2.5 were attempted to be suspended in a polar solvent (ethylene glycol). It is unclear of the $NaYF_4$ nanocrystals from those experiments are generally unstable ethylene glycol or if the post-synthesis, washing, and redispersion process could be adjusted to result in a stable colloidal dispersion in ethylene glycol or a similar solvent. If efforts to disperse the $NaYF_4$ nanocrystals from subsections 4.2.4 and 4.2.5 in a polar solvent are unsuccessful, adjusting the synthesis or post-synthesis process to allow for the nanocrystals to be dispersed in a nonpolar solvent should be considered. It is important to note that peer researchers have had success printing a different family of nanocrystal emitters in both

polar and nonpolar solvents. If the nanocrystals are polarizable, successful EHD printing can occur in both polar and nonpolar solvents. As such, it was not apparent from the start of the research presented in section 4.2 that a nonpolar solvent should be prioritized in order to result in an optimal nanocrystal printing dispersion.

The diameter of the nanocrystals in the $NaYF_4$ dispersion from subsection 4.2.2 is also substantially smaller (~27 nm) than the nanocrystals for the Fresnel lenses in subsections 4.2.4 and 4.2.5 (~130 nm). The smaller nanoparticles may form a stable dispersion more easily and may result in fewer instances of EHD nozzle clogging, two properties that are advantageous for successful EHD printing. If stable dispersion issues persist after adjustments are made to the capping ligands and the solvent, adjusting the synthesis process to result in nanocrystals smaller than 130 nm and investigations into the stability of smaller nanoparticle dispersions should be conducted.

In summary, there are many possible paths for future research and development of the EHD printing technique as it relates to printed meta-optics, photonics, and plasmonics. Specifically, investigations into improving both particle-free and nanoparticle based metal oxide printing formulations to result in greater printed feature control in the x, y, and z directions will lead to improved device performance. There is also a substantial amount of research to be conducted in EHD printed nanoparticle upconverters and downconverters. Expanding the library of stable nanoparticle emitter dispersions that maintain functionality post printing, will in turn expand the range of devices possible to fabricate via EHD printing. This work needs to be conducted for both metal rare earth fluorides, such as $NaYF_4$, and other families of materials. This research is especially valuable to explore due to the novelty of the field and the capabilities of EHD printing that enable a scalable path for direct deposition of a low volume of QDs. The research remaining

in the space of EHD printed meta-optics, photonics, and plasmonics are nontrivial tasks but the depth of knowledge attained, and skills developed to achieve the milestones presented in this dissertation make it apparent that the next set of objectives can be achieved.

Chapter 5. CONCLUSIONS

This dissertation presents in-depth functional and theoretical examples of high resolution electrohydrodynamic inkjet printing, with a specific focus on functional titanium alkoxide printing formulations and applications in meta-optical and photonic devices. While the methodology behind EHD printing has existed for decades, the more recent turn towards additive manufacturing techniques as a more sustainable alternative to traditional manufacturing and fabrication methods has reignited interest in EHD printing. This resurgence of research interest in EHD printing has resulted in new developments across a wide range of disciplines. Despite the many innovative applications of EHD printing alongside thorough investigations into the fundamentals of the dynamics of fluids under electrostatic influence, there remains a wealth of underexplored topics. This dissertation, and the published works on which the content is based, aimed to shed light on a few of the underexplore research areas and draw attention to novel applications of this widely applicable technique.

The innerworkings of the EHD printer were explored in Chapter 2. The information presented in this chapter is based both on literature and knowledge gained through experimental research. The details of the tool used to conduct the experimental research in the subsequent chapters are placed alongside examples of other experimental setups commonly presented from literature. The priority of the chapter is to the give the reader the fundamental information necessary to meaningfully understand the methods, results, and conclusions of the later chapters. It should be clear from this chapter that the interplay of classical mechanics, fluid dynamics, and electrostatics in the EHD printer and on EHD printed materials results in a complex system that requires the consideration of many variables before drawing any conclusions. A subset of these variables and their impact on EHD printed materials are explored in the next chapter.

In Chapter 3 of this dissertation, a range of titanium alkoxide precursor printing formulations with different material properties were presented. These properties were measure and compared to results of the printed materials in an effort to determine the impact of a material property on the final printed feature geometry. The material properties explored in this chapter are viscosity, surface tension, substrate-ink contact angle, primary solvent boiling point, and relative permittivity. The dimensionless Ohnesorge number, which combines viscosity, surface tension, and the characteristic drop length of a fluid, is also considered and compared to the final printing outcomes. Lastly, the effective printing use time of an ink is defined and the causes of a short or long use time are investigated. One main conclusion from this chapter is that printing outcomes depend on the innerworkings of many variables and there is not a singular, definitive property that predicts the printed feature outcome. In addition to this overarching conclusion, it is apparent that the viscosity of the printing formulation is an important material property to consider and should be tuned to achieve the printing objectives.

The initial exploration of the electrical permittivity and the relative permittivity of the printing solutions presented in Chapter 3 opened the doors to an underexplored or under considered area of materials research for EHD printing. The conclusions from this section are first that this property should be measured for every material considered for EHD printing in order to seek out any optima regimes for printing. Second, in contrast to other literature, in this study the materials with the lowest relative permittivity compared to the other materials considered, resulted in the smallest printed feature. This result led to calculations of the liquid printed feature, prior to solvent evaporation. This in turn led to the realization that when there are variables in the material properties, the ejected drop volume does not directly correlate to the width or area of the dried, printed feature. All other known examples in literature that investigate the impact of relative

permittivity on the extruded fluid stop at measuring the impact on the ejected drop volume and do not explore the subsequent interactions between the printed material and the substrate.

The material properties research in Chapter 3 resulted in two titanium alkoxide printing formulations that are capable of printing 1 μm features and smaller. The two inks, one ethylene glycol based the other 1,4-butylene glycol based, have several similar material properties but a distinct difference in effective printing use time. Although the two solvents are molecularly quite similar, the ethylene glycol formulation results in a pseudosolid gel after approximately 24 hours. These changes are observable in the bulk printing formulation after a few hours and these changes appear to result in clogging of the printing nozzle. Over the same period of time, the 1,4-butylene glycol ink has no observable changes.

As a result of the ink development research presented in Chapter 3, applications of the high refractive index materials in the field of meta-optics and photonics are possible, and the results are presented in Chapter 4. Even though there are demonstrated shortcomings with the ethylene glycol ink as it pertains to stability, the initial success in printing 1 μm features resulted in the first fully printed meta-optical lens. This technique was used to create mid-IR optical metasurface lenses that demonstrated focusing of 5 μm wavelength light. Lensing of 5 μm light was observed at the designed focal depth of 1 um. Although there are opportunities for further improvements in the printing materials and process to increase precision, printing consistency, feature aspect ratio, refractive index, and lensing efficiency, the reported results are the first of its kind both in the fields of printed meta-optics and EHD printed metal oxides.

The 1,4-butylene glycol based titanium alkoxide printing formulation is an improvement upon the ethylene glycol based formulation in most areas, especially in the realm of ink stability. The 1,4-butylene glycol inks are stable in ambient laboratory conditions and in the printing nozzle

for extensive periods of time. The effective printing use window is at least 5 hours and likely much longer. This improvement in stability was made without sacrificing printing resolution. As a result, the 1,4-butylene glycol ink is compatible with 500 nm inner diameter printing nozzles and was used to print individual features with a base diameter of 500 nm, significantly smaller than the 1 μm diameter features from the ethylene glycol formulation. The higher resolution printing capabilities expand the range of applications for EHD printed metal oxides to include devices in the near-IR and visible spectra. The new capabilities were tested by the design and fabrication of a plasmonic bullseye antenna, designed with peak resonance at ~1530 nm. Initial fabrication tests of the bullseye pattern and of a $NaYF_4$ nanocrystal printing formulation that is related to the Er^{3+}/Yb^{3+} doped $NaYF_4$ nanocrystals to be coupled with the plasmonic bullseye antenna have been completed. The next phase of device research includes the successful coupling of a functional EHD printed plasmonic bullseye antenna and Er^{3+}/Yb^{3+} doped $NaYF_4$ nanocrystals such that there is observable resonance and emission beam narrowing at ~1540 nm. Achieving this objective would be a groundbreaking milestone in several fields of research.

The only shortcoming of the 1,4-butyelen glycol ink is that there is no improvement on the printed feature aspect ratio over the ethylene glycol ink. While significant improvements in the printed feature aspect ratio were achieved from the onset of this research, there has been a plateau in the curve of improvement. It is possible that the particle free printing formulations have reached a maximum for printed feature aspect ratio and the best path forward to increase the aspect ratio could be to include TiO_2 nanoparticles in the printing formulation matrix. This is a significant change to the printing system and will likely present a new or expanded set of formulation variables to consider. Initially, this would require the development of a novel printing formulation that includes a stable dispersion of TiO_2 nanocrystals in a titanium alkoxide matrix such that the usable

printing window is at least 2.5 hours. Subsequently, the same material properties tests should be conducted with the novel ink to make an accurate comparison to the particle free system. If such a formulation is successful, this would create yet another avenue of exploration for applications of EHD printed metal oxides.

Within the space of high resolution EHD printed metal oxides, the primary areas of future research are in device fabrication for an ever-shorter wavelength of light and materials development to achieve the device objectives. There are substantially fewer examples of printable metal oxide formulations presented in literature than there are for printable metals or pure organics, such as photoresists. The specific goals for the research presented in this dissertation would be more easily achieved with metal oxide printing formulations capable of achieving higher aspect ratio features, but not all applications require that condition. What is apparent is that printable, functional metal oxides is an underexplored area of research and future applications of EHD printing, within the bounds of meta-optics and photonics or not, will require a more diverse library of tested and understood printable materials. This dissertation represents a meaningful contribution to the expansion of knowledge on the subject of printable metal oxides and further research in this area is necessary to meet the demands of advanced and scalable additive manufacturing.

BIBLIOGRAPHY

[1] J. Carter, P. Lyon, C. Creighton, M. Bale and H. Gregory, "P-65: Developing a Scalable and Adaptable Ink Jet Printing Process for OLED Displays," *SID International Symposium Digest of Technical Papers* **2005**, 36, 1, 523-525.

[2] S. Burns, C. Kuhn, K. Jacobs, J. D. MacKenzie, C. Ramsdale, A. C. Arias, J. D. Watts, M. Etchells, K. Chalmers, P. Devine, N. Murton, S. Norval, J. King, J. Mills, H. Sirringhaus and R. Friend, "Printing of polymer thin-film transistors for active-matrix-display applications," *Journal of the Society for Information Display* **2003**, 11, 4, 599-604.

[3] A. C. Arias, J. D. MacKenzie, I. McCulloch, J. Rivnay and A. Salleo, "Materials and Applications for Large Area Electronics: Solution-Based Approaches," *Chemical Reviews* **2010**, 110, 1, 3-24.

[4] A. Verma, D. Martineau, S. Abdolhosseinzadeh, J. Heier and F. Nuesch, "Inkjet printed mesoscopic perovskite solar cells with custom design capability," *Mater. Adv.* **2020**, 1, 153-160.

[5] S.-Y. Kim, K. Kim, Y. H. Hwang, J. Park, J. Jang, Y. Nam, Y. Kang, M. Kim, H. Park, Z. Lee, J. Choi, Y. Kim, S. Jeong, B.-S. Bae and J.-U. Park, "High-resolution electrohydrodynamic inkjet printing of stretchable metal oxide semiconductor transistors with high performance," *Nanoscale* **2016**, 8, 17113-17121.

[6] Z. Yin, Y. Huang, N. Bu, X. Wang and Y. Xiong, "Inkjet printing for flexible electronics: Materials, processes and equipments," *Chinese Sci. Bull.* **2010**, 55, 30, 3383-3407.

[7] M. Mao, J. He, X. Li, B. Zhang, Q. Lei, Y. Liu and D. Li, "The Emerging Frontiers and Applications of High-Resolution 3D Printing," *Micromachines* **2017***,* 8, 113, 1-20.

[8] C. Peroz, V. Chauveau, E. Barthel and E. Sondergard, "Silica Sol-gel NanoImprint Resist: a simple route to sequential patterning," *Advanced Materials* **2009***,* 21, 5, 555-558.

[9] M. Yu, K. H. Ahn and S. J. Lee, "Design optimization of ink in electrohydrodynamic jet printing: Effect of viscoelasticity on the formation of Taylor cone jet," *Materials & Design* **2016***,* 89, 109-115.

[10] J. Kim, R. Kumar, A. J. Bandodkar and J. Wang, "Advanced Materials for Printed Wearable Electrochemical Devices: A Review," *Adv. Electron. Mater.* **2017***,* 3, 1, 1600260.

[11] Y. Han, C. Wei and J. Dong, "Super-resolution electrohydrodynamic (EHD) 3D printing of micro-structures using phase-change inks," *Manufacturing Letters* **2014***,* 2, 4, 96-99.

[12] M. S. Onses, E. Sutanto, P. M. Ferreira, A. G. Alleyne and J. A. Rogers, "Mechanisms, Capabilities, and Applications of High-Resolution Electrohydrodynamic Jet Printing," *Small* **2015***,* 11, 34, 4237-4266.

[13] E. Sutanto and A. Alleyene, "A semi-continuous Roll-to-Roll (R2R) electrohydrodynamic jet printing system," *Mechatronics* **2015***,* 31, 243-254.

[14] K. Rahman, M. Mustafa, N. Muhammad and K. Choi, "Electrohydrodynamic printed TiO2 flexible memory device – fabrication and characterisation," *Electronics Letters **2012**,* 48, 20, 1261-1263.

[15] Y. Liang, J. Yong, Y. Yu, A. Nirmalathas, K. Ganesan, R. Evans, B. Nasr and E. Skafidas, "Direct Electrohydrodynamic Patterning of High-Performance All Metal Oxide Thin-Film Electronics," *ACS Nano* **2019***,* 13, 12, 13957-13964.

[16] A. Khan, K. Rahman, M.-T. Hyun, D.-S. Kim and K.-H. Choi, "Multi-nozzle electrohydrodynamic inkjet printing of silver colloidal solution for the fabrication of electrically functional microstructures," *Applied Physics A* **2011***,* 1113-1120.

[17] E. Sutanto and A. Alleyne, "A semi-continuous Roll-to-Roll (R2R) electrohydrodynamic jet printing system," *Mechatronics,* vol. 31, pp. 243-254, 2015.

[18] B. W. An, K. Kim, H. Lee, S. Kim, Y. Shim, D. Lee, J. Y. Song and J. Park, *Adv. Mater.* **2015***,* 27, 4322-4328.

[19] B. Y. Ahn, E. B. Duoss, M. J. Motala, X. Guo, S. Park, Y. Xiong, J. Yoon, R. G. Nuzzo, J. A. Rogers and J. A. Lewis, *Science* **2009***,* 323, 5921, 1590-1593.

[20] J. Park, M. Hardy, S. J. Kang, K. Barton, K. Adair, D. K. Mukhopadhyay, C. Y. Lee, M. S. Strano, A. G. Alleyne, J. G. Georgiadis, P. M. Ferreira and J. A. Rogers, *Nature Materials* **2007***,* 6, 782-789.

[21] B. Zhang, J. He, X. Li, F. Xu and D. Li, "Micro/nanoscale electrohydrodynamic printing: from 2D to 3D," *Nanoscale* **2016***,* 8, 15376–15388.

[22] S.-H. Lee, X. H. Nguyen, Y. Gim and H. S. Ko, "Study on electrohydrodynamic jetting performance of organic solvents," *Journal of Mechanical Science and Technology* **2015***,* 29, 11, 4767-4774.

[23] A. Lee, H. Jin, H.-W. Dang, K.-H. Choi and K. H. Ahn, "Optimization of Experimental Parameters To Determine the Jetting Regimes in Electrohydrodynamic Printing," *Langmuir* **2013***,* 29, 13630-13639.

[24] P. Zhou, H. Yu, W. Zou, Y. Zhong, X. Wang, Z. Wang and L. Liu, "Cross-scale additive direct-writing fabrication of micro/nano lens arrays by electrohydrodynamic jet printing," *Optics Express* **2020***,* 28, 5, 6336-6349.

[25] R. T. Collins, M. T. Harris and O. A. Basaran, "Breakup of electrified jets," *J. Fluid Mech.* **2007***,* 588, 75-129.

[26] H. Brunner and J. MacKenzie, "Inorganic-organic hybrid inks for attoliter scale electrohydrodynamic inkjet printing with applications in meta-optics and printed photonics," *ACS Appl. Mater. Interfaces,* **2022**.

[27] Q. Nie, Q. Ma, W. Yang, X. Pan, Z. Liu, H. Fang and Z. Yin, "Designing working diagrams for electrohydrodynamic printing," *Chemical Engineering Science* **2021***,* 240, 116661.

[28] M. Lee, D. Kang, N. Kim, S. James and S. Yoon, "A study of ejection modes for pulsed-DC electrohydrodynamic inkjet printing," *Journal of Aerosol Science* **2012***,* 46, 1-6.

[29] H. Yudistira, V. Nguyen, P. Dutta and D. Byun, "Flight behavior of charged drops in electrohydrodynamic inkjet printing," *Appl. Phys. Lett.* **2010***,* 96, 023503.

[30] S. Tran, D. Byun, V. Nguyen and T. Kang, "Liquid meniscus oscillation and drop ejection by ac voltage, pulsed dc voltage, and superimposing dc to ac voltages," *Phys. Rev. E.* **2009***,* 80, 026318.

[31] J. Schneider, P. Rohner, P. Galliker, S. N. Raja, Y. Pan, M. K. Tiwari and D. Poulikakos, "Site-specific deposition of single gold nanoparticles by individual growth in electrohydrodynamically-printed attoliter droplet reactors," *Nanoscale* **2015***,* 7, 9510-9519.

[32] H.-j. Kwon, J. Hong, S. Y. Nam, H. H. Choi, X. Li, Y. J. Jeong and S. H. Kim, "Overview of recent progress in electrohydrodynamic jet printing in practical printed electronics: focus

on the variety of printable materials for each component," *Materials Advances* **2021**, 2, 5593-5615.

[33] T. Cohen, D. Sharp, K. Kluherz, Y. Chen, C. Munley, R. Anderson, C. Swanson, J. De Yoreo, C. Luscombe, A. Majumdar, D. Gamelin and J. MacKenzie, "Direct Patterning of Perovskite Nanocrystals on Nanophotonic Cavities with Electrohydrodynamic Inkjet Printing," *Nano Lett.* **2022**, 22, 14, 5681–5688.

[34] H. T. Yudistira, A. P. Tenggara, S. S. Oh, V. Nguyen, M. Choi, C.-g. Choi and D. Byun, "High-resolution electrohydrodynamic jet printing for the direct fabrication of 3D multilayer terahertz metamaterial of high refractive index," *J. Micromech. Microeng.* **2015**, 25, 045006.

[35] T. T. T. Can, T. C. Nguyen and W.-S. Choi, "High-Viscosity Copper Paste Patterning and Application to Thin-Film Transistors Using Electrohydrodynamic Jet Printing," *Advanced Engineering Materials* **2020**, 22, 3, 1901384.

[36] S. M. Kamali, E. Arbabi, A. Arbabi and A. Faraon, "A review of dielectric optical metasurfaces for wavefront control," *Nanophotonics* **2018**, 7, 6, 1041-1068.

[37] Y. Kivshar, "All-dielectric meta-optics and non-linear photonics", *Nat. Sci. Rev.* **2018**, 5, 2, 144-158.

[38] E. Bayati, A. Zhan, S. Colburn, M. V. Zhelyeznyakov and A. Majumdar, "Role of refractive index in metalens performance," *Applied Optics* **2019**, 58, 6, 1460-1466.

[39] D. Wen, F. Yue, W. Liu, S. Chen and X. Chen, "Geometric Metasurfaces for Ultrathin Optical Devices," *Advanced Optical Materials* **2018**, 6, 7, 1800348.

[40] J. Muller, "MEMS on silicon for integrated optic metrology and communication systems," *Microsystems Technologies* **2003**, 9, 5, 308-315.

[41] E. B. Duoss, M. Twardowski and J. A. Lewis, "Sol-Gel Inks for Direct-Write Assembly of Functional Oxides," *Advanced Materials* **2007***,* 19, 3485-3489.

[42] A. Zhan, S. Colburn, R. Trivedi, T. K. Fryett, C. M. Dodson and A. Majumdar, "Low Contrast Dielectric Metasurface Optics," *ACS Photonics* **2016***,* 3, 2, 209-214.

[43] N. Mkhize and H. Bhaskaran, "Electrohydrodynamic Jet Printing: Introductory Concepts and Considerations," *Small Science* **2021***,* 2, 2, 2100073.

[44] N. Duraisamy, N. M. Muhammad, H.-C. Kim, J.-D. Jo and K.-H. Choi, "Fabrication of TiO2 thin film memristor device using electrohydrodynamic inkjet printing," *Thin Solid Films* **2012***,* 520, 15, 5070-5074.

[45] H. Choi, H. Jung, D.-K. Choi and C.-Y. Kim, "Alignment of One-Dimensional Sn02 Lines by Eiectrohydrodynamic Jet Printing," *Journal of Nanoscience and Nanotechnology* **2016***,* 16, 1818-1821.

[46] U. Schubert, "Chemical modification of titanium alkoxides for sol-gel processing," *Journal of Materials Chemistry* **2005***,* 15, 3701-3715.

[47] B. Peng, G. Jungmann, D. Haarer, H.-W. Schmidt and M. Thelakkat, " Systematic investigation of the role of compact TiO2 layer in solid state dye-sensitized TiO2 solar cells," *Coordination Chemistry Reviews* **2004***,* 248, 1479-1489.

[48] C. Jiang, W. L. Koh, M. Leung, W. Hong, Y. Li and J. Zhang, "Influences of alcoholic solvents on spray pyrolysis deposition of TiO2 blocking layer films for solid-state dye-sensitized solar cells," *Journal of Solid State Chemistry* **2013***,* 198, 197-202.

[49] D. Janssen, R. De Palma, S. Verlaak, P. Heremans and W. Dehaen, "Static solvent contact angle measurements, surface free energy and wettability determination of various self-assembled monolayers on silicon dioxide," *Thin Film Solids* **2006***,* 515, 1433-1438.

[50] M. Psarski, G. Celichowski, E. Bystrzycka, D. Pawlak, J. Grobelny and M. Cichomski, "Vapor phase deposition of fluoroalkyl trichlorosilanes on silicon and glass: Influence of deposition conditions and chain length on wettability and adhesion forces," *Materials Chemistry and Physics* **2018***,* 204, 305-314.

[51] M. Valiskó and D. Boda, "Relative Permittivity of Polar Liquids. Comparison of Theory, Experiment, and Simulation," *J. Phys. Chem. B* **2005***,* 109, 13, 6355-6365.

[52] A. Khalife, U. Pathak and R. Richert, "Heating liquid dielectrics by time dependent fields," *The European Physical Journal B* **2011***,* 83, 429-435.

[53] R. Collins, K. Sambath, M. Harris and O. Basaran, "Universal scaling laws for the disintegration ofelectrified drops," *PNAS* **2013***,* 110, 13, 4905-4910.

[54] J. Park, S. Lee, S. Unarunotai, Y. Sun, S. Dunham, T. Song, P. Ferreira, A. G. Alleyene, U. Paik and J. Rogers, "Nanoscale, Electrified Liquid Jets for High-Resolution Printing of Charge," *Nano Letters* **2010***,* 10, 584-591.

[55] H. Brunner, J. Whitehead, R. Gibson, Hendrickson, J.R., A. Majumdar and J. MacKenzie, "Fully Additive Electrohydrodynamic Inkjet Printed TiO2 Mid-Infrared Meta-Optics," *Advanced Materials Interfaces,* **2022**, 2200149.

[56] G. Zhang and M. Liu, "Preparation of nanostructured tin oxide using a sol-gel process based on tin tetrachloride and ethylene glycol," *Journal of Materials Science* **1999***,* 34, 3213-3219.

[57] P. Blainey and P. Reid, "FTIR studies of intermolecular hydrogen bonding in halogenated ethanols," *Spectrochimica Acta Part A* **2001***,* 57, 2763-2774.

[58] L. Huang, S. Colburn, A. Zhan and A. Majumdar, "Full color metaoptical imaging in visible light", *Adv. Photonics Res.* **2022***,* p. 2100265.

[59] J. Engelberg and U. Levy, "The advantages of metalenses over diffractive lenses", *Nature Communications* **2020***,* 11, 1991.

[60] R. Paniagua-Dominguez, Y. F. Yu, E. Khaidarov, S. Choi, V. Leong, R. M. Bakker, X. Liang, Y. H. Fu, V. Valuckas, L. A. Krivitsky and A. I. Kuzentsov, "A metalense with a near unity numerical aperture", *Nano Lett.* **2018***,* 18, 3, 2124-2132.

[61] P. Zhou, H. Yu, Y. Zhong, W. Zou, Z. Wang and L. Liu, "Fabrication of waterproof artificial compound eyes with variable field of view based on the bioinspiration from natural hierarchical micro-nanostructures", *Nano-Micro Lett.* **2020***,* 12, 166.

[62] C.-H. Liu, J. Zheng, S. Colburn, T. K. Fryett, Y. Chen, X. Xu and A. Majumdar, "Ultrathin van der Waals Metalenses," *Nano Letters* **2018***,* 18, 11, 6961-6966.

[63] R. Grober, R. Schoelkopf and D. Prober, "Optical antenna: Towards a unity efficiency near-field optical probe," *Appl. Phys. Lett.* **1997***,* 70, 10, 1354-1356 .

[64] P. Bharadwaj, B. Deutsch and L. Novotny, "Optical Antennas," *Advances in Optics and Photonics* **2009***,* 1, 438-483.

[65] G. Andrade, Q. Min, R. Gordon and A. Brolo, "Surface-Enhanced Resonance Raman Scattering on Gold Concentric Rings: Polarization Dependence and Intensity Fluctuations," *The Journal of Physical Chemistry C* **2012***,* 116, 2672-2676.

[66] Q. Yan, D. Debu, P. Ghosh, J. Herzog, M. Ware and M. Benamara, "Plasmonic emission of hybrid Au/Ag bullseye nanostructures," *Materials Letters* **2019***,* 247, 131-134.

[67] G. Naik, J. Kim and A. Boltasseva, "Oxides and nitrides as alternative plasmonic materials in the optical range," *Optical Materials Express* **2011***,* 1, 6, 1091.

[68] N. Livneh, M. Harats, S. Yochelis, Y. Paltiel and R. Rapaport, "Efficient Collection of Light from Colloidal Quantum Dots with a Hybrid Metal−Dielectric Nanoantenna," *ACS Photonics* **2015***,* 2, 1669-1674.

[69] S. Anderson, S. Bogdanov, O. Makarova, Y. Xuan, M. Shalaginov, A. Boltasseva, S. Bozhevolnyi and M. Shalaev, "Hybrid Plasmonic Bullseye Antennas for Efficient Photon Collection," *ACS Photonics* **2018***,* 5, 692-698.

[70] J. Boyer, L. Cuccia and J. Capobianco, "Synthesis of Colloidal Upconverting NaYF4: Er3+/Yb3+ and Tm3+/Yb3+ Monodisperse Nanocrystals," *Nano Letters* **2007***,* 7, 3, 847-852.

[71] G. Yi, H. Lu, S. Zhao, Y. Ge, W. Yang, D. Chen and L. Guo, "Synthesis, Characterization, and Biological Application of Size-Controlled Nanocrystalline NaYF4:Yb,Er Infrared-to-Visible Up-Conversion Phosphors," *Nano Lett.* **2004***,* 4, 11, 2191-2196.

[72] S. Xu, W. Xu, B. Dong, X. Bai and H. Song, "Downconversion from visible to near infrared through multi-wavelength excitation in Er3+/ Yb3+ co-doped NaYF4 nanocrystals," *Journal of Applied Physics* **2011***,* 110, 113113.

[73] F. Wang, Y. Han, C. Lim, Y. Lu, J. Wang, J. Xu, H. Chen, C. Zhang, M. Hong and X. Liu, "Simultaneous phase and size control of upconversion nanocrystals through lanthanide doping," *Nature* **2010***,* 463, 1061-1065.

[74] A. Bard, X. Zhou, X. Xia, G. Zhu, M. Lim, S. Kim, M. Johnson, J. Kollman, M. Marcus, S. Spurgeon, D. Perea, A. Devaraj, J. Chun, J. De Yoreo and P. Pauzauskie, "A Mechanistic Understanding of Nonclassical Crystal Growth in Hydrothermally Synthesized Sodium Yttrium Fluoride Nanowires," *Chem. Meter.* **2020***,* 32, 7, 2753-2763.

[75] D. Tu, Y. Liu, H. Zhu, R. Li, L. Liu and X. Chen, "Breakdown of Crystallographic Site Symmetry in Lanthanide-DopedNaYF4Crystals," *Angewandte Chemie* **2013***,* 125, 4, 1091-1371.

[76] H. Mai, Y. Zhang, R. Si, Z. Yan, L. Sun, L. You and C. Yan, "High-Quality Sodium Rare-Earth Fluoride Nanocrystals: Controlled Synthesis and Optical Properties," *J. Am. Chem. Soc.* **2006***,* 128, 19, 6426-6436.

[77] S. Hao, L. Sun, G. Chen, H. Qiu, C. Xu, T. Soitah, Y. Sun and C. Yang, "Synthesis of monoclinic Na3ScF6:1mol% Er3+/2mol% Yb3+ microcrystals by a facile hydrothermal approach," *Journal of Alloys and Compounds* **2012***,* 522, 74-77.

[78] J. Holsa, T. Laihinen, T. Laamanen, M. Lastusaari, L. Pihlgren, L. Rodrigues and T. Soukka, "Enhancement of the up-conversion luminescence from NaYF4:Yb3+,Tb3+," *Physica B: Condensed Matter* **2014***,* 439, 20-23.

[79] C. Lee, H. Park, W. Kim and S. Park, "Origin of strong red emission in Er3+-based upconversion materials: role of intermediate states and cross relaxation," *Phys. Chem. Chem. Phys.* **2019***,* 21, 24026-24033.

[80] H. Liu, J. Han, C. McBean, C. Lewis, P. Routh, M. Cotlet and S. Wong, "Synthesis-driven, structure-dependent optical behavior in phase-tunable NaYF4:Yb,Er-based motifs and associated heterostructures," *Phys. Chem. Chem. Phys.* **2017***,* 19, 2153-2167.

[81] D. Kim, "Recent Developments in Lanthanide-Doped Alkaline Earth Aluminate Phosphors with Enhanced and Long-Persistent Luminescence," *Nanomaterials* **2021***,* 11, 3, 723.

[82] Y. Huang, F. Fang, F. Chen, X. Cui, J. Sun, D. Zhuang and J. Wei, "Accurate generation of attolitre droplets for directly printing gold nanoparticles from solution through confined reaction," *Nano Ex.* **2020***,* 1, 3, 0008.

[83] E. Dobretsova, A. Pant, X. Xia, R. Gariepy and P. Pauzauskie, "Safe and Scalable Polyethylene Glycol-Assisted Hydrothermal Synthesis and Laser Cooling of 10%Yb3+:LiLuF4 Crystals," *Appl. Sci.* **2022***,* 12, 774.

[84] N. Venkataraman, J. Pei, C. Cremmel, A. Rossi and N. Spencer, "Template-Stripped, Ultraflat Gold Surfaces with Coplanar, Embedded Titanium Micropatterns," *Langmuir* **2013***,* 29, 9935-9943.

VITA

Holly J.C. Brunner was born in San Francisco, California and lived there with her family until she left The Golden State to attend college. She went to Bryn Mawr College for her undergraduate education and graduated in 2012 with a B.A in physics and a minor in geology. She began her graduate education at the University of Washington in the Materials Science and Engineering department. She quickly developed a passion for the discipline of materials science and her area of research. Holly intends to graduate with a Doctor of Philosophy in December 2022.